UNIVERSIDADE FEDERAL DE UBERLÂNDIA
PROGRAMA DE PÓS-GRADUAÇÃO EM ENGENHARIA QUÍMICA

CASSIANO CUNHA OLIVEIRA

HYDROGEN PRODUCTION FROM SORPTION ENHANCED STEAM REFORMING OF ETHANOL USING BIFUNCTIONAL NICKEL AND CALCIUM-BASED CATALYSTS DOPED WITH MAGNESIUM AND ALUMINUM

PRODUÇÃO DE HIDROGÊNIO ATRAVÉS DA REFORMA A VAPOR DE ETANOL COM CAPTURA DE DIÓXIDO DE CARBONO USANDO CATALISADORES BIFUNCIONAIS À BASE DE NÍQUEL E ÓXIDO DE CÁLCIO DOPADOS COM MAGNÉSIO E ALUMÍNIO

UBERLÂNDIA
2021

CASSIANO CUNHA OLIVEIRA

HYDROGEN PRODUCTION FROM SORPTION ENHANCED STEAM REFORMING OF ETHANOL USING BIFUNCTIONAL NICKEL AND CALCIUM-BASED CATALYSTS DOPED WITH MAGNESIUM AND ALUMINUM

PRODUÇÃO DE HIDROGÊNIO ATRAVÉS DA REFORMA A VAPOR DE ETANOL COM CAPTURA DE DIÓXIDO DE CARBONO USANDO CATALISADORES BIFUNCIONAIS À BASE DE NÍQUEL E ÓXIDO DE CÁLCIO DOPADOS COM MAGNÉSIO E ALUMÍNIO

Dissertação de mestrado apresentada ao Programa de Pós-Graduação em Engenharia Química da Universidade Federal de Uberlândia como parte dos requisitos necessários à obtenção do título de Mestre em Engenharia Química.

Orientadora: Profª Drª Carla Eponina Hori.

UBERLÂNDIA
2021

Ficha Catalográfica Online do Sistema de Bibliotecas da UFU
com dados informados pelo(a) próprio(a) autor(a).

O48
2021

Oliveira, Cassiano Cunha, 1997-
Hydrogen production from sorption enhanced steam reforming of ethanol using bifunctional nickel and calcium-based catalysts doped with magnesium and aluminum [recurso eletrônico] / Cassiano Cunha Oliveira. - 2021.

Orientadora: Carla Eponina Hori.
Dissertação (Mestrado) - Universidade Federal de Uberlândia, Pós-graduação em Engenharia Química.
Modo de acesso: Internet.
Disponível em: http://doi.org/10.14393/ufu.di.2021.340
Inclui bibliografia.

1. Engenharia química. I. Hori, Carla Eponina,1965-, (Orient.). II. Universidade Federal de Uberlândia. Pós-graduação em Engenharia Química. III. Título.

CDU: 66.0

Bibliotecários responsáveis pela estrutura de acordo com o AACR2:

Gizele Cristine Nunes do Couto - CRB6/2091

UNIVERSIDADE FEDERAL DE UBERLÂNDIA
Coordenação do Programa de Pós-Graduação em Engenharia Química
Av. João Naves de Ávila, 2121, Bloco 1K, Sala 206 - Bairro Santa Mônica, Uberlândia-MG, CEP 38400-902
Telefone: (34)3239-4249 - www.ppgeq.feq.ufu.br - secppgeq@feq.ufu.br

ATA DE DEFESA - PÓS-GRADUAÇÃO

Programa de Pós-Graduação em:	Engenharia Química				
Defesa de:	Dissertação de Mestrado, 11/2021, PPGEQ				
Data:	12 de julho de 2021	Hora de início:	07:30	Hora de encerramento:	09:05
Matrícula do Discente:	11922EQU004				
Nome do Discente:	Cassiano Cunha Oliveira				
Título do Trabalho:	Produção de hidrogênio através da reforma a vapor de etanol com captura de dióxido de carbono usando catalisadores bifuncionais à base de níquel e óxido de cácio dopados com magnésio e alumínio.				
Área de concentração:	Desenvolvimento de Processos Químicos				
Linha de pesquisa:	Termodinâmica, Cinética Química e Reatores				
Projeto de Pesquisa de vinculação:	Produção de hidrogênio por reações de reforma de hidrocarbonetos				

Reuniu-se por meio de webconferência, a Banca Examinadora, designada pelo Colegiado do Programa de Pós-graduação em Engenharia Química, assim composta: Professores Doutores: Sandra Cristina Dantas - ICTE/UFTM; Christian Gonçalves Alonso - IQ/UFG e Carla Eponina Hori - PPGEQ/UFU, orientadora do candidato.

Iniciando os trabalhos a presidente da mesa, Profa. Dra. Carla Eponina Hori apresentou a Comissão Examinadora e o candidato, agradeceu a presença do público e concedeu ao Discente a palavra para a exposição do seu trabalho. A duração da apresentação do Discente e o tempo de arguição e resposta foram conforme as normas do Programa.

A seguir, a senhora presidente concedeu a palavra, pela ordem sucessivamente, aos examinadores, que passaram a arguir o candidato. Ultimada a arguição, que se desenvolveu dentro dos termos regimentais, a Banca, em sessão secreta, atribuiu o resultado final, considerando o candidato:

aprovado.

Esta defesa faz parte dos requisitos necessários à obtenção do título de Mestre.

O competente diploma será expedido após cumprimento dos demais requisitos, conforme as normas do Programa, a legislação pertinente e a regulamentação interna da UFU.

Nada mais havendo a tratar foram encerrados os trabalhos. Foi lavrada a presente ata que após lida e achada conforme foi assinada pela Banca Examinadora.

Documento assinado eletronicamente por **Carla Eponina Hori**, **Professor(a) do Magistério Superior**, em 12/07/2021, às 09:05, conforme horário oficial de Brasília, com fundamento no art. 6º, § 1º, do Decreto nº 8.539, de 8 de outubro de 2015.

Documento assinado eletronicamente por **Christian Gonçalves Alonso**, **Usuário Externo**, em 12/07/2021, às 09:05, conforme horário oficial de Brasília, com fundamento no art. 6º, § 1º, do Decreto nº 8.539, de 8 de outubro de 2015.

Documento assinado eletronicamente por **Sandra Cristina Dantas**, **Usuário Externo**, em 12/07/2021, às 09:06, conforme horário oficial de Brasília, com fundamento no art. 6º, § 1º, do Decreto nº 8.539, de 8 de outubro de 2015.

A autenticidade deste documento pode ser conferida no site https://www.sei.ufu.br/sei/controlador_externo.php?acao=documento_conferir&id_orgao_acesso_externo=0, informando o código verificador **2896939** e o código CRC **4A300F4A**.

AGRADECIMENTOS

A Deus pela dádiva da vida e pelas forças para chegar aonde estou hoje.

Aos meus pais e irmãos por terem sempre acreditado em mim e me motivarem a continuar no caminho da pesquisa.

À professora e orientadora Carla, por toda a disponibilidade, conversas, conselhos e boa vontade de me auxiliar em todas as etapas desse trabalho sem medir esforços.

Aos colegas de laboratório, em especial ao Dyovani e Lucas Gomes pelos ensinamentos e auxílio no tratamento de dados e na execução dos procedimentos experimentais.

Aos técnicos da Faculdade de Engenharia Química que ajudaram no desenvolvimento deste projeto.

A todos os professores que repassaram seus conhecimentos ao longo da vida acadêmica, sendo os pilares da minha formação.

Ao Grupo de Materiais Inorgânicos do Triângulo (GMIT), que conta com o amparo da FAPEMIG (APQ-00330-14) pelas análises texturais desse trabalho.

À Universidade Federal de Uberlândia, ao Programa de Pós-Graduação em Engenharia Química e aos órgãos de fomento CAPES, FAPEMIG e CNPq.

Por fim, agradeço a todos, que de certa forma contribuíram para a conclusão de mais um ciclo.

RESUMO

Este trabalho avaliou o desempenho de catalisadores à base de níquel suportados em CaO e CaO-MgO-Al_2O_3 na reforma a vapor de etanol melhorada (RVEM) visando a produção de H_2 de alta pureza. Os catalisadores foram preparados pelo método sol-gel e caracterizados por diferentes métodos: Redução a temperatura programada (RTP), difração de raios X (DRX), microscopia eletrônica de varredura (MEV) com mapeamento de elementos químicos, fisissorção de N_2 e análise termogravimétrica (ATG). As análises de DRX mostraram que as fases predominantes foram CaO, MgO, $CaCO_3$, $Ca(OH)_2$ e NiO nas amostras calcinadas e de Ni^0 nas amostras reduzidas e passivadas. Os perfis de RTP indicaram que todos os catalisadores tiveram um alto grau de redução (Ni/CaMgAl-68 > Ni/CaMgAl-79 > Ni/Ca), embora as amostras de Ni/CaMgAl-X apresentem altas temperaturas de redução indicando a formação de $NiAl_2O_4$. A RTP realizada nas condições de temperatura da ativação do catalisador obteve um grau de redução do NiO superior a 90% devido ao contato das amostras em uma atmosfera redutora por um tempo maior do que o usado durante a análise de RTP. A ATG mostrou que o catalisador Ni/CaMgAl-68 foi o mais estável durante os 20 ciclos de carbonatação e regeneração porque teve a menor perda de capacidade de captura de CO_2. No entanto, o catalisador Ni/CaMgAl-79 apresentou a maior capacidade de captura após 20 ciclos tanto em relação a massa de catalisador quanto por massa de CaO. Os testes catalíticos na RVEM mostraram que o catalisador Ni/CaMgAl-79 teve o melhor desempenho, uma vez que foi o que teve maior tempo de produção de hidrogênio de alta pureza. No período de *pre-breakthrough*, as frações molares de H_2 ficaram próximas de 90% para todas as amostras durante todos os ciclos reacionais. Além disso, a captura de CO_2 promovida pelo sorvente permitiu que esses valores de concentração fossem superiores às da reforma a vapor de etanol convencional, devido ao deslocamento do equilíbrio que favorece a produção de H_2. A ATG realizada após os ciclos reacionais também mostraram que provavelmente a presença dos óxidos metálicos MgO e Al_2O_3 nos catalisadores minimizou a formação de coque na superfície dos catalisadores, obtendo taxas médias de deposição de 11,5, 7,4 e 6,2 $mgC/g_{cat}/h$, para os catalisadores de Ni/Ca, Ni/CaMgAl-79 e Ni/CaMgAl-68, respectivamente.

Palavras-chave: catalisadores à base de níquel, reforma a vapor de etanol melhorada (RVEM), óxido de cálcio, óxido de magnésio, óxido de alumínio, hidrogênio de alta pureza.

ABSTRACT

This work evaluated the performance of nickel-based catalysts supported on CaO and CaO-MgO-Al_2O_3 in the sorption enhanced steam reforming of ethanol (SESRE) aiming the production of high purity H_2. The catalysts were prepared by sol-gel method and characterized by different methods: Temperature programmed reduction (TPR), X-ray diffraction (XRD), scanning electronic microscopy (SEM) with chemical element mapping, N_2 physisorption and thermogravimetric analysis (TGA). XRD analyses showed that the predominant phases were CaO, MgO, $CaCO_3$, $Ca(OH)_2$ and NiO in the calcined samples and Ni^0 in the reduced and passivated samples. TPR profiles indicated that all catalysts presented a high degree of reduction (Ni/CaMgAl-68 > Ni/CaMgAl-79 > Ni/Ca), although the Ni/CaMgAl-X samples presented high reduction temperatures indicating the formation of $NiAl_2O_4$. TPR performed under temperature conditions of catalyst activation obtained a degree of reduction of NiO over 90% due to the contact of the samples in a reducing atmosphere for a longer time than that used during TPR analysis. TGA showed that the catalyst Ni/CaMgAl-68 was the most stable during the 20 cycles of carbonation and decarbonation because it had the lowest loss of CO_2 uptake capacity. However, Ni/CaMgAl-79 catalyst showed the highest capture capacity after 20 cycles in relation both to mass of catalyst and by mass of CaO. The catalytic tests in the SESRE showed that Ni/CaMgAl-79 catalyst had the best performance since it had the longest high purity hydrogen production time. In the pre-breakthrough period, the H_2 mole fractions were close to 90% for all samples during all reaction cycles. Furthermore, the CO_2 capture promoted by the sorbent allowed these concentration values to be higher than conventional steam reforming of ethanol, due to the equilibrium shift that favors H_2 production. The TGA performed after the reaction cycles also showed that probably the presence of the metal oxides (MgO and Al_2O_3) in the catalysts minimized the formation of coke on the surface of the catalysts, obtaining average deposition rates of 11.5, 7.4 and 6.2 $mgC/g_{cat}/h$, for the Ni/Ca, Ni/CaMgAl-79 and Ni/CaMgAl-68 catalysts, respectively.

Keywords: nickel-based catalysts, sorption enhanced steam reforming of ethanol (SESRE), calcium oxide, magnesium oxide, aluminum oxide, high purity hydrogen.

LIST OF FIGURES

TABLE LIST

SUMMARY

CHAPTER 1. INTRODUCTION

Due to global population growth, urbanization and industrial development, energy demand continues to increase. Nowadays, energy supply is heavily dependent on fossil fuels, which are non-renewable. This type of energy is gradually depleted and has been causing serious environmental problems, especially global warming effects. Renewable energy, which presents a low environmental impact, is an alternative way to face the increasing energy demands of the 21st century (Chen et al., 2020).

Among the more sustainable forms of energy, hydrogen has been considered to be one of the most promising future energy sources due to its clean combustion, abundance in our planet, and high energy content (120.7 kJ/g). Hydrogen has great potential to be used in transportation, fuel cells and power stations. It is also used as an important reactant in chemical industries, which is implemented in some processes such as ammonia synthesis, Fischer–Tropsch synthesis, and oil refining processes (Chen et al., 2020; Chen; Pei; Gong, 2019).

Catalytic reforming is an effective and classic method to produce hydrogen, which has been used for several years in commercial chemical production and fuel upgrading. In recent years, a lot of work has been devoted to the reforming of renewable resources, such as biomass and biomass-derived liquid fuels, which are becoming an important research field. Using biomass as a renewable resource is very advantageous because it is highly available in many forms and it has a low dependence on location and climate. The expansion of feedstock usage from hydrocarbons (CH_4) to oxygenated compounds (CH_3OH, C_2H_5OH) has brought new challenges and opportunities for the catalytic reforming process. Steam reforming of ethanol (SRE) is a sustainable option because ethanol can be produced from renewable biomass during fermentation process. It is a promising hydrogen storage chemical for large-scale transportation since the global annual output of ethanol exceeds 900 million tons (Ashok et al., 2020; Chen et al., 2020; Chen; Pei; Gong, 2019).

Although it is a suitable alternative, SRE process produces carbon dioxide as a byproduct, which is a main concern due to environmental problems linked to global warming. To solve this, a promising technology to produce hydrogen can be used, also

known as Sorption Enhanced Steam Reforming of Ethanol (SESRE). This process associates the conventional steam reforming to CO_2 capture using a sorbent in the catalyst, favoring H_2 production according to Le Chatelier's Principle. These catalysts are known as bifunctional since they have both catalytic activity and sorbent characteristics. Nickel has been used as the active phase and calcium oxide as the CO_2 sorbent of the catalyst during sorption enhanced steam reforming process. This partial reforming of ethanol reaction provides high yield to hydrogen (4 mol of H_2 per mol of ethanol fed) as shown in Equation 1.1. The water-gas shift reaction also occurs in the reactional system and can be represented by Equation 1.2. Equation 1.3 represents the capture reaction performed by the sorbent (Gunduz; Dogu, 2012; Nimmas et al., 2019).

$$C_2H_5OH + H_2O \rightleftarrows 2CO + 4H_2 \qquad \Delta H^0_{298\,K} = 255.9\ kJ/mol \qquad \text{Equation 1.1}$$

$$CO + H_2O \rightleftarrows H_2 + CO_2 \qquad \Delta H^0_{298\,K} = -41.2\ kJ/mol \qquad \text{Equation 1.2}$$

$$CO_{2(g)} + CaO_{(s)} \rightleftarrows CaCO_{3(s)} \qquad \Delta H^0_{298\,K} = -178.2\ kJ/mol \qquad \text{Equation 1.3}$$

Many studies have shown that CaO-based materials are used as solid sorbents for CO_2 capture due to their good thermodynamic and chemical properties. The strong decrease in sorption capacity after multiple carbonation/decarbonation cycles is the main problem of CaO and sintering process is believed to be the cause of the decay. Another reason may be related to the formation of a non-porous calcium carbonate layer on the surface of the CaO particles, limiting the CO_2 diffusion to the bulk of the grain (Cesário et al., 2015). In order to overcome this problem, researchers have been using a spacer strategy to improve CaO properties, where the sintering process is avoided by using a refractory phase to separate the sorbent particles (Dang et al., 2016). Several studies have shown that this refractory phase can be metal oxides (MgO, Al_2O_3, ZrO_2, TiO_2, Y_2O_3, etc.) or mixture oxides ($Ca_{12}Al_{14}O_{33}$, Ca_2SiO_4, etc.) during sorption enhanced steam reforming (Dang et al., 2020; Sang et al., 2019; Wang et al., 2020; Zhao et al., 2014).

The addition of a refractory phase to CaO may enhance the sorbent anti-sintering properties. In the literature, there are few studies that evaluate the stability over the cyclic reaction/regeneration process for ethanol reforming since it is more common to find in the literature sorption enhanced steam reforming of methane. Thus, the general objective of this work is to study nickel-based catalysts supported on CaO and CaO-MgO-Al_2O_3 for the sorption enhanced steam reforming of ethanol (SESRE) aiming H_2 production with high purity. The specific objectives include to prepare and characterize the catalysts; to evaluate the CO_2 sorption capacity over 20 carbonation and decarbonation cycles; to quantify the products during catalytic tests over 10 cycles and to study the influence of adding metal oxides into CaO in the cyclic stability of the bifunctional catalysts.

CHAPTER 2. LITERATURE REVIEW

2.1. Hydrogen

Nowadays society has been facing a very important environmental challenge: climate change caused by global warming. However, industry is still highly dependent on traditional fossil fuels (such as natural gas, petroleum and coal) as energy sources. Fossil fuels can cause high greenhouse gas (GHG) emissions during the combustion process. In addition, since energy consumption is closely related to industrialization and rapid population growth, it is expected that energy consumption will continue to increase in the future. Therefore, there is an urgent need to use renewable energy sources to reduce greenhouse gas emissions to the atmosphere (Capa et al., 2020).

Studies have been developed in order to use hydrogen as a future energy vector for transportation, fuel cells and power plants due to its waste-free combustion, high energy mass density, and a variety of raw materials that can be used for its production. The renewable production of this fuel can be conducted through different methods, such as photolysis, thermolysis and electrolysis of water, biological reactions, gasification and pyrolysis of biomass, partial oxidation and steam reforming of fossil and renewable biomass. Hydrogen production from photocatalytic process has been making progress, but the excessive demand for electricity makes the electrochemical process expensive. The photolysis of water is very expensive because of the requirement of high-cost electrodes. It is also possible to find biological methods in the literature, but they present a low rate of hydrogen generation. These inconveniences make thermochemical method a viable way to produce hydrogen sustainably (Sharma et al., 2017).

Although there are several technologies to produce hydrogen from sustainable and renewable energy resources (such as solar, wind and geothermal energy to hydrogen), hydrogen production from biomass has presented a favorable condition in terms of economic and environmental issues. The availability and low prices of biomass feedstock represent the main economic advantages (Hosseini et al., 2015). Some of the hydrogen production pathways are illustrated in Figure 2.1.

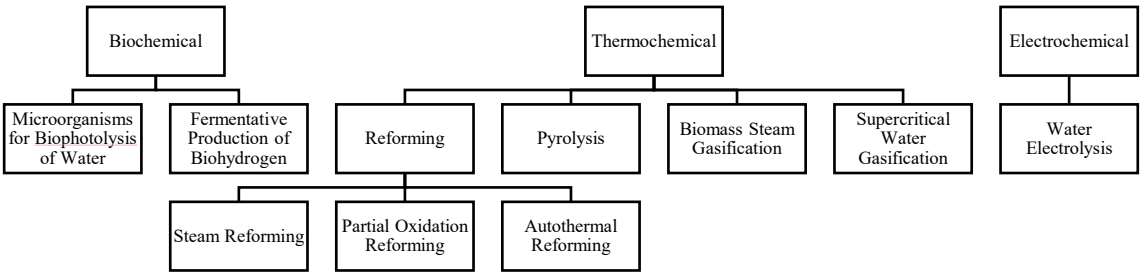

Figure 2.1. Traditional routes for hydrogen production, adapted from Lamb et al., (2020).

In contrast to other methods that require chemical or electrochemical counterparts, microorganisms catalyze the biochemical routes of H_2 production (Lamb et al., 2020). There are some methods to produce hydrogen and each group uses an appropriate type of microorganism. The biochemical production of hydrogen processes can be classified as direct biophotolysis (microalgae), indirect biophotolysis (cyanobacteria), photo fermentation (purple bacteria) and dark fermentation (closteridum) (Bolatkhan et al., 2019).

The thermochemical process involves thermally assisted chemical reactions to release gases with high purity hydrogen. Some sources, such as biomass, nuclear and fossil fuels, can be used by this rout. The traditional thermochemical processes commonly used for H_2 production include reforming, pyrolysis, gasification, water splitting and supercritical water extraction.

Reforming refers to the use of various technologies to convert carbon-containing fuels. When hydrocarbon fuels react with steam or O_2 (or a combination of the two) at high temperatures, H_2 is produced. These reactions are known as reforming reactions. When only steam is used, the reaction is endothermic, this process is steam reforming. The partial oxidation reaction uses O_2 for fuel conversion, which is called an exothermic reforming reaction. The combination of steam reforming and partial oxidation is called an autothermal reforming reaction (Lamb et al., 2020).

Pyrolysis consists on heating and degasifying raw organic materials at a temperature of 500-900 °C and pressure of 0.1-0.5 MP. It occurs in the absence of oxygen and dioxin formation, therefore, can be almost negligible. CO and CO_2 are the minority products, which excludes the need of using secondary reactors (Bičáková; Straka, 2012). This process has pure carbon as by-product and the reaction can be usually described as Equation 2.1.

$$Organic\ material + heat \rightarrow H_2 + CO + CH_4 + other\ products \qquad \text{Equation 2.1}$$

Pyrolysis process is divided into different categories according to the temperature range: low (below 500 °C), medium (500-800 °C) and high (above 800 °C). Rapid pyrolysis is one of the latest processes to convert organic materials into products with higher energy content. The products of rapid pyrolysis appear in all phases: solid, liquid and gaseous (Bičáková; Straka, 2012).

Gasification of biomass is carried out in the presence of a gasification agent, which interacts with solid char and heavier hydrocarbons in order to convert them into CO and H_2. The gasification media can be steam, oxygen, air, carbon dioxide, or a combination of them. Gasification of biomass reduces the carbon to hydrogen mass ratio. Therefore, the H_2 fraction increases, which in turn raises the heating value of the output gaseous product (Sikarwar; Zhao, 2017).

Compared with thermochemical gasification, which consumes a lot of energy for biomass conversion, supercritical water (or hydrothermal) gasification is relatively energy-saving and does not require additional biomass drying. Lignocellulosic biomass components can be broken down into simple molecules in the supercritical water gasification (SCWG) process to produce syngas. Syngas (H_2 + CO) is the main product of biomass SCWG, which can be used as a clean fuel or to produce diesel fuel through gas-to-liquid (GTL) technology such as Fischer-Tropsch catalysis or syngas fermentation (Reddy et al., 2014).

Hydrogen production by water electrolysis has the advantages of no pollution, simple process, high purity, and wide sources. For one hundred years the industrial water electrolysis cells have been established. Nevertheless, water electrolysis is only used in

special situations that require high-purity hydrogen. In the past few decades, this technology has been regarded as a supplement to hydrocarbon sources rather than a replacement. However, fossil fuels, such as coal, petroleum or natural gas are not reliable due to severe environmental pollution and reduced reserves. Renewable primary energy sources such as wind, solar and ocean energy have received more and more attention. This could be an energy revolution that will change an era. The problems or disadvantages of renewable primary energy are intermittence, regionalism and non-storable, which can lead to instability of the power supply. Hydrogen production by electrolysis is considered to be the best energy carrier to adjust the balance between renewable primary energy power generation and energy demand for end-use. It provides an inspiring opportunity for the development of water electrolysis technology (Wang et al., 2014).

In the future, a roadmap with broad prospects for sustainable energy development is shown in Figure 2.2. Most renewable energy sources provide power for the end-use, and the excess electricity is used to electrolyze water to produce storable hydrogen and oxygen. Then, the hydrogen is delivered to areas lacking renewable energy to serve industry, traffic, electric stations, and households. The sustainable energy route is feasible and convenient. Then, pure hydrogen is produced by water electrolysis. Intermittent wind power is converted into stored hydrogen, which is used to power homes and cars through fuel cells (Wang et al., 2014).

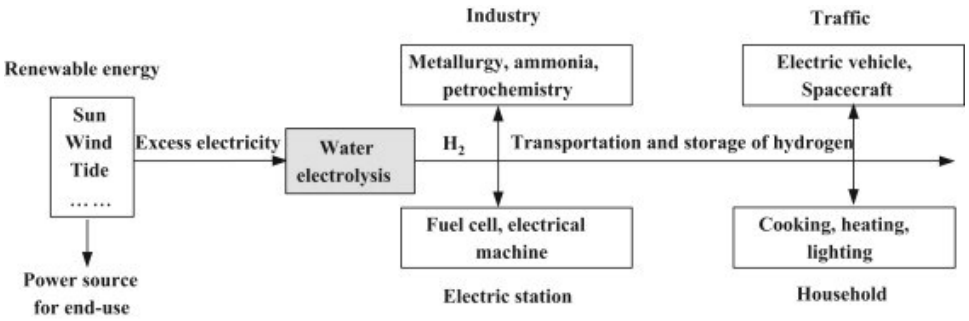

Figure 2.2. Sustainable production and energy application (Wang et al., 2014).

2.2. Steam reforming for hydrogen production

Steam reforming (SR) is carried out at high temperatures, with catalysts that convert hydrocarbons and steam into H_2 and other gases. Steam reforming must be

performed at high temperatures, high steam to carbon ratio and low pressure in order to maximize hydrogen yield because the reaction is reversible and strongly endothermic (according to Le Chatelier's principle). Some of the important steps of SR include the generation of synthesis gas, water-gas shift reaction (WGS) and gas purification. The catalyst used for reforming varies greatly depending on the type of feedstock. For instance, nickel-based catalysts are the most commonly used for steam reforming of methane. When choosing a catalyst, performance and cost are obviously the most critical considerations. It can be a combination with a variety of noble metals (such as Rh, Ru, Pt, Pd and Ir), transition metals (such as Ni, Co, Cu and Fe) and oxide support metals (such as Ni/MgO, Ru/Mg(Al)O and Ni/Al_2O_3) suitable for catalyst compositions. Studies have proved that catalysts composed of noble metals have high activity and stability for steam reforming reactions, but their high cost has led researchers to switch to low-cost materials (such as nickel-based catalysts), which have similar activity to the former. Besides metal catalysts, non-metal catalysts have also been studied but commercial success has not been achieved yet due to their small activity (Lamb et al., 2020). Table **2.1** compares the difference between noble and non-noble metals prices commonly used as active phase in steam reforming.

Table 2.1. Price of some noble and non-noble metals used in SR (Phung et al., 2020).

Metal	Price [(a)]
Ru	249.00 USD ozt^{-1}
Rh	3530.00 USD ozt^{-1}
Pt	843.50 USD ozt^{-1}
Pd	1505.50 USD ozt^{-1}
Ni	6.66 USD lb^{-1}
Co	12.93 USD lb^{-1}
Cu	2.70 USD lb^{-1}

[(a)] 1 pound (lb) = 14.58 troy ounces (ozt).

2.2.1. Steam reforming of ethanol (SRE)

Steam reforming of ethanol offers a promising solution for future hydrogen production. The advantage of using ethanol in hydrogen production is due to its renewable nature, relatively high hydrogen content, transport safety and low toxicity (Chen et al., 2020). It is common for steam reforming of ethanol to be performed at temperatures of 300 °C or more, usually from 450 to 600 °C. Thermodynamics shows that Gibbs free energy variation becomes a negative value above 205 °C. However, it is difficult to achieve high ethanol conversion and low coke formation at such low temperatures (Ogo; Sekine, 2020).

Steam reforming of ethanol reactions is complex and can occur by several pathways. Stoichiometrically, the overall reaction is represented as follows:

$$C_2H_5OH(g) + 3H_2O(g) \rightarrow 6H_2(g) + 2CO_2(g) \quad \Delta H^0_{r\,298K} = 174\ kJ\ mol^{-1} \qquad \text{Equation 2.2}$$

The series of reaction pathways that can occur in the ethanol reform is shown below (Bepari et al., 2017; Han et al., 2017; Ogo; Sekine, 2020):

1) Dehydration of ethanol to form ethylene (C_2H_4) and water followed by the formation of coke:

$$C_2H_5OH(g) \rightarrow C_2H_4(g) + H_2O(g) \quad \Delta H^0_{r\,298K} = 45.5\ kJ\ mol^{-1} \qquad \text{Equation 2.3}$$

$$C_2H_4(g) \rightarrow 2C(s) + 2H_2(g) \quad \Delta H^0_{r\,298K} = -52.3\ kJ\ mol^{-1} \qquad \text{Equation 2.4}$$

2) Decomposition of ethanol to form methane (CH_4), followed by steam reforming of methane:

$$C_2H_5OH(g) \rightarrow CH_4(g) + CO(g) + H_2(g) \quad \Delta H^0_{r\,298K} = 49.0\ kJ\ mol^{-1} \qquad \text{Equation 2.5}$$

$$CH_4(g) + 2H_2O(g) \rightarrow 4H_2(g) + CO_2(g) \quad \Delta H^0_{r\,298K} = 165.0\ kJ\ mol^{-1} \qquad \text{Equation 2.6}$$

3) Dehydrogenation of ethanol to form acetaldehyde (C_2H_4O), followed by decarboxylation or steam reforming:

$$C_2H_5OH(g) \rightarrow C_2H_4O(g) + H_2(g) \quad \Delta H^0_{r\,298K} = 68.9\ kJ\ mol^{-1}$$ Equation 2.7

$$C_2H_4O(g) \rightarrow CH_4(g) + CO(g) \quad \Delta H^0_{r\,298K} = -19.3\ kJ\ mol^{-1}$$ Equation 2.8

$$C_2H_4O(g) + H_2O(g) \rightarrow 3H_2(g) + 2CO(g) \quad \Delta H^0_{r\,298K} = 186.8\ kJ\ mol^{-1}$$ Equation 2.9

4) Decomposition of ethanol to form acetone (C_3H_6O), followed by steam reforming of acetone:

$$2C_2H_5OH(g) \rightarrow C_3H_6(g) + CO(g) + 3H_2(g) \quad \Delta H^0_{r\,298K} = 142\ kJ\ mol^{-1}$$ Equation 2.10

$$C_3H_6O(g) + 2H_2O(g) \rightarrow 5H_2(g) + 3CO_2(g) \quad \Delta H^0_{r\,298K} = -481\ kJ\ mol^{-1}$$ Equation 2.11

5) Steam reforming of ethanol to produces synthesis gas ($CO + H_2$):

$$C_2H_5OH(g) + H_2O(g) \rightarrow 2CO(g) + 4H_2(g) \quad \Delta H^0_{r\,298K} = 256.0\ kJ\ mol^{-1}$$ Equation 2.12

6) Water gas shift reaction (WGS):

$$CO(g) + H_2O(g) \rightarrow CO_2(g) + H_2(g) \quad \Delta H^0_{r\,298K} = -41.4\ kJ\ mol^{-1}$$ Equation 2.13

7) Methanation:

$$CO(g) + 3H_2(g) \rightarrow CH_4(g) + H_2O(g) \quad \Delta H^0_{r\,298K} = -206.1\ kJ\ mol^{-1}$$ Equation 2.14

$$CO_2(g) + 4H_2(g) \rightarrow CH_4(g) + 2H_2O(g) \quad \Delta H^0_{r\,298K} = -164.8\ kJ\ mol^{-1}$$ Equation 2.15

8) Decomposition of methane generating coke:

$$CH_4(s) \rightarrow 2H_2(g) + C(s) \quad \Delta H^0_{r\,298K} = 74.9\ kJ\ mol^{-1}$$ Equation 2.16

Figure 2.3 shows some possible reaction pathways of steam reforming of ethanol over nickel surface based on experimental and theoretical results. The ethanol reaction proceeds by the scission of OH bond, followed by continuous dehydrogenation (steps 2-

5), forming a series of intermediates, such as acetaldehyde (CH_3CHO^*), acetyl (CH_3C^*O), ketene ($^*CH_2C^*O$), and ketenyl ($^*CHC^*O$). After C-C bond of the intermediates is cleaved, hydrogenation/dehydrogenation, water activation and oxidation of C* species reaction may also occur (Zanchet et al., 2015).

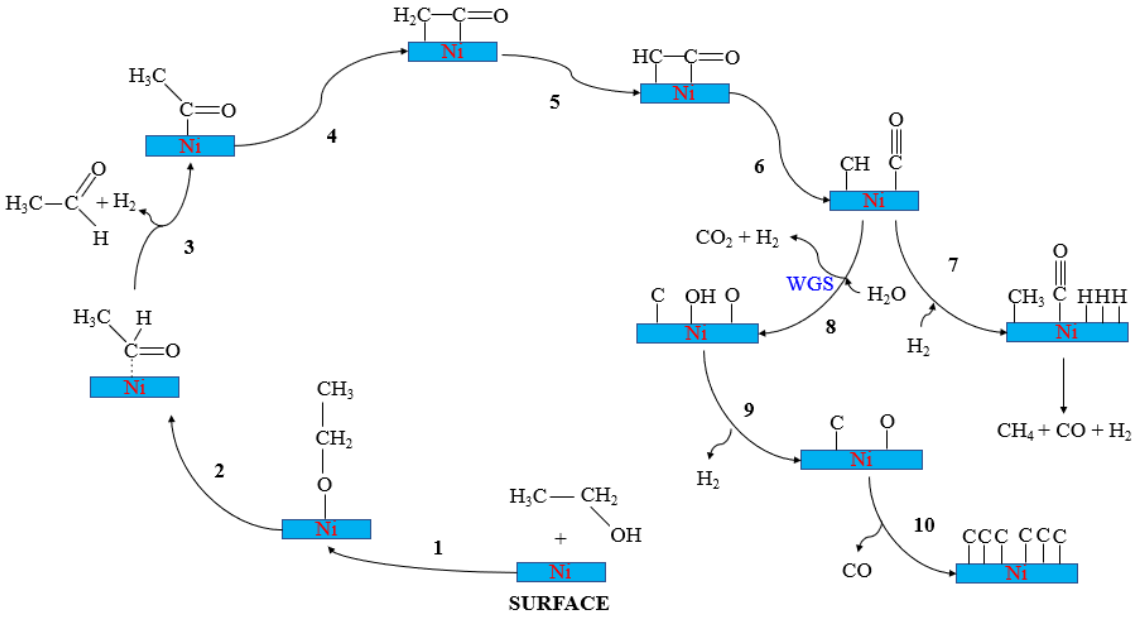

Figure 2.3. Schematic representation of the SRE reaction pathways for nickel catalysts, adapted from Zanchet et al. (2015).

There have been thousands of papers about catalysts tested for the steam reforming of ethanol and it is not the goal of this modest chapter to perform a wide literature review about this topic. Here are two examples of studies recently published about this topic: Di Michele et al. (2019) performed steam reforming of ethanol at 625 °C using $MgAl_2O_4$ as a stable support and varying nickel composition as an active phase (1.5, 5 and 10 wt%). For 1.5 wt% Ni, ethanol conversion was 86% and it was possible to observe ethylene as a byproduct due the catalyst low activity to reform this intermediate. This metal loading is insufficient for C–C bond cleavage, keeping unreacted ethanol and ethylene. This sample also had low stability due to the decrease of ethanol conversion after 450 minutes of reaction and the simultaneous increase of acetaldehyde selectivity, as can be seen in Figure 2.4. The other catalysts had 100% of ethanol conversion and

increasing the Ni content improved H_2 production because of the lower CO/CO_2 ratio promoted by the water-gas shift reaction and diminished CH_4 selectivity.

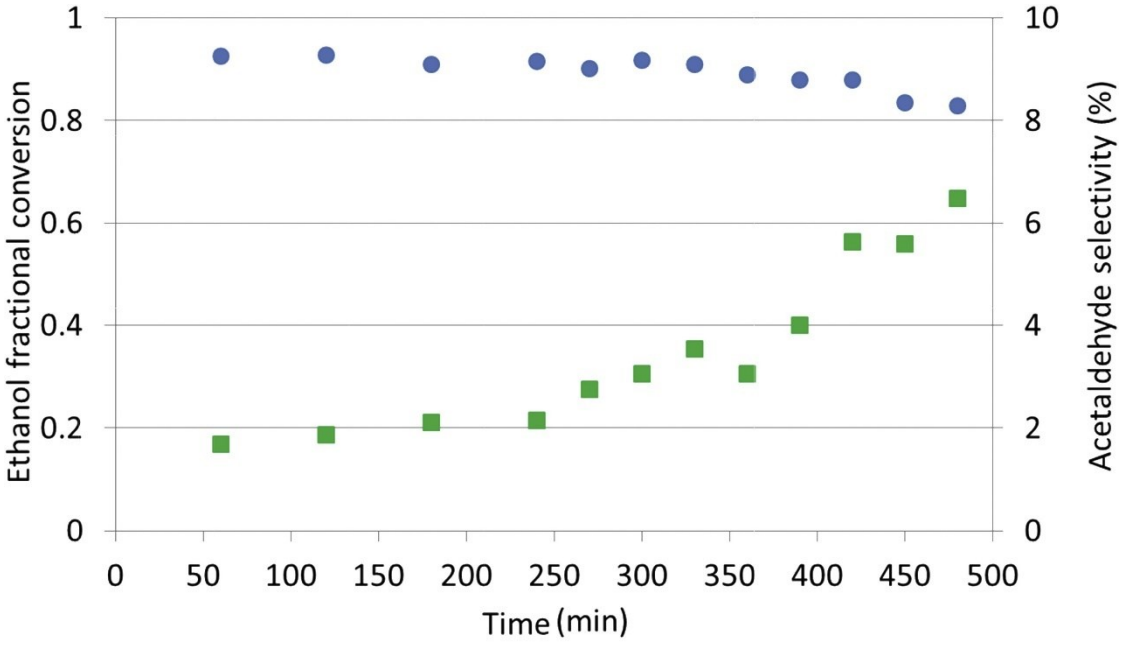

Figure 2.4. Steam reforming of ethanol using 1.5 wt% $Ni/MgAl_2O_4$ at 625 °C (Di Michele et al., 2019). Legend: ethanol conversion (●) and acetaldehyde selectivity (■)

Bepari et al. (2017) investigated a series of Ce-promoted Ni-Mg-Al hydrotalcite catalysts, prepared by co-precipitation followed by wet impregnation, during steam reforming of ethanol. The cerium content and reaction conditions were varied (temperature, steam/ethanol molar ratio and space-time) in order to observe the products distribution and catalytic activity. The catalyst with 10% Ce loading had a good stability and activity during a long time of reaction at atmospheric pressure. The best operational conditions were with a space-time of 22.04 kg_{cat} h $kmol^{-1}$ of ethanol fed and a steam/ethanol molar ratio of 9 at 540 °C. At these conditions, ethanol conversion was about 97% and hydrogen yield of 4.13 mol of hydrogen per mole of ethanol reacted.

2.3. Sorption enhanced steam reforming for hydrogen production

Sorption enhanced steam reforming (SESR) is an innovative technology that can produce H_2 on a large scale in a relatively low temperature range of 550-700 °C, achieving a high fuel conversion and high H_2 purities, when compared to the conventional

steam reforming processes. According to this concept, steam reforming, water-gas shift and CO_2 adsorption reactions can be carried out in a single reactor in the presence of a suitable catalyst composed of CO_2 sorbent. As CO_2 is removed from the gas phase by the sorbent in situ, the reaction shifts to the production of H_2, which increases the production of hydrogen, as predicted by Le Chatelier's principle (Capa et al., 2020; Vanga et al., 2019). In the environmental aspect, CO_2 capture and storage and the system to remove sulfur, make biomass-based hydrogen a best alternative comparing to fossil fuel-based hydrogen production (Hosseini et al., 2015). Figure 2.5 shows a schematic diagram that illustrates how this principle works.

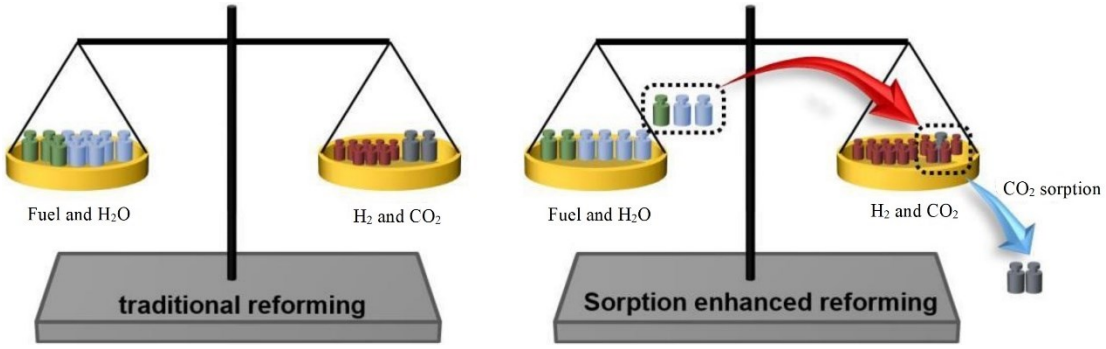

Figure 2.5. Schematic diagram of the SESR based on Le Chatelier's principle, adapted from Wang et al. (2021b).

In the SESR process, there are three important concepts that are worth to mention: pre-breakthrough, breakthrough and post-breakthrough period. In the pre-breakthrough period, the sorbent easily adsorbs the CO_2 formed during the SR and WGS reactions and favors the production of H_2 with high purity. The breakthrough period is characterized by the gradual reduction of the CO_2 sorption capacity of the sorbent due to the diffusion limitation, leading to the appearance of CO_2 at the reactor exit and lower H_2 molar fraction. When the sorption material is practically saturated, the H_2 and CO_2 molar fraction approach their equilibrium composition that would occur in the conventional steam reforming, this region is known as the post-breakthrough period (Ghungrud; Vaidya, 2020). When the SESR reaction reaches the breakthrough stage, it means that the regeneration process in the reactor should take place, also known as decarbonation process. The regeneration mode occurs at high temperatures, which is a favorable

condition to the reaction shown in Equation 2.17. Figure 2.6 describes the two processes that involve the SESR: sorption enhanced reaction and regeneration.

$$Carbonated\ sorbent(s) \leftrightarrow Sorbent(s) + CO_2(g)\ \Delta H_0 > 0 \qquad \text{Equation 2.17}$$

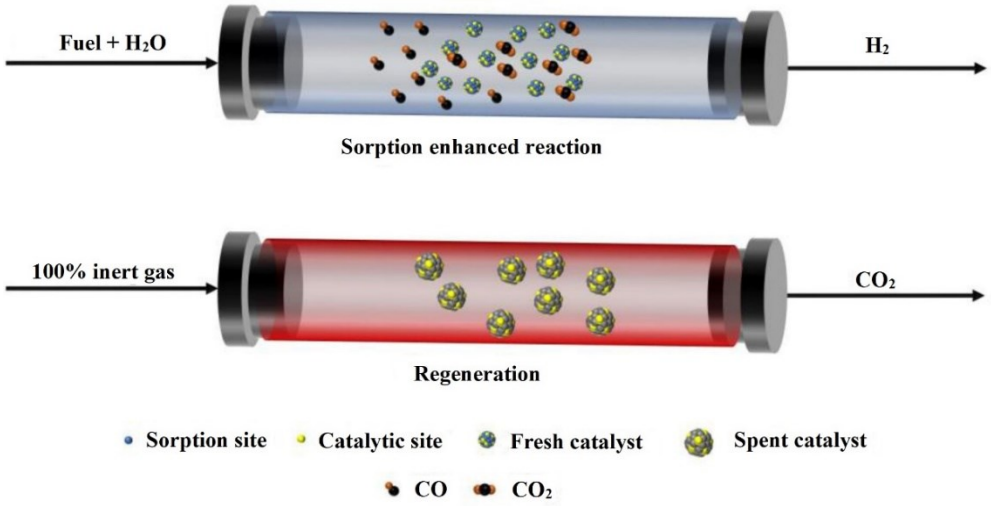

Figure 2.6. Representation of two processes in sorption enhanced steam reforming, adapted from Wang et al. (2021b).

Martavaltzi, Pefkos and Lemonidou (2011) performed SESR of methane using 1.5 g of nickel-based catalyst and 3–6 g of CaO-$Ca_{12}Al_{14}O_{33}$ sorbent. The steam to carbon molar ratio was 3.4 and the inlet flow of methane and helium was 36-144 cm³/min. The reaction was conducted at 500, 600 and 650 °C and decarbonation process was at 850 °C, in pure helium flow. Hydrogen concentration gradually decreases from 92-93% in the pre-breakthrough period to 77-78% in the post-breakthrough at 650 °C. Methane conversion achieved 95% in the reaction. They reported that the duration of the pre-breakthrough period is a function of sorbent properties (sorption kinetics and sorption capacity) and operating conditions (flow rate, sorbent mass, temperature, pressure). For a new batch of the same material, the duration of the pre-breakthrough period only increases due to different operating conditions. Therefore, the increase of sorbent mass from 3 to 6 g and other operating parameters were kept constant, the duration of the pre-breakthrough period was doubled (from 80 to 160 min).

Hu et al. (2017) studied SESR of acetic acid using 2 g of Ni-CaO-$Ce_xZr_{1-x}O_2$ catalyst with a Ca/(Zr+Ce) ratio of 2.5 and a Steam/Carbon ratio of 4 at 550 °C. Figure 2.7 shows the product distribution on dry basis for the first cycle and they found the three typical steps for this process: pre-breakthrough, breakthrough and post-breakthrough. The methanation reaction of CO was not considered by the authors in the first cycle of SESR of acetic acid because of its low concentration was maintained. The H_2 concentration in the pre-breakthrough period was 95.5% and in the post-breakthrough was 68.4%, which represents a strong evidence of the sorption enhanced effect. They also reported that this catalyst had a valuable performance due the addition of Zr to Ca, which enabled the $CaZrO_3$ formation, diminishing the sintering rate of CaO and increasing the efficiency of CaO utilization.

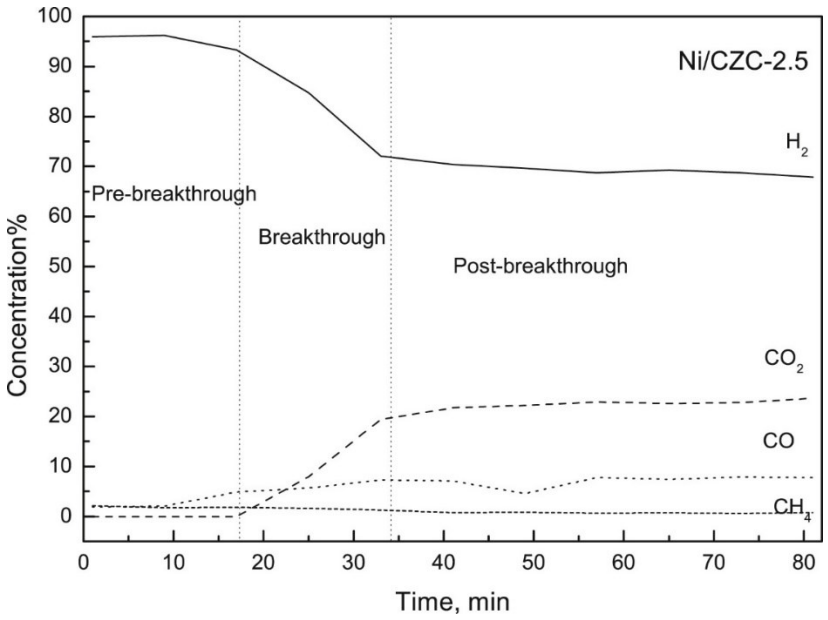

Figure 2.7. Products found on the first cycle of sorption enhanced steam reforming of acetic acid bounded by the three typical periods. Operational conditions: Steam/Carbon ratio = 4, $T_{reaction}$ = 550 °C, 1 atm, 2 g of catalyst, 0.016 mL/min (Hu et al., 2017).

Wu et al. (2012) investigated SESR of ethanol using Ni-CaO-Al_2O_3 catalyst derived from hydrotalcite-like compounds, varying the Ca/Al molar ratio (CA = 2, 2.5, 3 and 3.5). They used a mixture of 30 mg of catalyst and 0.1 mL of quartz sand. The reaction was performed at 500 °C and 1 atm with a steam to carbon molar ratio of 4 during 120

minutes. The catalytic test showed that CA2.5 and CA3.0 catalysts had higher H_2 concentration than the other two even in the post-breakthrough period. This may be attributed to highly dispersed nickel nanoparticles and the strong interaction between nickel and oxides. These two factors have been shown to contribute to high activity for hydrocarbon conversion and reforming reactions. Although CA3.0 catalyst had good performance in SESRE process, CA3.5 was the one that reached the maximum adsorption of CO_2 at 500 °C (24.8%).

2.3.1. Materials used in sorption enhanced steam reforming

Calcium oxide (CaO) is commonly used in the process of CO_2 capture due to its favorable characteristics, such as high availability of their precursors, low cost, high CO_2 capture capacity, fast CO_2 sorption-desorption kinetics and regeneration capacity (Dang et al., 2020a). CaO can be obtained by decomposing different calcium precursor compounds (such as calcium carbonate, calcium hydroxide, calcium acetate, calcium nitrate, etc). Among them, calcium carbonate ($CaCO_3$) is widely used as a precursor of CaO because it is easy to find in nature. However, the chemical and texture properties of natural $CaCO_3$ resources are diverse and difficult to control the requirements of industrial processes. Therefore, synthetic $CaCO_3$ has been developed to replace natural CaO in order to overcome their limitations and can be used in a variety of applications, such as CO_2 sorption, hydrogen production, renewable fuel production, etc (Nimmas et al., 2019).

The carbonation/decarbonation cyclic process occurs in CaO-based materials during SESR, which consists on converting CaO into $CaCO_3$ under CO_2 atmosphere. This process is divided into three distinct stages (Yoon; Mun; Lee, 2021):

(i) in the rapid chemical reaction-controlled carbonation stage, the surface of unreacted CaO undergoes rapid CO_2 chemisorption without any interruption, and a thin layer composed of $CaCO_3$ is formed around the CaO particles;

(ii) in the slow diffusion-controlled carbonation stage, the unreacted CaO is completely surrounded by the $CaCO_3$ layer and the CO_2 sorption kinetics suddenly decreases for the additional CO_2 sorption due the limitation of CO_2 diffusion through the carbonate layer;

(iii) in the calcination stage, also known as decarbonation or regeneration, the CO_2 feeding is stopped and only remains an inert stream in order to release the CO_2 present in the material that contains $CaCO_3$.

Figure 2.8a shows the typical profile of CO_2 capture capacity (C_t) as a function of time, obtained by a thermogravimetric analyzer, over multiple carbonation/decarbonation cycles. When zooming in the first cycle of CaO material (Figure 2.8b), it is possible to observe the three-stage mechanisms listed before. Figure 2.9 illustrates the first two CO_2 sorption mechanisms that occur on CaO-based materials.

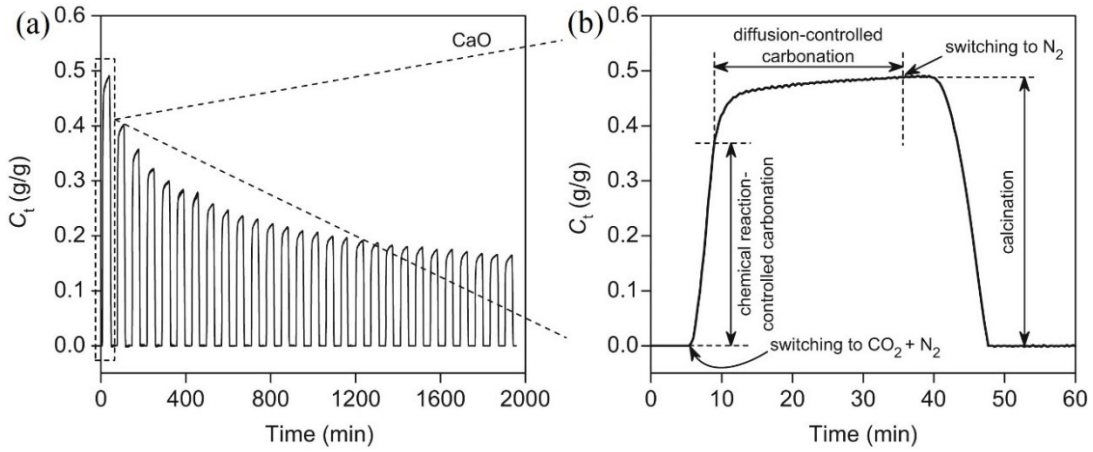

Figure 2.8. (a) Multiple carbonation/decarbonation cycles and (b) stages of the carbonation process (Zhou et al., 2012).

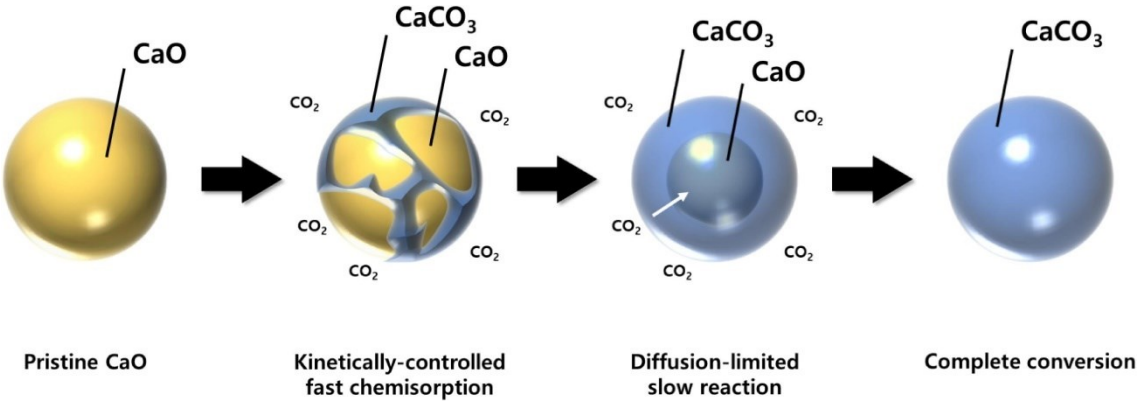

Figure 2.9. Representative scheme of two CO_2 sorption mechanisms that occur on CaO-based materials: the kinetically controlled stage and diffusion-limited stage (Yoon; Mun; Lee, 2021)

Although being considered a very attractive sorbent, after several adsorption/desorption cycles at high temperatures, the CO_2 sorption capacity of CaO declines. It is generally observed that in the first 10 cycles of pure CaO or limestone sorbents, the sorption capacity is reduced by 60% to 80% (Dang et al., 2020a). The rapid decrease in CO_2 sorption capacity is related to the increase of CaO crystal grain size and the formation of a $CaCO_3$ layer on the surface of the sorbent, which deteriorates the microstructure in the high-temperature adsorption/desorption cycles, reducing the CO_2 adsorption rate and inhibits the diffusion of CO_2 from the solid state. Therefore, in order to increase the stability of CaO, the effect of adding different metal ions to CaO has been studied, including Al^{3+}, Y^{3+}, Zr^{4+}, La^{3+}, Mg^{2+}, Ti^{4+} and Si^{4+}. These metal ions are selected according to their Tammann temperature, the minimum temperature at which ions, atoms or molecules in the solid acquire enough energy to undergo a solid-solid interaction and take part in sintering process. Figure 2.10 exhibits the Tammann temperature for some metal oxides. Tammann temperature is given by a fraction of the absolute melting temperature (approximately 0.5 for bulk diffusion and 0.3 for surface diffusion) (Phromprasit et al., 2017). The reaction temperature for SESR is usually higher than the Tammann temperature of $CaCO_3$ (533 °C), which causes a decrease in porosity and activity of the material. However, doping inert oxides stabilizes the CO_2 uptake activity of the CaO and improves the sintering resistance, key features for materials used in SESR reactions (Xu et al., 2016).

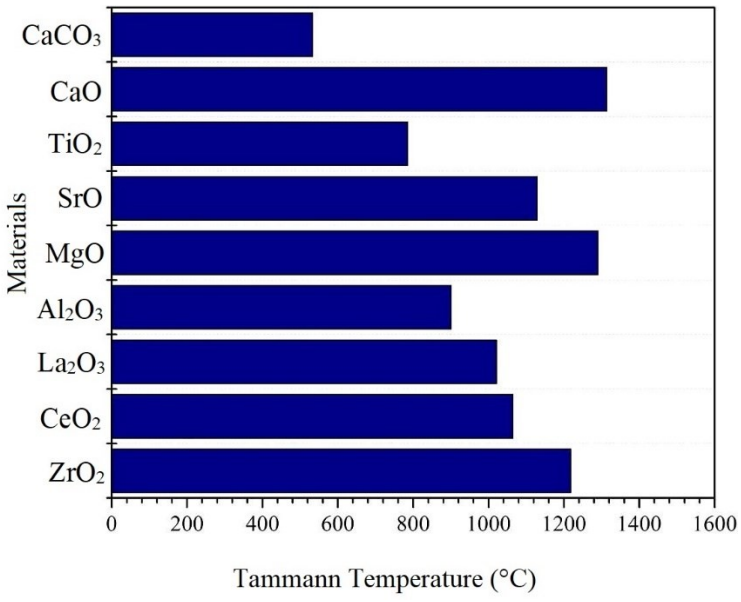

Figure 2.10. Representation for Tammann temperature of some materials (Phromprasit et al., 2017).

The catalysts used in SESR have a different characteristic when compared to those used in SR: the presence of both active phase for reforming and CO_2 sorbent, denominated bifunctional materials. This integration into one particle allows the improvement of mass and heat transfer characteristics between reforming (endothermic) and carbonation (exothermic) reactions, which have been reported by several theoretical studies (Broda et al., 2012; Xu et al., 2014). CaO is the most attractive sorbent to be used on bifunctional materials, however, its fast-sintering process needs a strategy development to stabilize it, as the incorporation of metal oxides previously described.

Zhao et al. (2017) investigated the use of Ni-CaO-La_2O_3 catalyst with 8, 16 and 20 wt% Ni for hydrogen production via SESR of acetic acid. The experiments were conducted using 2 g of catalyst at 650 °C, 1 atm and WHSV (Weight Hourly Space Velocity) of 0.6316 $g_{acetic\ acid}/g_{cat}\ h^{-1}$. The best performance was achieved by the 20 wt% Ni-CaO-La_2O_3 catalyst with hydrogen concentration and yield of 92.24 and 86.02%, respectively, in the pre-breakthrough period. This catalyst was stable during the catalytic tests, which had a good Ni dispersion and enough Ni^0 on the surface, but during the carbonation tests the CO_2 uptake capacity was slightly declined due to sintering process and blockage of pores within the first nine carbonation/decarbonation cycles.

Li et al., (2020) prepared a bifunctional catalyst, as shown in Figure 2.11, via sol-gel method. The feed was composed by 45 mL/min of N_2 and 0.01 mL/min of liquid flow rate with a steam to carbon molar ratio of 1.3. The reaction was carried out with 1 g of catalyst at 220 °C and 1 atm. The 8 wt% Cu-MgO/Al_2O_3 catalyst had the optimal performance for SESR of methanol. Metallic Cu had good results as active site on the catalyst surface for this reaction. They reported that the interaction between Cu ion and MgO promotes sorption capacity and by forming more bidentate carbonates, the desorption of carbon dioxide is facilitated. It was found that the inhibition of carbon monoxide production happened due to the induction of more formate species caused by MgO. They also concluded that there was an inhibition of Cu sintering when compared to materials that had a mechanical mixture of sorbents and catalysts.

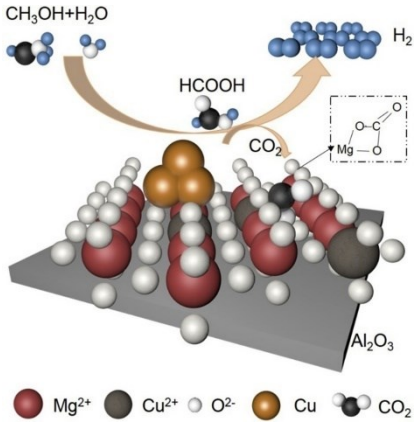

Figure 2.11. Representation of Cu-MgO/Al_2O_3 catalyst used in SESR of methanol, adapted from Li et al. (2020).

Dang et al. (2020a) performed SESR of glycerol, which is an abundant by-product from biodiesel manufacturing. They used Ni-CaO-MgO catalysts prepared by hydrothermal method that formed a porous material with small size of CaO particles. It was required only 8.1 wt% of MgO to stabilize it. The catalytic test was performed using 0.5 g of catalyst at 550 °C and 1 atm. A liquid mixture of 0.02 mL/min containing glycerol and water (S/C = 4) with 30 mL/min of N_2 as carried gas was fed into the reactor. After 10 carbonation/decarbonation cycles, the sorption capacity was 0.374 gCO_2/g_{cat}, higher value than some found on the literature (usually lower than 0.20 gCO_2/g_{cat}), and reached 98.66 and 0.31 vol% of H_2 and CO_2, respectively, in the pre-breakthrough region during the catalytic test.

Dang et al. (2020b) also prepared Ni-Ca-Al-O catalysts by coprecipitation method and performed SESR of phenol using 1 g of catalyst at 550 °C and 1 atm. The reactor was fed with a liquid mixture of phenol and water (0.0797 g/mL, S/C ratio of 11) at 0.02 mL/min with an Ar carrier gas flow of 25 mL/min. The best catalyst achieved 98.88% of purity of hydrogen and approximately 100% of conversion under the optimum conditions of reaction. After 50 reaction/decarbonation cycles (nearly 100 h), phenol conversion and hydrogen concentration were stabilized at 100 and 98%, respectively. They also reported that during the stability test coke was not present in the catalysts. Figure 2.12 represents the catalyst structure used in the SESR of phenol to produce hydrogen with high purity.

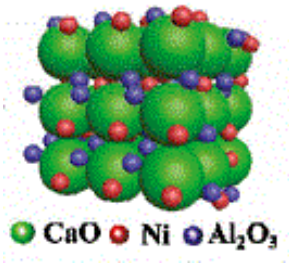

Figure 2.12. Structure representation of Ni-Ca-Al-O catalyst, adapted from Dang et al. (2020b).

Fermoso, He and Chen (2012) produced hydrogen from SESR of crude glycerol using a mixture of 12 g of sorbent (calcined dolomite) and catalyst (Ni-Co/hydrotalcite-like material). The tests were performed from 525 to 600 °C, at atmospheric pressure. The inlet of the reactor was composed by 75-150 mL/min of N_2 with 5-10 g/h of liquid reactant mixture in a way that N_2/C molar ratio remained constant. At 550-600 °C with a steam to carbon of 3, H_2 yield was up to 88% and its purity was approximately 99.7 vol%. CO concentration increases with the temperature rise from 525 to 600 °C whereas methane was lowest at 575 °C. They also reported that methane reforming and water-gas shift reactions exhibited higher reaction rates than steam reforming of crude glycerol.

Dewoolkar and Vaidya (2017) studied SESR of butanol using K-Ni-CaO/hydrotalcite (HTlc), Ni-CaO/HTlc and Ni-CaO/HTlc. The catalytic tests were performed from 773 to 923 K using a steam to butanol ratio of 3-9. The highest H_2 concentration (98.7 mol%) and sorption capacity (12.8 mol $CO_2/kg_{sorbent}$) was obtained by K-Ni-CaO/HTlc at 823 K with steam to butanol ratio of 5. This catalyst also had the best stability during 21 cycles. The improvement of hydrogen production, multiple cycles stability and resistance occurred due to the addition of K as a promoter.

2.3.2. Sorption enhanced steam reforming of ethanol (SESRE)

Wang et al. (2021a) studied sorption enhanced steam reforming of ethanol using lithium silicate-based sorbents in two parallel reactors. To prepare them, rice husk ash was used as silica precursor for the sorbent, which guarantees a sustainable characteristic by reusing residues. The material was modified by doping metallic elements (K, Ca, Al, Mg) in order to improve its chemical properties. The reaction was carried out with 2 g of

catalyst and 8 g of sorbent at 525 °C. A mixture containing steam to carbon ratio of 8 and LHSV (Liquid Hourly Space Velocity) of 0.8 mL/g h was fed in the reactor. The decarbonation was at 650 °C with a total flow rate of 30 mL/min (10 vol% H_2/N_2). The one which had the best CO_2 uptake properties was the K-doped Li_4SiO_4 and it was used in the catalytic test under the optimal conditions obtained by thermodynamics analysis. Figure 2.13 shows the product distribution over the 10 reaction/decarbonation cycles for K-doped sorbent with Ni as its active phase. It can be seen that CO and CO_2 achieved low concentrations in all cycles, indicating good stability without compromising the CO_2 capture capacity during the regeneration process. The catalytic activity was decreased due to coke formation causing a fluctuation of CH_4 concentration. However, H_2 remained higher than 93% during reaction.

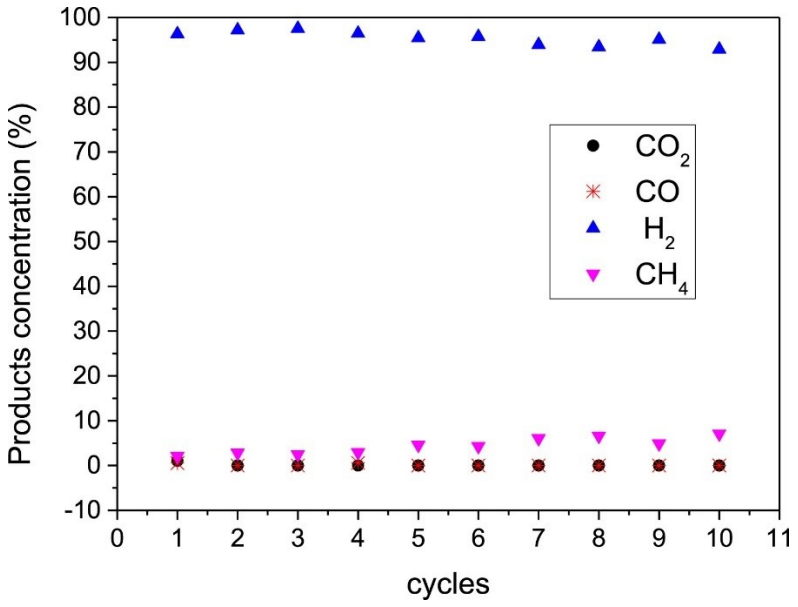

Figure 2.13. Products concentration obtained over 10 reaction/decarbonation cycles during SESRE process (Wang et al., 2021a).

A study comparing the performance of Ni/CaO and Ni/CaO-MgO catalysts was carried out by Sang et al. (2019). They prepared the materials by coprecipitation method and used them in sorption enhanced steam reforming of ethanol. SESRE tests were conducted using 0.5 g of catalyst at 600 °C, 1 atm, S/C = 4, liquid feed of 0.015 mL/min. The regeneration time was 120 minutes at 700 °C, 1 atm and 60 mL/min of N_2. For both catalysts 100% of ethanol conversion was reached over the 10 cycles. As the number of

cycles of Ni/CaO catalyst increased, the purity of hydrogen decreased significantly due to the decrease in catalytic activity of steam reforming of methane reaction and a direct evidence is the increase in CH_4 concentration shown in Figure 2.14a. As far as the Ni/CaO-MgO catalyst is concerned (Figure 2.14b), it can maintain high hydrogen purity in 10 cycles, varying from 97.2 to 96 vol% in the 1st and 10th cycles, respectively. It was observed that the pre-breakthrough duration of both catalysts was shortened, from 50 to 35 minutes in the first and tenth cycles, respectively, which can be attributed to the decrease in the CO_2 sorption capacity of the samples. This work confirmed that adding MgO as a dopant improved the catalyst cyclic stability, producing high-purity hydrogen and reduced the coke deposition. Figure 2.14 presents the products distribution over 10 cycles for SESRE reactions for Ni/CaO and Ni/CaO-MgO catalysts.

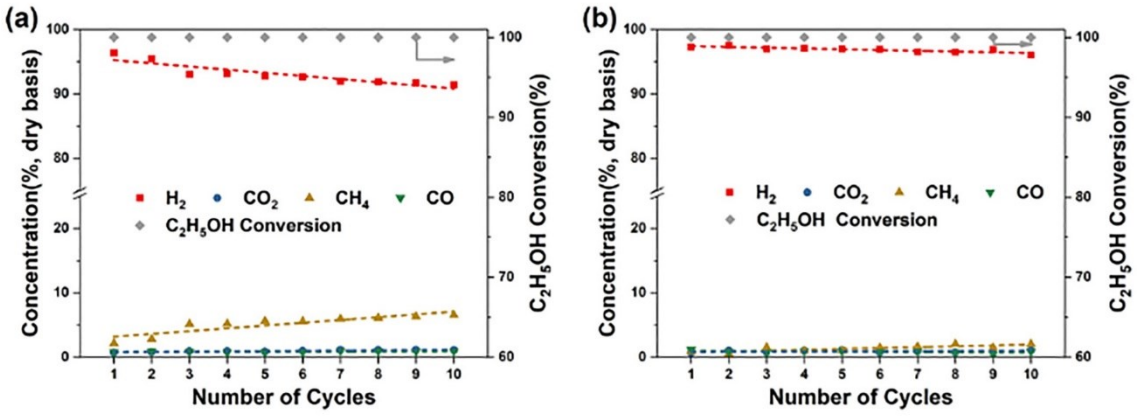

Figure 2.14. Concentrations obtained over 10 cycles during SESRE reaction for (a) Ni/CaO and (b) Ni/CaO-MgO (Sang et al., 2019).

Rahmanzadeh and Taghizadeh (2019) investigated SRE and SESRE reactions using Ce-Ni/NCM-41 and CaO as sorbent at 600 °C with molar ratio steam/ethanol of 6 and WHSV of 1.99 h^{-1}. The regeneration of the sorbent occurred at 850 °C under pure N_2 atmosphere. As can be seen in Figure 2.15a, analyzing the gas products for SRE the amount of H_2 and CO_2 produced is about 70 and 20%, respectively. The products distribution for SESRE reaction (Figure 2.15b) showed a significant increase in hydrogen production was found, which is due to the CO_2 capture by the sorbent present in the catalyst and following Le Chatelier's principle. In addition, because of this effect, the

values of CO and CO_2 are significantly reduced. In the beginning of SESRE reaction (pre-breakthrough period), H_2 concentration was 93%, being decreased to 70% after 210 minutes, which obviously corresponds to the saturated state of the CaO sorbent for a longer period of time, caused by the reaction with CO_2 and the formation of $CaCO_3$ on the surface of the sorbent (post-breakthrough period). Before 60 minutes of reaction, CO and CO_2 values were very low, indicating that the CaO-based sorbent has significant CO_2 absorption. After 60 minutes, the amount of CO enhanced as the content of CO_2 increased. In Figure 2.15 can be seen the distribution of gaseous products generated from SRE (just catalyst) and SESRE (catalyst and sorbent), indicating that the sorbent plays an important role in the H_2 purity.

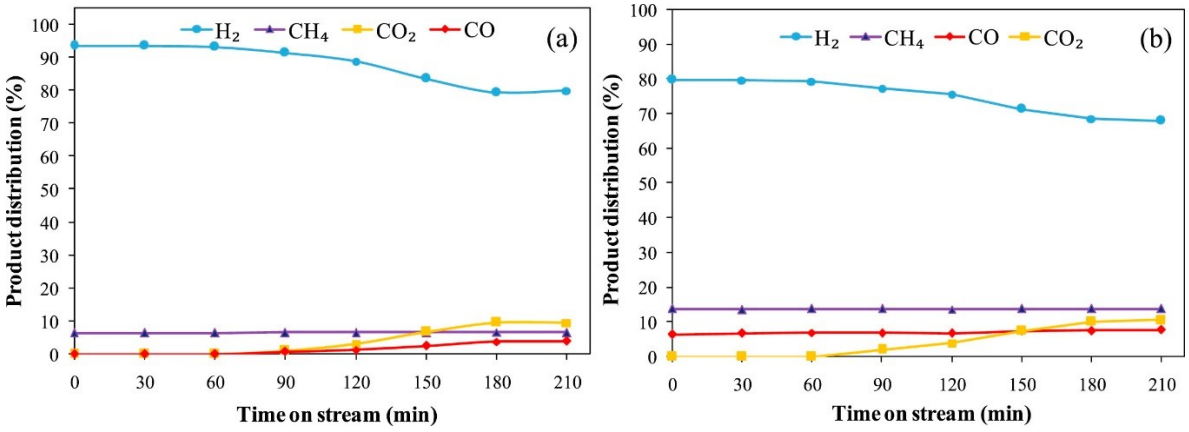

Figure 2.15. Catalytic tests for (a) SRE and (b) SESRE reactions over 210 minutes (Rahmanzadeh; Taghizadeh, 2019).

Combining the traditional Ni/Al_2O_3 catalyst with the new CaO-based porous spherical sorbent (prepared by a new molding method) has been studied by Xu et al. (2021) in the sorption-enhanced steam reforming of ethanol process (SESRE) to improve H_2 purity. They used 0.5 g of catalyst at 650 °C and 1 atm with a feed of 0.08 mL/min containing a steam to ethanol ratio of 4. The regeneration occurred at 900 °C for 15 minutes with 200 mL/min of pure N_2. In the pre-breakthrough stage, high-purity H_2 is produced, especially the process that is enhanced by a modeled sorbent (CaOS-C5 pellets) using cells as a template, showing a good perspective to use these pellets in the SESRE process. Using CaOS-C5, it was possible to reach continuously a H_2 concentration higher than 90% in the 10^{th} SESRE process for at least 15 minutes of reaction. The authors

reported that the spheric CaO-based sorbent greatly increases the concentration of H_2. The Ni/Al_2O_3 catalyst coupled with the modeled sorbent presented good stability in the long-term reaction in repeated cycles, which shows that these new spherical sorbents improve the catalytic activities for the SESRE process.

Based on the works presented in this literature review, it was verified that there are advantages to use nickel and calcium bifunctional catalysts doped with inert materials during the sorption enhanced steam reforming of ethanol rection. This process reaches higher purity of H_2 than the conventional steam reforming of ethanol, it is eco-friendly because it avoids emitting pollutants in the environment and reduces the operation costs in the industrial field by not requiring extra separation processes at the reactor outlet. Ethanol is used as a renewable source for H_2 production to avoid depletion of fossil fuel materials and nickel is used as active phase of SESRE because its low price and high catalytic activity. Calcium oxide is usually used as CO_2 sorbent due its sorption capacity, low cost and adding inert materials guarantees more stability to it by avoiding the sintering process. Therefore, given the relevance of this process from a technical and operational point of view, this catalytic system may be very promising and deserves further investigation.

CHAPTER 3. MATERIALS AND METHODS

3.1. Materials and equipment

Reactants used in the preparation of the catalysts:

- Nickel nitrate (II) hexahydrate ($Ni(NO_3)_2 \cdot 6H_2O$) (97.0%) – Vetec;
- Calcium nitrate tetrahydrate ($Ca(NO_3)_2 \cdot 4H_2O$) (99.0%) – Dinâmica;
- Magnesium nitrate hexahydrate ($Mg(NO_3)_2 \cdot 6H_2O$) (98.0%) – CAAL;
- Aluminum nitrate nonahydrate ($Al(NO_3)_3 \cdot 9H_2O$) (98.0%) – Nuclear;
- Anhydrous citric acid ($C_6H_8O_7$) (99.5%) – Dinâmica;
- Ethylene glycol ($C_2H_6O_2$) (99.5%) – Dinâmica;
- Distilled water.

Gases and reactants used in the characterization and in the CO_2 capture of the catalysts:

- Argon (99.99%) – White Martins;
- Gas mixture containing 1.96% H_2 in Argon (99.99%) – White Martins;
- Helium (99.99%) – White Martins;
- Carbon dioxide (99.99%) – White Martins;
- Synthetic air (99.99%) – White Martins;
- Nitrogen.

Gases and reactants used in the catalytic tests:

- Ethanol (95.0%) – Neon;
- Hydrogen (99.99%) – White Martins;
- Argon (99.99%) – White Martins;
- Distilled water.

Equipment used:

- Laboratory glassware in general (mortar with pestle, crucibles, beaker and so on);
- Analytical balance (Shimadzu ATX224);
- Magnetic stirrer with heating (IKA C-MAG HS 7);
- Oven with airflow (Brasdonto - model 3);
- Muffle furnace with airflow (Fornitec - number 3331);
- X-ray diffractometer (Shimadzu Lab X – XRD-6000);
- High pressure pump for liquid (Shimadzu LC-20AT);
- K-type thermocouple;
- Temperature controllers (ThermaTH 91 DP 203-000 and NOVUS N1040);
- Gas chromatograph (Shimadzu GC-2014 and GC-17A);
- Quartz fixed-bed reactor;
- Ceramic furnace;
- Unit for catalytic tests;
- Thermogravimetric Analyzer (Shimadzu TGA–50);
- NOVAtouch Gas Sorption Analyzer LX1 (Quantachrome instruments).

3.2. Preparation of the catalysts

The experimental procedures to prepare the catalysts by sol-gel method were based on Tian et al. (2020). This method was chosen due to the formation of a porous microstructure that favors the diffusion of CO_2 into the CaO particle, improving cyclic stability and reactivity (Xu et al., 2016). Anhydrous citric acid and the precursors salts $Ca(NO_3)_2 \cdot 4H_2O$, $Mg(NO_3)_2 \cdot 6H_2O$, $Al(NO_3)_3 \cdot 9H_2O$ and $Ni(NO_3)_2 \cdot 6H_2O$ were dissolved into water considering a molar ratio anhydrous citric acid : water of 25 and magnetically stirred at 90 °C for 1 h. Then, ethylene glycol was added making the molar ratio of metal : anhydrous citric acid : ethylene glycol at 1:2:2, maintaining the continuous stirring at 90 °C until the gelation promoted by the removal of excess solvent. The obtained gel was dried overnight at 140 °C in an oven to remove water and causing the volume to increase considerably. The as-burnt product was calcined up to 450 °C at a heating rate of 1 °C/min, temperature was held for 4 h and then heated until 800 °C at 5 °C/min and

was kept constant for 2 h under airflow to remove the residual organic materials. The prepared catalysts were named as Ni/Ca and Ni/CaMgAl-X, where X represents the theoretical calcium content in the material. Table 3.1 shows the theoretical composition (wt%) of the prepared catalyst by sol-gel method.

Table 3.1. Theoretical composition (wt%) of the catalysts after calcination.

Catalyst	Ni (%)	CaO (%)	MgO (%)	Al_2O_3 (%)
Ni/Ca	10	90	-	-
Ni/CaMgAl-79	10	78.84	3.24	7.92
Ni/CaMgAl-68	10	67.68	6.48	15.84

3.2.1. Activation and passivation process

The calcined catalysts were firstly activated under a gas mixture atmosphere of H_2 (30 mL/min) and Ar (100 mL/min) from room temperature up to 800 °C at 10 °C/min, maintaining at this temperature for 1 h. After the activation time, the catalysts were cooled down until 0 °C by immersing the reactor into an ice bath with ethanol, following the passivation process. After 10 minutes, the samples were submitted to a mixture of 5% O_2/Ar at a flow rate of 30 mL/min for 30 minutes.

3.3. Characterization of the catalysts

3.3.1. X-Ray Diffraction (XRD)

X-ray diffraction (XRD) measurements were carried out using a Shimadzu Lab X-XRD-6000 diffractometer operated at 40 kV and 30 mA with CuKα radiation (λ =0.154 nm). Data were collected using the scan range (2θ) from 10 to 90°, steps of 0.02° and scan speed of 2°/min. This analysis aimed to determine the bulk crystalline structure of the materials and the average crystallite size by Scherrer equation (Equation 1.1), where d_n is the average crystallite size; K is the shape factor, taken as 0.90 in this work; λ is the wavelength of radiation in nanometer; θ is the diffracted angle of the peak; β is the full width at half maximum of the peak (FWHM) in radians.

$$d_n = \frac{K\,\lambda}{\beta \cos\theta}$$ Equation 3.1

Equation 3.2 was used to calculate metallic nickel dispersion (Thomas; Thomas, 2014). In this equation, D_{Ni} represents the metal nickel dispersion, MW_{Ni} is the molecular weight of nickel (58.6934 g/mol), N_A is the Avogadro constant ($6.022 \cdot 10^{23}$ mol^{-1}), r_p is the radius of the nickel metal particle (obtained by Equation 1.1), A_{Ni} is the area of the Ni^0 atom ($4.831 \cdot 10^{-20}$ m^2) e ρ_{Ni} is the nickel density (8908000 g/m^3).

$$D_{Ni} = \frac{3MW_{Ni}}{N_A \cdot r_p \cdot A_{Ni} \cdot \rho_{Ni}}$$ Equation 3.2

The XRD analysis were conducted for the calcined, passivated and spent materials.

3.3.2. Temperature Programmed Reduction (TPR)

H_2-TPR was performed in a quartz reactor which was heated by a furnace connected to a temperature controller. Approximately 100 mg of each sample was used. The samples were pretreated under Ar flow at 500 °C for 1 h and then cooled down to room temperature. The tests were conducted using a thermal conductivity detector with a mixture of 1.96% H_2 in Ar (30 mL/min), increasing the temperature from room temperature to 1000 °C at a heating rate of 10 °C/min. The experimental H_2 consumption was determined comparing the area below the peaks obtained during TPR with a calibration curve using the quantitative reduction of CuO to Cu^0. The degree of reduction was obtained by the ratio between experimental H_2 consumption and the theoretical one.

3.3.3. Scanning Electron Microscopy (SEM)

SEM analysis was used to verify the changes in the structure and surface of the catalysts before the sorption enhanced steam reforming of ethanol (fresh) and after 10 reactional cycles (spent). This technique can help to elucidate changes in the samples caused by sintering and carbon deposition on the surface. The samples were fixed in aluminum stubs with a double-sided carbon tape, sputter-coated with one thin layer of gold (approximately 56 nm) using a metallizer (SCD050, Leica) in order to avoid charging the catalysts due to the accumulation of electrostatic fields by increasing electrical conductivity. The morphology was investigated using scanning electron microscopy, EVO-MA10, ZEISS with a voltage setting of 20 kV and EHT (extra-high tension) mode. The SEM was also equipped with an Energy-Dispersive X-ray Spectroscopy (EDS) detector for the analysis of the individual chemical elements contained in the samples.

3.3.4. N_2 physisorption

The N_2 physisorption experiments were performed in surface area and porosity analyzer, model NOVAtouch Gas Sorption Analyzer LX1. Before the analysis, the samples were previously heated under vacuum at 333 K for 66 hours. Then, the sample weight was measured and the analysis started, and the N_2 physisorption on the solid was performed at liquid nitrogen temperature (77 K). The volume of N_2 adsorbed or desorbed was measured at different nitrogen partial pressure conditions by varying the concentration of this gas. Finally, determination of specific surface areas (Brunauer, Emmett and Teller Model – BET), volume (Barrett, Joyner and Halenda Model – BJH) and pore sizes were provided by the software installed in the equipment. This analysis was carried out for the catalyst before (fresh) and after (spent) the sorption enhanced steam reforming of ethanol.

3.4. Carbonation and decarbonation tests

The CO_2 capture capacity was evaluated using a thermogravimetric analyzer (TGA-50 from Shimadzu). A thermal pretreatment was performed before the carbonation/decarbonation cycles at 800 °C in order to remove impurities and moisture

from the samples. The carbonation cycle occurred at 600 °C during 30 minutes under 10.6 mL/min of diluted CO_2 in 60 mL/min of He. After that, CO_2 feed was stopped, remaining just the He flow rate and temperature was increased to 800 °C at 10 °C/min, maintaining constant during 10 minutes aiming to regenerate the material by converting $CaCO_3$ to CaO and releasing CO_2. After the decarbonation process, temperature was cooled down to 600 °C, starting a new cycle. A total of 20 carbonation/decarbonation cycles were performed for each sample.

Weight and temperature were monitored by the thermogravimetric analyzer during the carbonation and decarbonation cycles. These data were treated to determine the capture capacity for all the materials during carbonation process in each cycle according to Equation 3.3. In this equation, m_0 represents the sample weight at the beginning of the carbonation process of each cycle and m_t represents the maximum sample weight at the end of the carbonation process of each cycle.

$$Capture\ Capacity\left(\frac{g\ CO_2}{g\ cat}\right)=\frac{m_t-m_0}{m_0} \qquad \text{Equation 3.3}$$

Equation 3.4 was used to determine the CO_2 capture capacity by mass of CaO in the samples. In this equation, Y_{CaO} represents the theoretical weight fraction of CaO in each sample as shown in Table 3.1.

$$Capture\ Capacity\left(\frac{g\ CO_2}{g\ CaO\ in\ the\ catalyst}\right)=\frac{m_t-m_0}{m_0\cdot Y_{CaO}} \qquad \text{Equation 3.4}$$

3.5. Thermodynamics Analysis

A software developed by National Aeronautics and Space Administration (NASA), based on a Chemical Equilibrium with Applications (CEA) model was used in order to determine the equilibrium composition during sorption enhanced steam reforming of ethanol and steam reforming of ethanol (Gordon; Mcbride, 1994). This software is based on minimization of Gibbs free energy (g). This software uses the non-stoichiometric method to find the equilibrium composition using the minimization of the

Gibbs free energy based on the set of species assumed initially. This method has the following advantages: i) no need to define the reactions, ii) no divergence occurs through the computation, iii) no need to estimate the initial equilibrium composition (Mojaver et al., 2020).

According to Gordon and Mcbride (1994), the Gibbs energy for a mixture of NS species per kilogram of mixture is given by Equation 3.5, where μ_j represents the chemical potential per kilogram-mole of species j (n_j), as shown in Equation 3.6.

$$g = \sum_{j=1}^{NS} \mu_j n_j \qquad \text{Equation 3.5}$$

$$\mu_j = \left(\frac{\partial g}{\partial n_j} \right)_{T,P,n_{i \neq j}} \qquad \text{Equation 3.6}$$

The minimization of free energy is the condition for chemical equilibrium, which can be shown as the mass-balance represented by Equation 3.7, where λ_i are Lagrangian multipliers and a_{ij} are the number of kilogram-atoms of element i per kilogram-mole of species j. Equation *3.7* allows to determine the equilibrium composition for a thermodynamics state at a temperature (T) and pressure (P).

$$\mu_j + \sum_{i=1}^{NS} \lambda_i a_{ij} = 0 \qquad (j = 1, \ldots, NS) \qquad \text{Equation 3.7}$$

The species considered for the thermodynamics analysis for the steam reforming of ethanol were C_2H_5OH, H_2O, H_2, CO, CH_4, CO_2 and C(s). For the sorption enhanced steam reforming of ethanol, CaO(s) and $CaCO_3$(s) were also considered in addition to the species cited before. The assumed molar ratio steam/ethanol was 6 and pressure 1 atm, varying the temperature condition: 400, 500, 600, 700, 800 and 900 °C. The molar feed ratio steam/ethanol employed was 6 (twice the stoichiometric) because no carbon formation was found in any experimental runs with the molar ratio more than 3, one advantage compared to the conventional reforming as reported by (Aceves Olivas et al.,

2014). The pressure 1 atm was chosen because it is the atmospheric value and no need to increase it since higher pressure restrains hydrogen formation (Wang; Wang, 2008). For each temperature was determined the equilibrium compositions for all the species and Table 3.2 shows the feed molar ratio inserted in the Software for the thermodynamics analysis.

Table 3.2. Molar ratio inserted in the Software to simulate Steam Reforming of Ethanol (SRE) and Sorption Enhanced Steam Reforming of Ethanol (SESRE).

Reaction System	Feed Molar Ratio Steam : Ethanol : CaO
Steam Reforming of Ethanol (SRE)	6 : 1 : 0
Sorption Enhanced Steam Reforming of Ethanol (SESRE)	6 : 1 : 2

3.6. Catalytic tests

The catalytic tests were divided into three steps: reduction, reaction and decarbonation. The reduction occurred with 1.5 g of sample in the quartz reactor with a mixture of 30 mL/min of H_2 and 100 mL/min of Ar. The furnace was heated up to 800 °C at a heat rate of 10 °C/min and the temperature was held for 1 h. After the reduction step, the reactor was purged with Ar and the temperature was cooled down until 600 °C. A liquid solution with a molar ratio water : ethanol of 6:1 was pumped, evaporated forming a vapor phase with the following composition: 27 mL/min of water, 4.5 mL/min of ethanol and 100 mL/min of argon. When the reactants stream was stabilized, the reactants mixture was fed to the reactor. After 5 minutes, the quantification of the products was done by a Gas Chromatograph GC-2014 (Shimadzu) every 7 minutes. The sorption enhanced steam reforming of ethanol was performed at 600 °C, 1 atm, during 117 minutes. After the reaction step, the furnace was heated until 800 °C at 10 °C/min for 1 h under Ar atmosphere aiming to decompose $CaCO_3$, also known as the decarbonation (or regeneration) step. The reduction, reaction and regeneration steps are shown in Figure 3.1. The reaction and decarbonation steps were repeated 10 times in a cyclic process to monitor the performance of the catalysts. Figure 2.1 exhibits the experimental unit used

in this work, based on Zhao et al. (2017) sketch, since they used a similar reactional unit for sorption enhanced steam reforming of acetic acid.

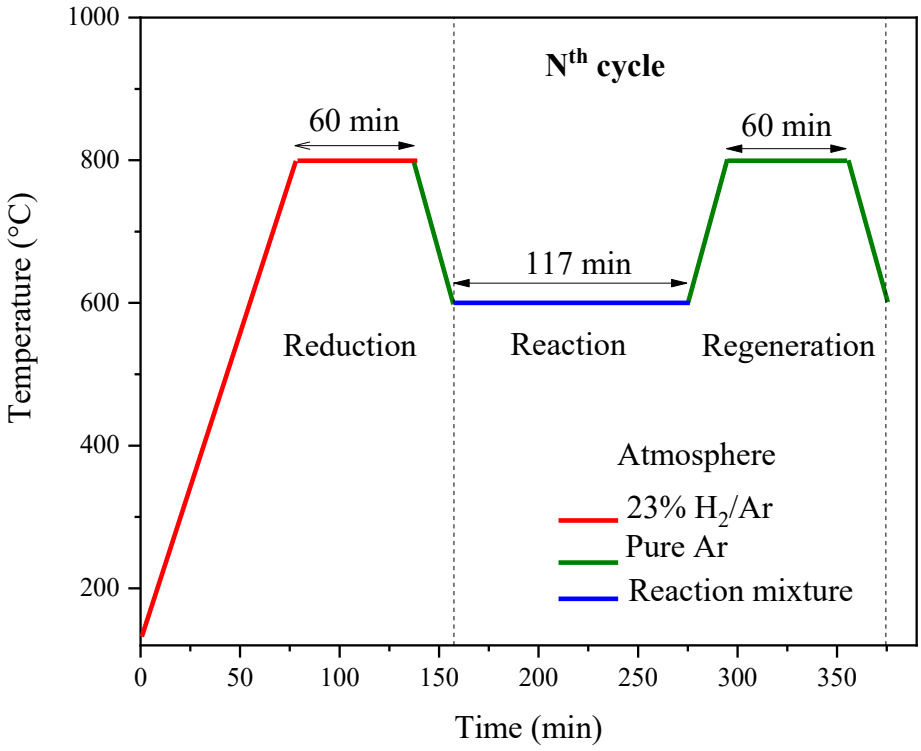

Figure 3.1. Scheme and reactional conditions for the catalytic tests.

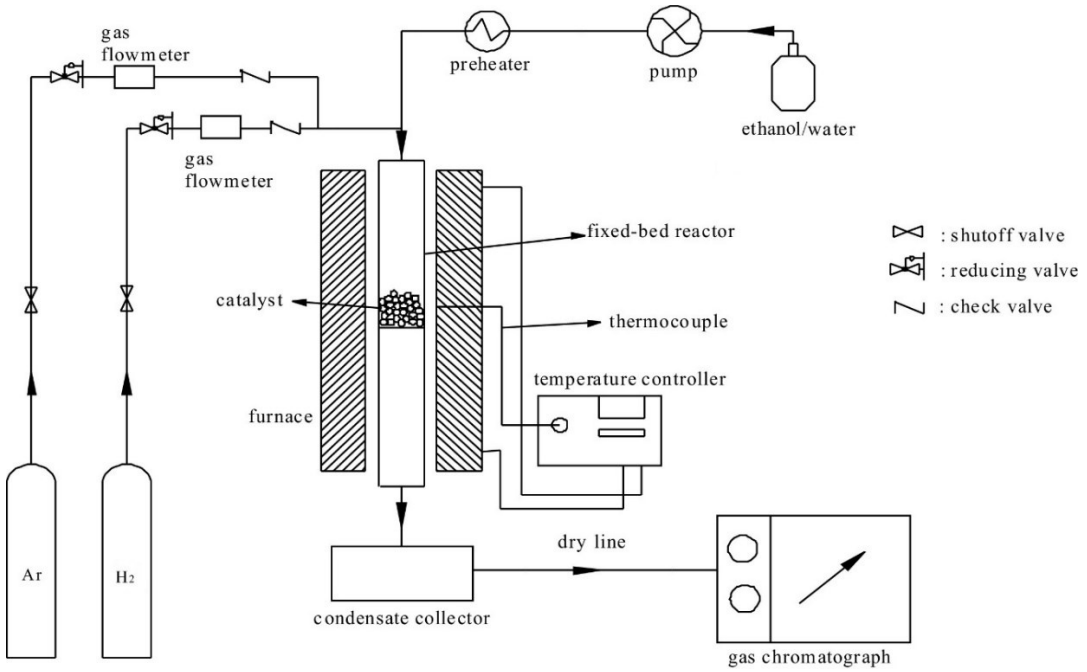

Figure 3.2. Representative scheme used during sorption enhanced steam reforming of ethanol, adapted from Zhao et al. (2017).

After each cycle of reaction and decarbonation, the products distribution and ethanol conversion were calculated. Equation 3.8 was used to determine the molar fraction of the products on dry basis, where y_i represents the molar fraction of each product in gas phase, n_i and n_j are the number of moles on dry basis, in gas phase, from the species i and j at the exit of the reactor and N represents the total number of species identified by the GC.

$$y_i = \frac{n_i}{\sum_{j=1}^{N} n_j}$$ Equation 3.8

For the ethanol conversion, the pumped solution was injected into the gas chromatograph before the beginning of the cycle (feed, with the reactor in the bypass position) and after each cycle (condensed solution), in order to obtain the number of moles of ethanol in the feed and at the exit of the reactor. Equation 2.2 was used to calculate ethanol conversion ($X_{C_2H_5OH}$), where $n_{C_2H_5OH}$ represents the number of moles of ethanol.

$$X_{C_2H_5OH}\ (\%) = \frac{(n_{C_2H_5OH})_{feed} - (n_{C_2H_5OH})_{exit}}{(n_{C_2H_5OH})_{feed}} \cdot 100$$ Equation 3.9

3.7. Thermogravimetric analysis after multiple reaction and decarbonation cycles

The thermogravimetric analysis (TGA) of the catalysts after 10 cycles of sorption enhanced steam reforming of ethanol, also known as spent catalysts, were performed in the TGA-50 from Shimadzu. Approximately 10 mg of the regenerated samples were inserted into the equipment and temperature was increased from room temperature to 900 °C at a heating rate of 10 °C/min with an atmosphere containing 15% O_2/He. Weight and temperature were monitored during all the process.

CHAPTER 4. RESULTS AND DISCUSSION

4.4. X-Ray Diffraction (XRD)

Figure 4.1 shows the diffractograms obtained at room temperature for the calcined samples. Ni/Ca catalyst presented CaO, $CaCO_3$, $Ca(OH)_2$ and NiO phases. For CaO (PDF 82-1691), the characteristic peaks are represented in 2θ equal to 37.4, 53.9 and 64.2°, with the corresponding planes (2 0 0), (2 2 0) and (3 1 1), respectively. $CaCO_3$ peak (PDF 4-636) was also detected in 43.0° with the plane (2 0 2) suggesting that $CaCO_3$ was incompletely decomposed to CaO and CO_2 during calcination at 800 °C. Due the high hygroscopicity of CaO, most of the peaks observed correspond to $Ca(OH)_2$ (PDF 81-2041) which diffraction angles are at 18.0, 28.7, 34.1, 47.1, 50.8, 71.8, 79.1 and 84.8° related to planes (0 0 1), (1 0 0), (1 0 1), (1 0 2), (1 1 0), (0 2 2), (1 1 3) and (0 1 4), respectively. Besides the previously mentioned phases, Ni/CaMgAl-79 and Ni/CaMgAl-68 catalysts showed diffraction peaks related to the MgO phase. The three samples also present NiO peaks (PDF 65-2901) at 37.1, 43.1, 62.6, 75.0 and 79.0° with the corresponding phases (1 1 1), (2 0 0), (2 2 0), (3 1 1), (2 2 2). Unfortunately, these diffraction peaks have coincidentally, the same 2θ values for MgO according to PDF 65-476. Probably there are NiO and MgO peaks overlapping in the Ni/CaMgAl-79 and Ni/CaMgAl-68 catalysts. Therefore, it is not possible to affirm that the MgO phase is present.

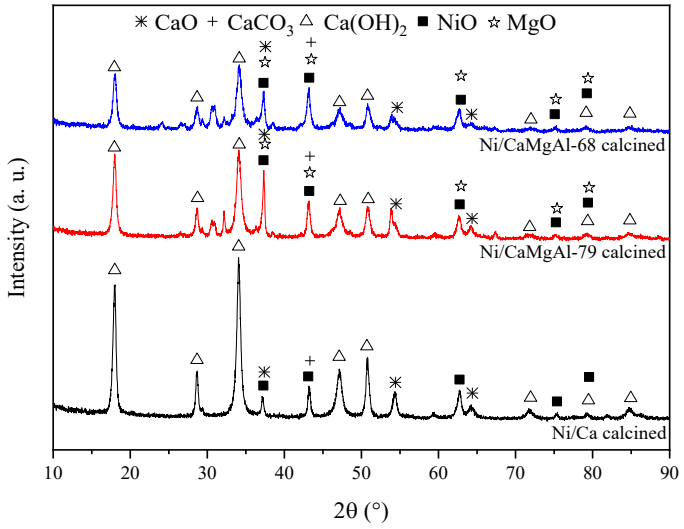

Figure 4.1. XRD patterns for the Ni/Ca, Ni/CaMgAl-79 and Ni/CaMgAl-68 calcined catalysts.

It is worth to point out that diffraction peaks related to Al_2O_3 phases were not detected. This is an indication that the aluminum added may have been converted to small amounts of other phases such as nickel aluminate spinel ($NiAl_2O_4$). Although the presence of small quantities of this kind of spinel as a surface species is difficult to be detected by XRD, it is considered to be the cause of a peak at high temperature in TPR of nickel catalysts (Di Giuliano et al., 2019).

Figure 4.2 displays XRD patterns obtained at room temperature for the passivated catalysts. After passivation process, the peaks that corresponds to reduced nickel appeared at 44.5, 51.8 and 76.4° (PDF 65-2865) which can be correlated to the respective planes (1 1 1), (2 0 0) and (2 2 0). It is also important to notice that $Ca(OH)_2$ phase was not presented in the passivated catalysts. CaO phase (PDF 82-1690) was present at 32.2, 37.4, 53.9, 64.2, 67.5, 79.8 and 88.7° with the planes (1 1 1), (2 0 0), (2 2 0), (3 1 1), (2 2 2), (4 0 0) and (3 3 1), respectively. $CaCO_3$ (PDF 4-636) had a single peak at 43.0° with the plane (2 0 2). The diffraction peaks detected at 37.1, 43.1 and 62.6° could be related to NiO which would suggest that nickel was not completely reduced. The presence of this oxidized nickel could be related to the passivation procedure. Unfortunately, the peaks observed at 37.1, 43.1 and 62.6° are also characteristic of CaO, $CaCO_3$ and MgO. Therefore, we could not rule out the presence of NiO phase, nor CaO, CaCO3, and MgO.

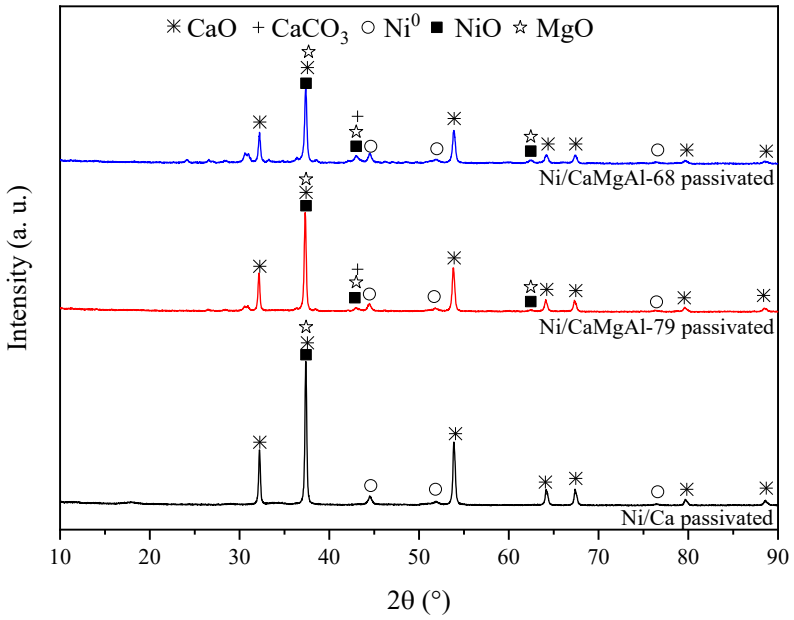

Figure 4.2. XRD patterns for the Ni/Ca, Ni/CaMgAl-79 and Ni/CaMgAl-68 passivated catalysts.

The average crystallite sizes of CaO and Ni^0 and the Ni^0 dispersion were calculated from the XRD data obtained for the passivated catalysts, using the Scherrer Equation. The results can be found in Table 4.1. It was not possible to calculate the average crystallite diameter for NiO, because the peaks for this phase are interfered by other phases that may be present (MgO, CaO and $CaCO_3$). The peak at $2\theta = 53.9°$ was used for the calculation of CaO average crystallite size and the one at $2\theta = 44.5°$ was used for Ni^0. The three catalysts showed CaO average crystallite sizes between 26–32.3 nm. For Ni^0 the three catalysts presented the same average crystallite sizes around 19 nm.

Table 4.1. Average crystallite size (CaO and Ni^0) for the passivated catalysts.

Catalysts	**Average crystallite size (nm)**		**Ni^0 dispersion (%)**
	CaO	Ni^0	
Ni/Ca	32.3	19.0	7.1
Ni/CaMgAl-79	29.5	19.3	7.1
Ni/CaMgAl-68	26.0	19.0	7.2

4.5. Thermogravimetric Analysis (TGA) for the calcined catalysts

Thermal pretreatment was performed in each sample in order to eliminate moisture, impurities, calcium hydroxide and calcium carbonate. The weight loss caused by the increase of temperature for the three calcined catalysts can be shown in Figure 4.3. The first weight loss between 350 and 500 °C is usually associated to the decomposition of $Ca(OH)_2$ (Klimesch; Ray, 1999).The second weight loss, between 550 and 700 °C, may be attributed to $CaCO_3$ decomposition (Wang et al., 2010). Ni/Ca catalyst presented the highest mass loss (21.6%), followed by Ni/CaMgAl-79 and Ni/CaMgAl-68 (17.1 and 14.8%, respectively), These differences are probably related to the decreasing order of the calcium content present in the catalysts (90, 78.84 and 67.68%, respectively).

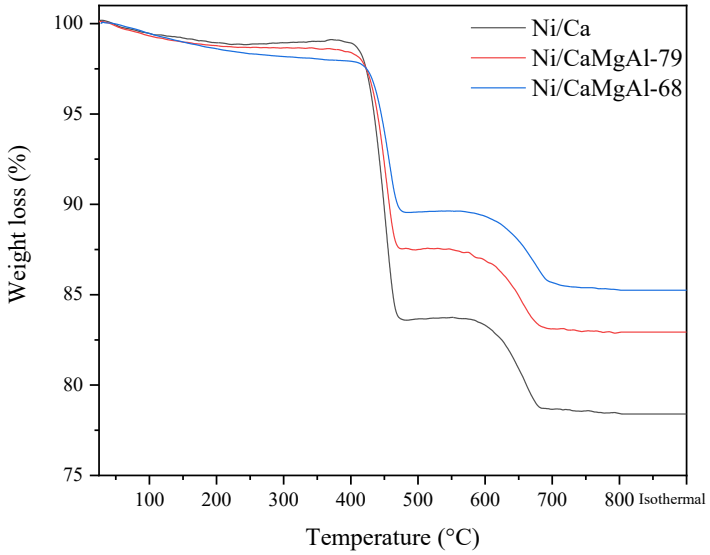

Figure 4.3. Thermogravimetric analysis obtained after thermal pretreatment from Ni/Ca, Ni/CaMgAl-79 and Ni/CaMgAl-68 catalysts under He atmosphere (50 mL/min). $T_{treatment}$ = 800 °C (10 minutes).

4.6. H_2-Temperature-programmed reduction (TPR)

Figure 2.1 displays TPR profiles obtained for Ni/Ca, Ni/CaMgAl-79 and Ni/CaMgAl-68 catalysts after calcination process. Ni/Ca catalyst presented two peaks at 489 and 628 °C. According to the literature, the lower temperature peak can be attributed to NiO that had weak interaction with CaO. The higher temperature peak can be associated to NiO that presented a stronger interaction with CaO (Sang et al., 2019). For Ni/CaMgAl-79 and Ni/CaMgAl-68 catalysts, the TPR profiles are very similar. The only differences are the peak intensity and the change of the reduction temperature. Both profiles exhibit two distinct peaks, a smaller one between 500 and 730 °C and a larger one between 750 and 1000 °C. The first half of the lower temperature peak can be associated to NiO interacting with CaO, as observed for Ni/Ca. As reported by Sang et al. (2019), the second half of the low temperature peak could be related to the reduction of $Ni_xMg_{1-x}O$. Since many MgO and NiO diffraction peaks have the same 2θ position, it was not possible to identify the formation of small amounts of this phase by X-ray diffraction. However, the formation of this phase has been previously reported in the literature for materials prepared in a similar way used in this present work. For the Ni/CaMgAl-79 catalyst, the formation of this mixed oxide phase would be less notable probably because this sample has a low theoretical MgO content (3.24 wt%). The larger

H_2 consumption peak, above 880 °C, could be associated to the reduction of $NiAl_2O_4$ spinel (Liu et al., 2020; Wu et al., 2012; Xu et al., 2021). The TPR patterns also showed that reducing the CaO content and adding Mg and Al increased the reduction temperature, making the catalysts more difficult to reduce.

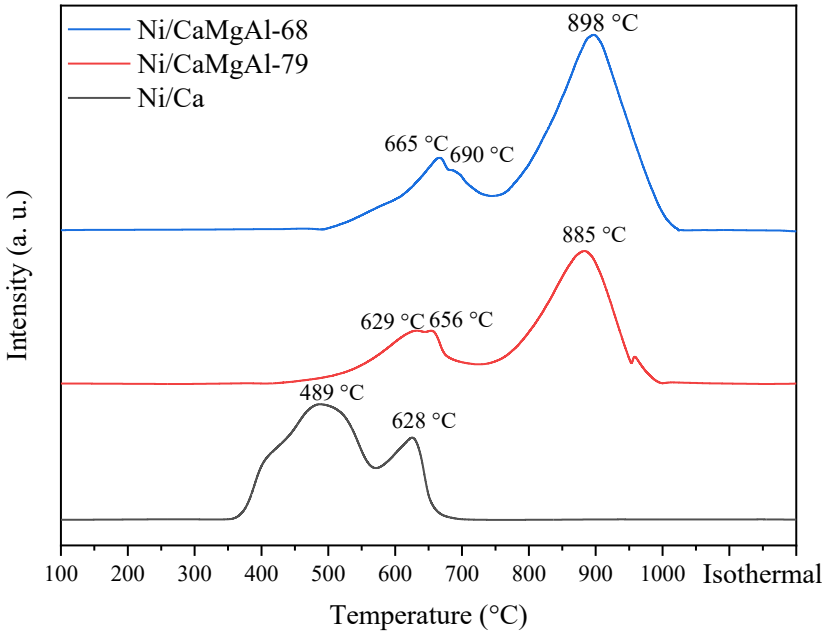

Figure 4.4. TPR of the calcined catalysts: Ni/Ca, Ni/CaMgAl-79 and Ni/CaMgAl-68.

TPR was also performed under the same temperature conditions used in the catalyst activation process preceding the SESRE reaction: the furnace was heated until 800 °C at a heating rate of 10 °C/min and kept at this temperature for 1 hour. This procedure was conducted in order to confirm that the catalyst activation conditions were appropriate for the catalytic tests. The TPR profiles obtained are presented in Figure 4.5.

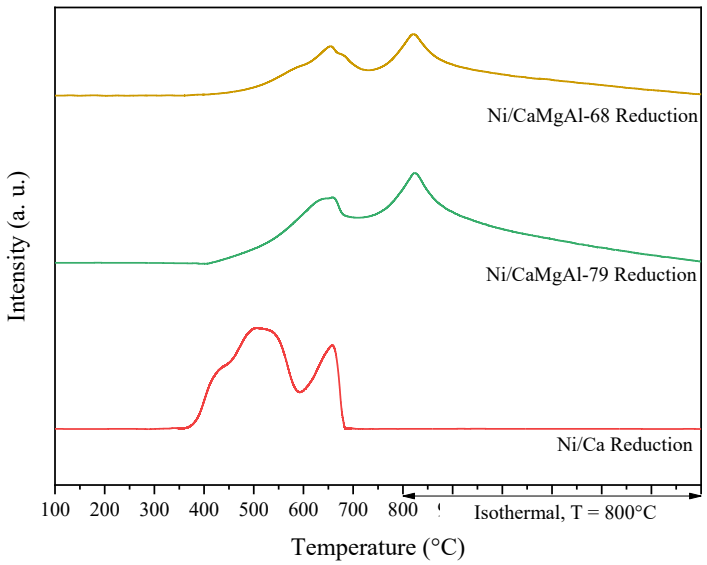

Figure 4.5. TPR of Ni/Ca, Ni/CaMgAl-79 and Ni/CaMgAl-68 catalysts under the same temperature conditions used in activation process that preceded catalytic tests.

The profiles obtained under activation conditions are similar to the standard ones presented in the Figure 2.1. The main difference is that there was an increase of H_2 consumption, since in these experiments, the catalysts remained for a longer time under hydrogen atmosphere. Table 4.2 shows experimental H_2 consumption and degree of reduction obtained during TPR procedure under the same temperature conditions used in activation process. The theoretical H_2 consumption for total NiO reduction in these samples is 13388 µmol/gcat.

Table 4.2. Experimental consumption of H_2 and degree of reduction of the catalysts during the TPR under the same temperature conditions used in activation process.

Catalyst	H_2 consumed (µmol/gcat)	Degree of Reduction (%)
Ni/Ca	12234	91
Ni/CaMgAl-79	14411	100
Ni/CaMgAl-68	12054	90

All the samples presented a degree of reduction above 90%, indicating that this condition is favorable to activate the catalysts. The majority of the nickel is in the reduced

form, which is the active phase for steam reforming of ethanol promoting the conversion of ethanol and water into high purity H_2. It is also worth noting that during catalytic tests, the hydrogen produced can promote reactivation of the sites that have been oxidized throughout the reaction cycles, which may help to maintain the catalytic activity. In addition, the TPR profiles using the same temperature conditions as the one used in the reduction process before catalytic tests showed that Ni/CaMgAl-79 catalyst achieved a degree of reduction of 100%.

4.7. Carbonation and decarbonation tests

The samples were submitted to carbonation and decarbonation cycles using thermogravimetric analysis. Figure 4.6 shows the results of carbonation and decarbonation for all the catalysts during 20 cycles. Ni/Ca catalyst (Figure 4.6a) presented a weight increase of 47.7% in the 1st cycle and 19.7% in the 20th. For Ni/CaMgAl-79 (Figure 4.6b), the weight increases were 31.7 and 24.2% in the 1st and 20th cycles, respectively. The Ni/CaMgAl-68 catalyst (Figure 4.6c) presented an increase of 22.3% in the 1st cycle and 17.7% in the 20th. These weight increases are attributed to the conversion from CaO to $CaCO_3$ during the carbonation cycle, when the sample is exposed to a diluted CO_2 flow. The decrease of CO_2 uptake capacity can be probably attributed to the incomplete conversion of $CaCO_3$ to CaO due to the sintering of CaO and the change of physical properties caused by the multiple carbonation-decarbonation cycles (Wu et al., 2012). The addition of inert materials possibly delays the sintering of CaO during calcination and contributes considerably to the CO_2 uptake capacity and stability, as reported by Wu et al. (2012) when adding aluminum to Ni/CaO. Table 4.3 summarizes the loss of CO_2 uptake capacity from the studied catalysts.

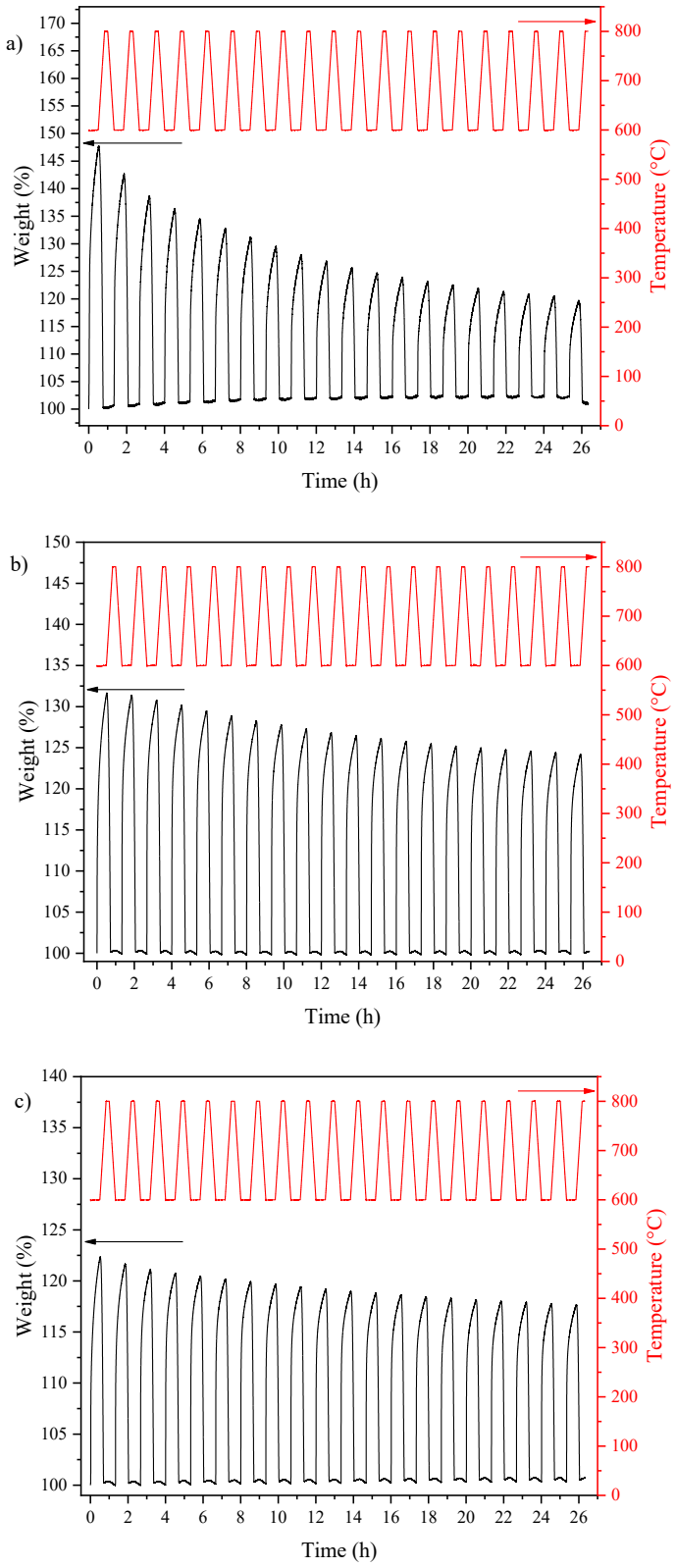

Figure 4.6. 20 carbonation and decarbonation cycles from: a) Ni/Ca, b) Ni/CaMgAl-79 and c) Ni/CaMgAl-68 catalysts. $T_{carbonation}$ = 600 °C (15% of CO_2 in He atmosphere), $T_{decarbnation}$ = 800 °C (pure He atmosphere).

Table 4.3. Loss of CO_2 uptake capacity from Ni/Ca, Ni/CaMgAl-79 and Ni/CaMgAl-68, comparing the 1st and 20th cycles.

Catalyst	1st cycle (gCO_2 / gCaO)	20th cycle (gCO_2 / gCaO)	Loss of CO_2 uptake (%)
Ni/Ca	0.53	0.19	64
Ni/CaMgAl-79	0.40	0.31	23
Ni/CaMgAl-68	0.33	0.26	21

From Figure 4.6 it was possible to calculate the amount of CO_2 absorbed per gram of catalyst (Figure 4.7a) over the 20 cycles. In the first 6 cycles, Ni/Ca catalyst presented the highest CO_2 capture capacity, which is consistent with the fact that this sample has the highest CaO content (90%), followed by Ni/CaMgAl-79 and Ni/CaMgAl-68. Ni/CaMgAl-79 catalyst presented almost the same CO_2 uptake capacity in the first 2 cycles, and this capacity suffered a slight decrease over the remaining cycles. In the seventh cycle, the sorption capacity of Ni/Ca was equal to the one observed for Ni/CaMgAl-79 catalyst. However, Ni/Ca sorption capacity continued to decrease sharply until the 18th cycle. At this point, both Ni/Ca and Ni/CaMgAl-79 presented similar CO_2 uptake capacities per gram of catalyst (Figure 4.7a). Ni/CaMgAl-68 catalyst had the lowest initial CO_2 capture capacity per gram of catalyst and it presented the smallest variation in CO_2 capture capacity between the first and last cycle, but it is not enough to be considered as the most stable catalyst.

In order to have a suitable comparison, the CO_2 sorption capacity was normalized by mass of CaO, considering the theoretical CaO content of Ni/Ca, Ni/CaMgAl-79 and Ni/CaMgAl-68 catalysts as 90, 78.84 and 67.68%, respectively. Figure 4.7b shows that in the first 3 cycles Ni/Ca catalyst has the highest CO_2 sorption capacity, similar to the behavior noted in Figure 4.7a. As the number of cycles increased, the ability to capture CO_2 of Ni/Ca catalyst decreased. This is probably due to the fact that this sample had no inert material in its composition. Therefore, the sintering process could not be avoided and this sample was the worst one in terms of CO_2 capture capacity at the end of 20 carbonation/decarbonation cycles. The best catalyst in terms of CO_2 capture capacity was Ni/CaMgAl-79, followed by Ni/CaMgAl-68. Both samples had the addition of spacers,

which play an important role in the stability of the catalyst, reducing its sintering and facilitating the molecular contact between CO_2 and CaO (Aceves Olivas et al., 2014).

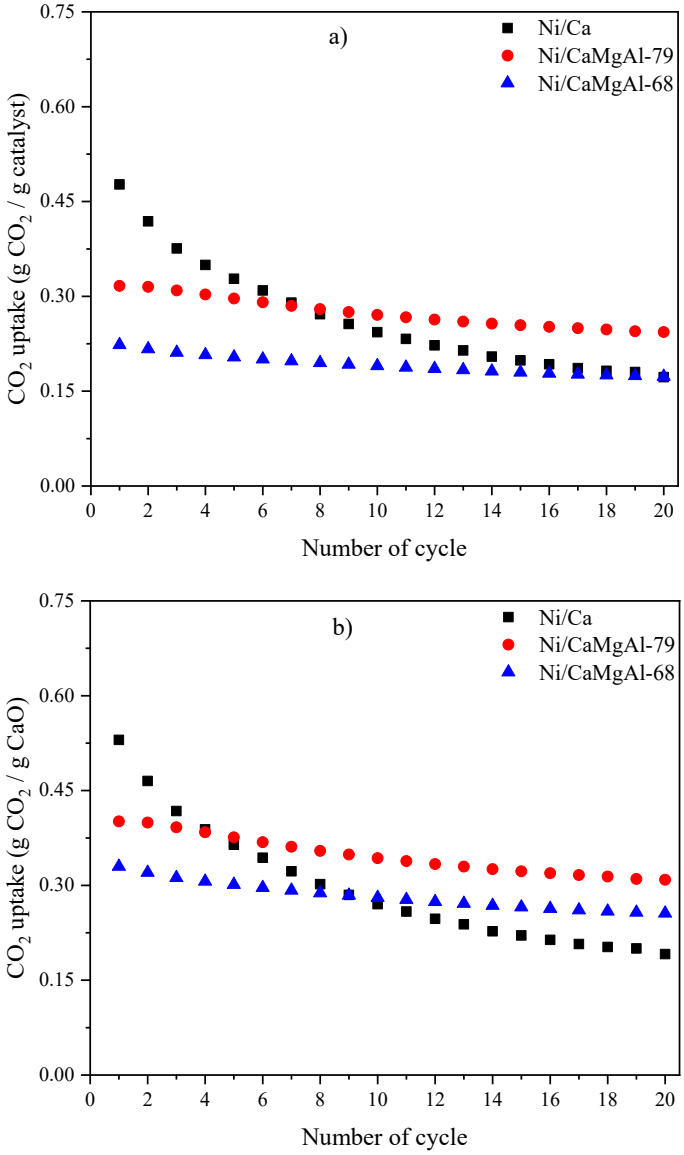

Figure 4.7. Comparison among CO_2 uptake capacity over 20 cycles from Ni/Ca, Ni/CaMgAl-79 and Ni/CaMgAl-68 catalysts, in mass of CO_2 by mass of: a) catalyst and b) CaO.

Loganathan et al. (2016) considered some models to describe CO_2 capture kinetics. One of them is the double-exponential model and it is feasible to explain kinetic

mechanisms that involves two steps: a rapid and a slow phase. The rapid phase is controlled by strong surface reactions (chemisorption of CO_2 on CaO) while the slow one is controlled by intra-particle CO_2 diffusion through the $CaCO_3$ external layer formed. The TGA data acquired (Figure 4.6) were adjusted by the double-exponential model given in Equation 4.1. The two exponential terms represent the two steps of the adsorption kinetics for an adsorbent: the rapid and the slow carbonation. In Equation 4.1, y represents the percentage of CO_2 adsorbed at a given time, t is time, A and B are pre-exponential factors, k_1 and k_2 represent the kinetic rate constant of the two adsorption steps and C is the percentage of CO_2 adsorbed at the equilibrium (Loganathan et al., 2016; Qi et al., 2013).

$$y = A \cdot e^{-k_1 \cdot t} + B \cdot e^{-k_2 \cdot t} + C \qquad \text{Equation 4.1}$$

Table 4.4 summarizes the kinetic parameters from all the three catalysts in the 1st and 20th cycles and the ratio k_1/k_2 and coefficient of determination (R^2). According to Guo et al. (2017) if k_1/k_2 value is more than 1, the CO_2 diffusion through an external layer of $CaCO_3$ to react with CaO is the controlling step. On the other hand, if k_1/k_2 is lower than 1, the surface reaction is the rate-determining step. Figure 4.8 shows the experimental data from TGA and the double-exponential model fitting for all the three catalysts.

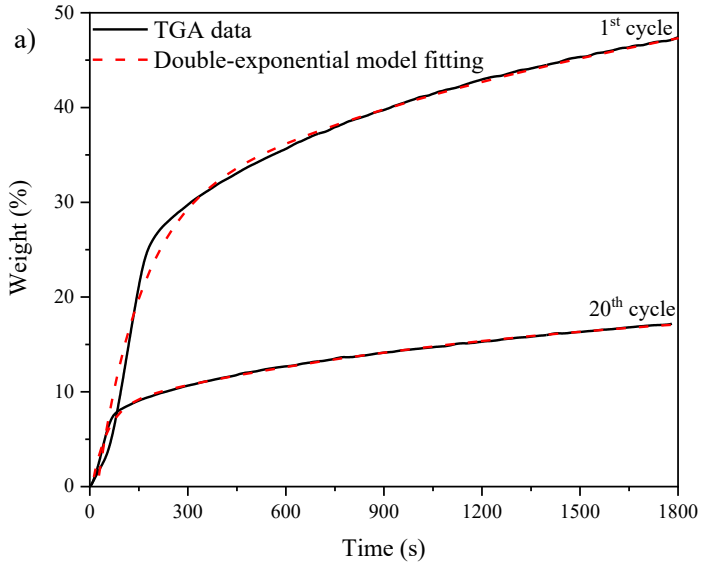

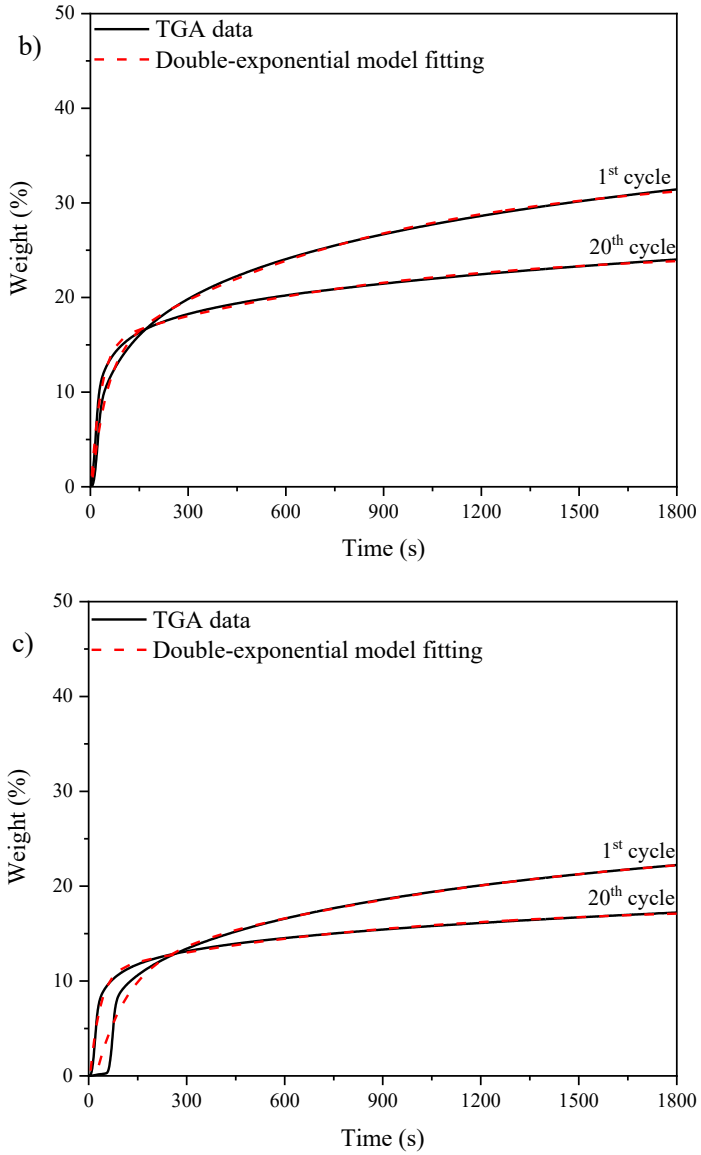

Figure 4.8. Experimental and double-exponential model fitting in the 1st and 20th cycles for a) Ni/Ca, b) Ni/CaMgAl-79 and c) Ni/CaMgAl-68 catalysts.

Table 4.4. Estimated parameters by the double-exponential model using TGA data for Ni/Ca, Ni/CaMgAl-79 and Ni/CaMgAl-68 catalysts, comparing the 1st and 20th cycles.

Catalyst	cycle	A	B	C	k_1 (s^{-1})	k_2 (s^{-1})	k_1/k_2	R^2
Ni/Ca	1st	-34.075	-32.378	60.502	0.0078	0.0005	15.600	0.992
	20th	-9.692	-11.936	20.278	0.0215	0.0007	30.714	0.998
Ni/CaMgAl-79	1st	-15.199	-19.698	33.503	0.0221	0.0012	18.417	0.998
	20th	-16.355	-9.970	25.088	0.0337	0.0012	28.083	0.996
Ni/CaMgAl-68	1st	-14.391	-14.640	25.687	0.0109	0.0008	13.625	0.988
	20th	-12.810	-7.045	18.020	0.0329	0.0011	29.909	0.994

As can be seen in Table 4.4, both 1st and 20th cycles indicated a k_1/k_2 value over 1 for all the three catalysts, which suggests that the CO_2 diffusion is the rate-limiting process. The k_1 value, that represents the chemisorption step, varied from 0.0078 to 0.337 s^{-1} whereas k_2 , that represents slow step (diffusion), had a variation from 0.0005 to 0.0012 s^{-1}. The following increasing order of k_1 and k_2 values was determined in both 1st and 20th cycles: Ni/Ca < Ni/CaMgAl-68 < Ni/CaMgAl-79 k_1 and k_2 values increased when comparing the 1st and 20th cycles for Ni/Ca and Ni/CaMgAl-68. However, Ni/CaMgAl-79 kept the same k_2 value for the 1st and 20th cycles (0.0012 s^{-1}). The smallest values for k_1 and k_2 were calculated for Ni/Ca catalyst, which is in agreement with the highest loss of CO_2 uptake capacity of this catalyst. The correlation coefficients for the fitting (R^2) are approximately 1, which indicates a good agreement between the double-exponential model and the experimental data, as shown in Figure 4.8.

Yoon, Mun and Lee (2021) used a deactivation model to fit the cyclic sorption data, which describes the sorbent activity in each cycle. This model allows to calculate the deactivation coefficients (k_d) of the materials based on Equation 4.2 as follows:

$$a = K \cdot e^{-k_d \cdot N} \qquad \text{Equation 4.2}$$

The parameter N represents the number of carbonation/decarbonation cycles, a indicates the sorbent activity at the Nth cycle (amount of CO_2 sorption uptake at the Nth cycle divided by 78.5 wt%, that is the maximum CO_2 sorption capacity of CaO) and the model pre-exponential factor is K. According to these researchers, the deactivation coefficient can indicate the degree of loss of the CO_2 sorption performance of the materials per cycle, and sorbents with lower values tend to have a higher cyclic stability. The calculated values of the deactivation model are presented in Table 4.5 for the three CaO-based sorbents. It is clear that Ni/CaMgAl-68, and Ni/CaMgAl-79 presented k_d values around 70% lower than Ni/Ca. It is notable that adding spacers to Ni/Ca lead to the decrease of the deactivation coefficient value, which means that the dopped catalysts are more stable, as expected.

Table 4.5. Estimated parameters by the deactivation model using TGA data for Ni/Ca, Ni/CaMgAl-79 and Ni/CaMgAl-68 catalysts.

Catalyst	K	$-k_d$	R^2
Ni/Ca	0.5777	0.0563	0.9566
Ni/CaMgAl-79	0.4065	0.0149	0.9794
Ni/CaMgAl-68	0.2791	0.0130	0.9680

4.8. Thermodynamics Analysis

Thermodynamics Analysis was performed to determine the equilibrium composition of the reactional system on dry basis using CEA Software (Snyder, 2021). This program employs the Gibbs free energy minimization technique, ensuring greater reliability in the results. The obtained data were compared to the literature in Figure 4.9. Collins-Martinez et al. (2013) carried out a thermodynamic modeling for steam reforming of light alcohols, including ethanol, at 300-800 °C and 1 atm, and the molar ratio (Steam:Ethanol:CaO) was varied from 3:1:2.5 to 6:1:2.5, keeping constant the amount of CaO. Molar ratio 5:1:2.5 and the range temperature 400-800 °C at 1 atm were chosen for comparison. The lines represent the molar fraction in dry basis obtained by Collins-Martinez et al. (2013) , whereas the symbols represent the results obtained using the CEA Software, in this present work. Collins-Martinez et al. (2013) reported that all the ethanol was consumed in these conditions, which was also observed in the simulation using the CEA Software. The molar fraction of the products found using the CEA Software and by Collins-Martinez et al. (2013) are similar as it can be observed in Figure 4.9.

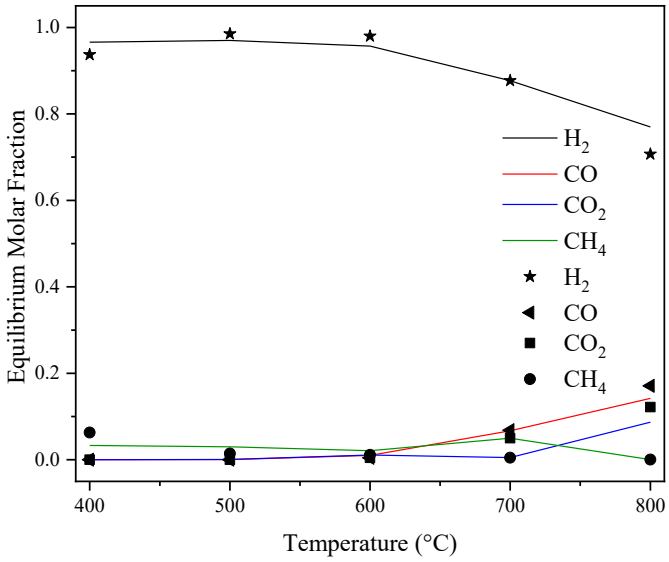

Figure 4.9. Thermodynamics Analysis – comparison between CEA Software and literature. Steam:Ethanol:CaO molar ratio = 5:1:2.5. Lines, (simulation obtained by Collins-Martinez et al. (2013)) and symbols (simulation obtained by CEA Software in this work).

Figure 4.10 shows the equilibrium composition for the Steam Reforming of Ethanol (SRE) and Sorption Enhanced Steam Reforming of Ethanol (SESRE) using CaO as a sorbent with a molar ratio Steam/Ethanol = 6. Since the values were very low (less than 0.53%), the equilibrium molar fraction of CH_4 and CO were omitted in order to have a better view of the data. For the SESRE, the equilibrium H_2 molar fraction was high up to 600 °C, followed by a slight decrease until 800 °C. For SRE, low temperatures do not favor high H_2 concentration and after 600 °C H_2 keeps approximately constant. Between 800 and 900 °C, the reaction $CaCO_3 \rightarrow CaO + CO_2$ is favorable, indicating that the sorption of CO_2 by CaO does not occur. At these high temperatures, the H_2 and CO_2 equilibrium molar fractions are alike for SESRE and SRE processes. From the thermodynamics analysis, it is possible to observe that the SESRE between 500 and 600 °C favors the high concentration of H_2. At 600 °C both SRE and SESRE presents the highest H_2 concentration and this explains why some researchers carries out the SESRE at this temperature with the molar ratio Steam/Ethanol = 6 (Aceves Olivas et al., 2014; Dou et al., 2018; Nimmas et al., 2019; Rahmanzadeh; Taghizadeh, 2019).

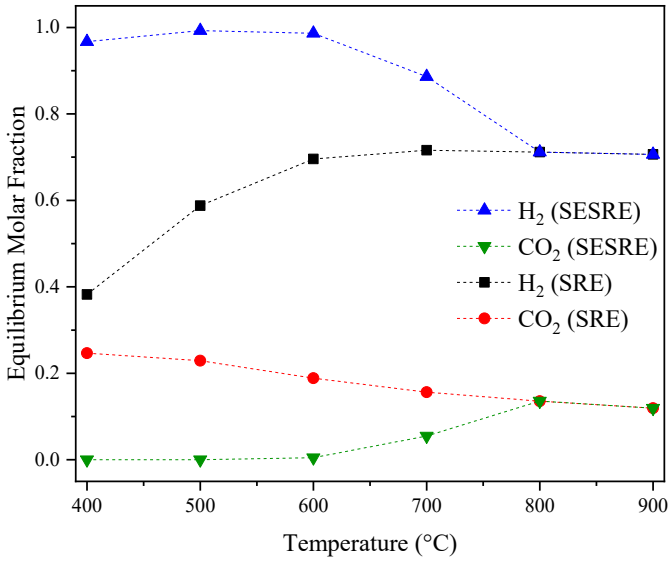

Figure 4.10. Equilibrium composition obtained by CEA Software, Steam Reforming of Ethanol (SRE) and Sorption Enhanced Steam Reforming of Ethanol (SESRE). Molar ratio Steam/Ethanol = 6 for SRE and Steam/Ethanol/CaO = 6:1:2 for SESRE.

Table 4.6 shows the molar fraction in the thermodynamics equilibrium, in dry basis, for the SESRE and SRE process. These values were used to compare to the molar fraction reached for all the species during catalytic tests. The results for the SESRE were used in the pre-breakthrough stage while the SRE were used in the post-breakthrough stage.

Table 4.6. Equilibrium composition obtained from thermodynamics analysis by CEA Software at 600 °C, 1 atm and molar ratio Steam/Ethanol = 6 for SRE and Steam/Ethanol/CaO = 6:1:2 for SESRE.

Molar Fraction	H_2 (%)	CO_2 (%)	CO (%)	CH_4 (%)
SESRE	98.64	0.49	0.35	0.53
SRE	69.58	18.89	8.15	3.38

4.9. Catalytic tests

The catalytic tests were carried out in 10 cycles of reaction and decarbonation for the SESRE of Ni/Ca, Ni/CaMgAl-79 and Ni/CaMgAl-68 catalysts. The ethanol

conversions for all of them were approximately 100% for all cycles. The main product was H_2 and the other products observed were CO_2, CO and CH_4. In Figure 4.11 - Figure **4.19**, regions I, II and III represent the pre-breakthrough, breakthrough and post-breakthrough periods, respectively. The dashed lines refer to the products distribution predicted by the thermodynamics analysis in the equilibrium.

Figure 4.11 - Figure **4.13** show the molar fractions of the products (dry basis) of the SESRE for the Ni/Ca catalyst in the 1st, 2nd and the 10th cycles, respectively. During the pre-breakthrough stage of the 1st cycle (Figure 4.11), the H_2 concentration reached values between 83.6 and 87.6%. The CO molar fraction was between 8.9 and 10.9%, followed by the minor products species (CH_4 and CO_2) with mean molar fractions of 3.3 and 1.2%, respectively. The pre-breakthrough duration was nearly 50 minutes and, in this stage, the CO_2 reacted with CaO, which can explain the low CO_2 concentration. In the breakthrough period, H_2 molar fraction decreased whereas CO and CO_2 increased and CH_4 maintained approximately the same. After 85 minutes, the reaction reached the post-breakthrough period, which indicates that the catalyst was saturated and the CO_2 capture was no longer occurring. In other words, only the steam reforming of ethanol was happening. In the post-breakthrough, the mean molar fractions of the products H_2, CO, CO_2 and CH_4 are 72.4, 15.8, 10.1 and 1.7%, respectively. The pre-breakthrough period lasted approximately 43 minutes in the 2nd cycle (Figure 4.12) and reached mean molar concentrations of 90.4, 7.3, 1.1 and 1.3% for H_2, CO, CH_4 and CO_2, respectively. The increase in hydrogen purity may be an indication that the catalytic system was previously in the induction period and then it was stabilized in the subsequent cycles. After 80 minutes of reaction (post-breakthrough), H_2 decreased to 72.2% and the concentration of CO, CH_4 and CO_2 were 15.0, 2.0 and 10.8%, respectively. In the 10th cycle (Figure 4.13), the H_2 and CO_2 mean molar fractions were 88.3 and 1.5% during the pre-breakthrough period. After 75 minutes of reaction (post-breakthrough), H_2 and CO_2 molar fraction decreased whereas CO increased, indicating that the reverse water-gas shift (RWGS) reaction is happening, since high temperatures (700 – 1000 K) favor this reaction (Abd El-Hafiz et al., 2015). Comparing the first and 10th cycle, the pre-breakthrough period decreased from 50 to 28 minutes and the post-breakthrough increased and started at 45 minutes, due to the loss of CO_2 uptake capacity.

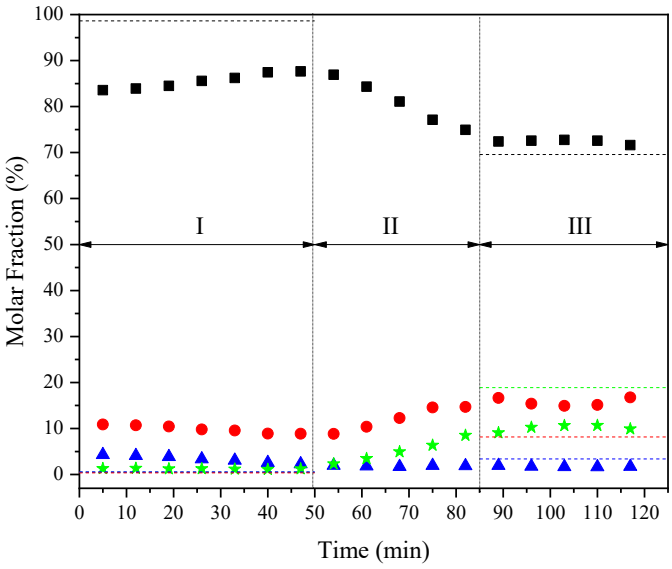

Figure 4.11. Product distribution from the SESRE for the Ni/Ca catalyst in the 1st cycle. Reactional conditions: $T_{reaction}$ = 600 °C, molar ratio steam/ethanol = 6, W/F = 11.41 min·mg_{cat}·mL^{-1}. Legend: ■: H_2; ●: CO; ▲: CH_4 and ★: CO_2.

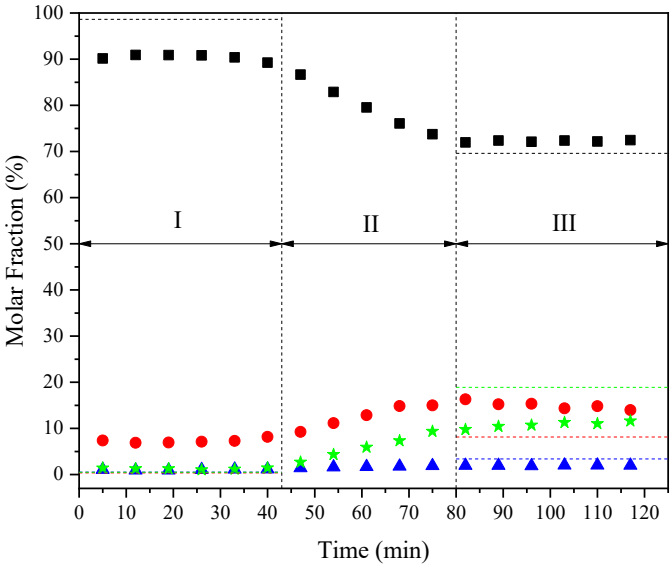

Figure 4.12. Product distribution from the SESRE for the Ni/Ca catalyst in the 2nd cycle. Reactional conditions: $T_{reaction}$ = 600 °C, molar ratio steam/ethanol = 6, W/F = 11.41 min·mg_{cat}·mL^{-1}. Legend: ■: H_2; ●: CO; ▲: CH_4 and ★: CO_2.

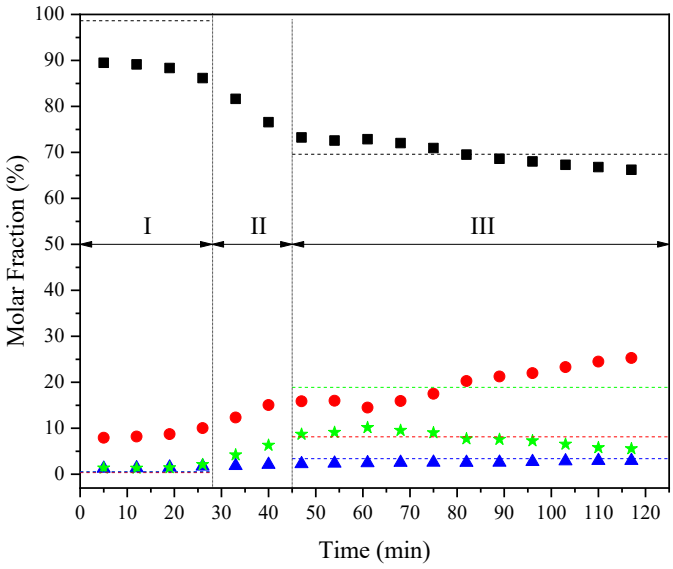

Figure 4.13. Product distribution from the SESRE for the Ni/Ca catalyst in the 10th cycle. Reactional conditions: $T_{reaction}$ = 600 °C, molar ratio steam/ethanol = 6, W/F = 11.41 min·mg_{cat}·mL^{-1}. Legend: ■: H_2; ●: CO; ▲: CH_4 and ★: CO_2.

Phromprasit et al. (2017) performed sorption enhanced steam reforming of biogas using a Ni-CaO catalyst. They used 0.5 g of sample and obtained H_2 molar fractions between 79 and 93 % in the pre-breakthrough period. The pre-breakthrough lasted about 30 min and high conversions to methane were obtained. In the post-breakthrough an average mole fraction of 60% for H_2 was achieved and methane conversion was slightly lower than the pre-breakthrough stage. In this work, Ni/Ca catalyst obtained H_2 molar fractions within the range cited by the authors during pre-breakthrough in the 10 reaction cycles. However, the present work had a longer pre-breakthrough period in the 1st cycle when compared to the authors. This is possibly due to the larger amount of catalyst in the reactor and the differences in the reaction systems. Furthermore, Ni/Ca catalyst had higher conversion and average H_2 concentration in the post-breakthrough during the reaction cycles comparing to the results found by the authors.

Figure 4.14 - Figure **4.16** exhibit the products distribution, in dry basis, of the SESRE for the Ni/CaMgAl-79 catalyst in the 1st, 2nd and the 10th cycles, respectively. In the 1st cycle (Figure 4.14) the mean H_2 molar fractions in the beginning (pre-breakthrough) and at the end (post-breakthrough) of the cycle are 83.6 and 73.1%, respectively. The CO varied from 11.0% in the beginning to 14.3 at the end of the cycle.

The CO_2 molar fraction was 2.2% during pre-breakthrough period and became 10.7% in the post-breakthrough period. The CH_4 species was 3.2% in the beginning of the cycle and decreased to 1.8% at the end of the cycle. In the 2nd cycle (Figure 4.15), the concentrations of H_2 and CO_2 were 86.1 and 1.8%, while CO and CH_4 had molar concentration of 9.9 and 2.2%, respectively, during the pre-breakthrough period. In the post-breakthrough period, the concentrations changed to 73.4, 13.7, 1.6, and 11.0% for H_2, CO, CH_4, and CO_2, respectively. In the 10th cycle (Figure 4.16) the H_2 molar fraction had a slight increase to 86.4% in the pre-breakthrough stage and a decrease to 71.9% in the post-breakthrough stage when compared to the 1st cycle. The other molar fraction values of the other species remained similar to the 1st cycle. The pre-breakthrough duration was 45 minutes in the 1st and 2nd cycles and was reduced to 30 minutes at the end of the 10th cycle. At the same time, the post-breakthrough started at approximately 80 minutes in the 1st cycle and maintained the same value up to the 10th cycle. Similar to the Ni/Ca catalyst, the decrease of the pre-breakthrough period is attributed to the reduction in the capture capacity of the catalyst over the reaction/decarbonation cycles. The strong metal-support interaction, shown in TPR profile, lead to stability when compared to the Ni/Ca catalyst Sang et al. (2019).

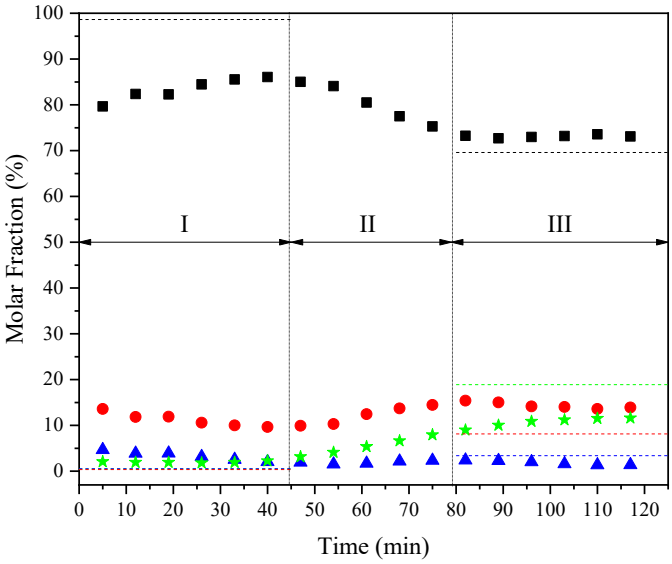

Figure 4.14. Product distribution from the SESRE for the Ni/CaMgAl-79 catalyst in the 1st cycle. Reactional conditions: $T_{reaction}$ = 600 °C, molar ratio steam/ethanol = 6, W/F = 11.41 min·mg_{cat}·mL^{-1}. Legend: ■: H_2; ●: CO; ▲: CH_4 and ★: CO_2.

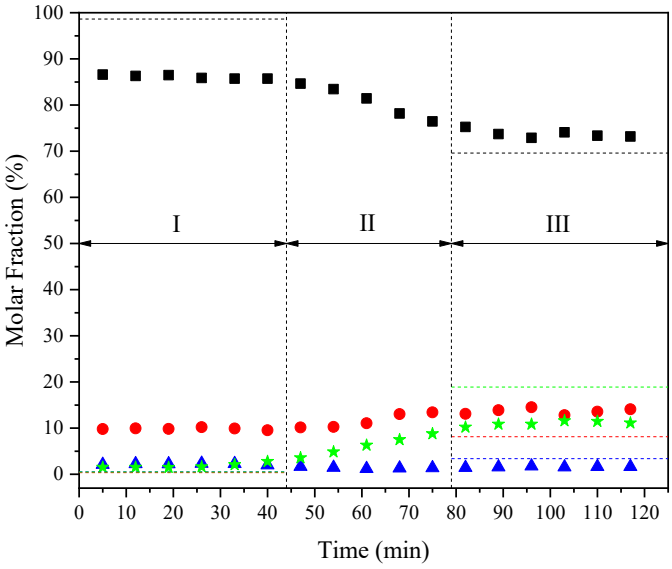

Figure 4.15. Product distribution from the SESRE for the Ni/CaMgAl-79 catalyst in the 2nd cycle. Reactional conditions: $T_{reaction}$ = 600 °C, molar ratio steam/ethanol = 6, W/F = 11.41 min·mg_{cat}·mL^{-1}. Legend: ■: H_2; ●: CO; ▲: CH_4 and ★: CO_2.

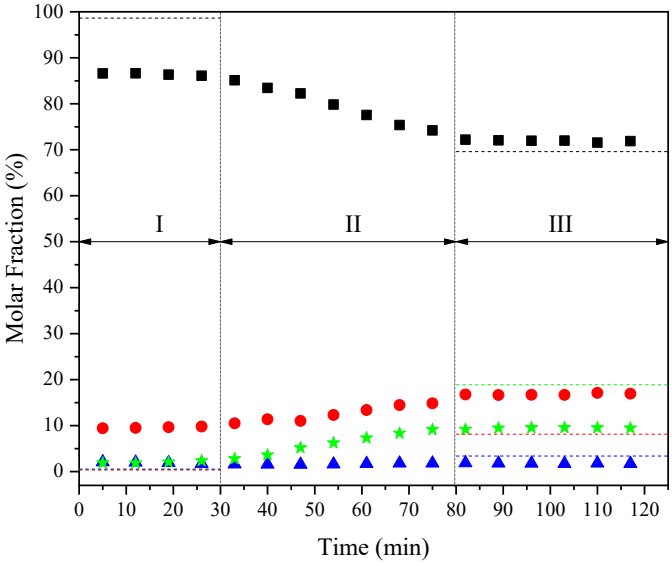

Figure 4.16. Product distribution from the SESRE for the Ni/CaMgAl-79 catalyst in the 10th cycle. Reactional conditions: $T_{reaction}$ = 600 °C, molar ratio steam/ethanol = 6, W/F = 11.41 min·mg_{cat}·mL^{-1}. Legend: ■: H_2; ●: CO; ▲: CH_4 and ★: CO_2.

Figure 4.17 - Figure **4.19** show the molar fractions of the products, in dry basis, in the 1st, 2nd and the 10th cycles, respectively, obtained during SESRE using Ni/CaMgAl-68 catalyst. The molar fraction in the pre-breakthrough stage in the 1st cycle (Figure 4.17) for H_2, CO, CH_4 and CO_2 were 83.2, 11.7, 3.0 and 2.1%, respectively. In this same order, the molar fraction of the species in the post-breakthrough were 73.3, 13.2, 1.6 and 11.9%. In the 2nd cycle (Figure 4.18), the molar fraction of H_2 was 86.8% in the pre-breakthrough period while for CO, CH_4 and CO_2 it was 9.4, 2.2 and 1.6%, respectively. In the post-breakthrough period, the concentrations became 74.0, 12.7, 1.3 and 12.0%. In the 10th cycle (Figure 4.19), the H_2 molar fraction increased to 90.6% in the pre-breakthrough period and had a decrease of the CO, CH_4 and CO_2 species, becoming 7.1, 1.0 and 1.3%, respectively. The molar fraction in the post-breakthrough for all the species in the 10th cycle remained almost the same when compared to the 1st cycle. The pre-breakthrough duration in the 1st cycle was 30 minutes and maintained the same until the 10th cycle, indicating that the addition of dopant material promoted an improvement in the cyclic stability of CaO. Besides, the post-breakthrough in the 1st cycle stared at nearly 79 minutes and was reduced to 59 minutes in the 2nd cycle and kept the same value until the 10th cycle.

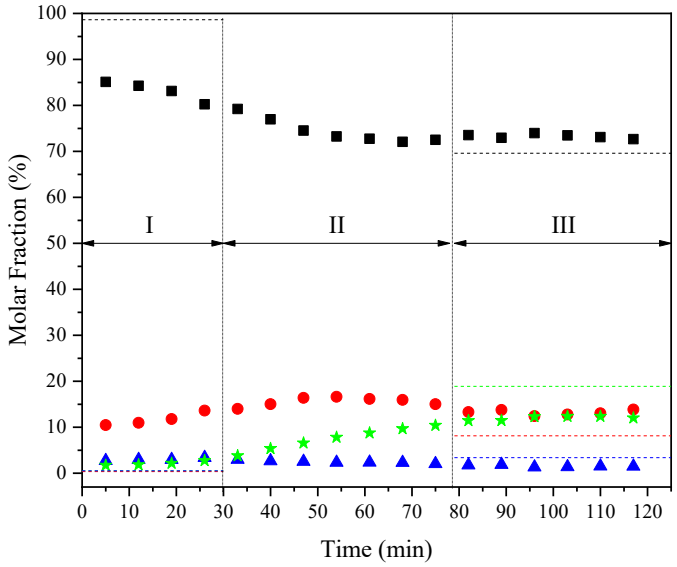

Figure 4.17. Product distribution from the SESRE for the Ni/CaMgAl-68 catalyst in the 1st cycle. Reactional conditions: $T_{reaction}$ = 600 °C, molar ratio steam/ethanol = 6, W/F = 11.41 $min \cdot mg_{cat} \cdot mL^{-1}$. Legend: ■: H_2; ●: CO; ▲: CH_4 and ★: CO_2.

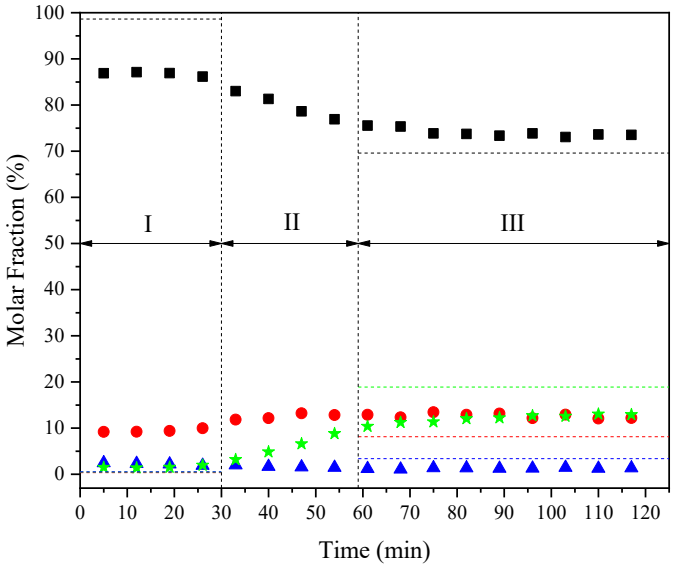

Figure 4.18. Product distribution from the SESRE for the Ni/CaMgAl-68 catalyst in the 2nd cycle. Reactional conditions: $T_{reaction}$ = 600 °C, molar ratio steam/ethanol = 6, W/F = 11.41 min·mg_{cat}·mL^{-1}. Legend: ■: H_2; ●: CO; ▲: CH_4 and ★: CO_2.

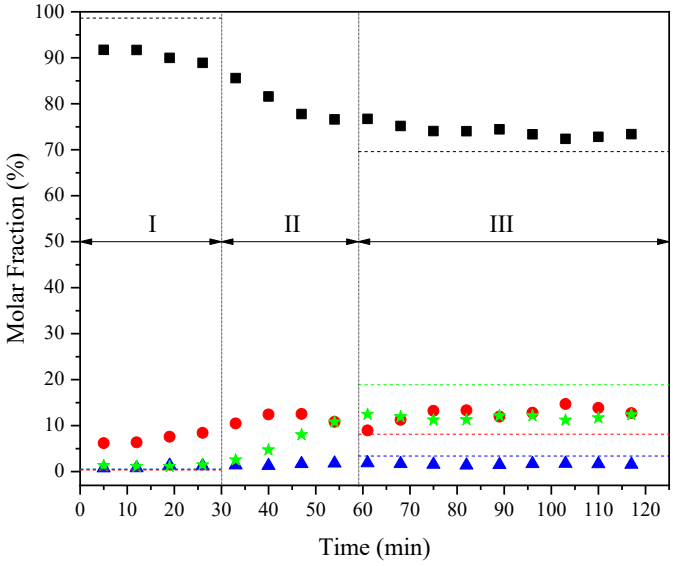

Figure 4.19. Product distribution from the SESRE for the Ni/CaMgAl-68 catalyst in the 10th cycle. Reactional conditions: $T_{reaction}$ = 600 °C, molar ratio steam/ethanol = 6, W/F = 11.41 min·mg_{cat}·mL^{-1}. Legend: ■: H_2; ●: CO; ▲: CH_4 and ★: CO_2.

The catalyst containing only Ni and CaO showed the longest pre-breakthrough period in the first cycle (approximately 50 minutes), when compared to the other catalysts. This fact is justified by the larger amount of CaO available for CO_2 capture. However, this excellent performance was not repeated in the next cycles. This decline in the capture capacity is related to the low Tammann temperature of $CaCO_3$, also indicating the need to add stabilizing material to the catalyst. These results corroborate with the Zhao et al. (2016), since they studied a similar catalyst, obtained 60 minutes in pre-breakthrough in the 1st cycle and 30 minutes in the 10th cycle over sorption enhanced steam reforming of methane reaction.

Dewoolkar and Vaidya (2016) studied SESRE using hydrotalcite-like materials (HTlc). The catalytic test was performed using NiMgHTlc and NiCaHTlc catalysts at 673 K and S/C = 9. The pre-breakthrough period in the 1st cycle was approximately 15 and 10 minutes, respectively. NiMgHTlc achieved 80% of hydrogen purity whereas NiCaHTlc had nearly 70%. Ca^{2+} probably needs to be available in the sample and not inserted into the structure in order to guarantee better CO_2 capture capacity. This explains why the authors obtained lower concentrations of hydrogen when compared to this work. In addition, NiMgHTlc catalyst was stable during 18 cycles at 573 K and S/C = 5. Performing SESRE at 773K and S/C = 10, NiCaHTlc remained stable during 6 multi-cycles. This characteristic of cyclic stability over reaction cycles is desired in sorption enhanced steam reforming reactions and can be seen in the performance of the catalysts doped with MgO and Al_2O_3 in this work.

Zhao et al. (2017) evaluated the catalytic activity of Ni/CaO-La_2O_3 in sorption enhanced steam reforming of acetic acid. The pre-breakthrough period decreased from 20 to 17.5 minutes with the increase of number of cycles from 1 to 9, showing the decline of CO_2 sorption capacity. This was due to the blockage of pores and increase of CaO particles caused by sintering phenomenon. Between the 1st and 7th cycles, this period was decreased from 20 to 18 minutes. However, between the 7th and 9th cycles, the pre-breakthrough period was kept unchanged at around 17.5 minutes. This catalyst improved its cyclic stability and had a small reduction in the CO_2 sorption capacity in SESR over nine cycles. The addition of dopants to the material is responsible for this enhancement, as reported by Dang et al. (2019). This reinforces the importance of using this technique in this work.

Figure 4.20 shows the maximum mole fraction of H_2 in each of the 10 reaction cycles at pre-breakthrough and post-breakthrough for all the catalysts studied. The molar fractions of the upper part represent the pre-breakthrough and the lower part the fractions at post-breakthrough. The dashed lines represent the equilibrium composition predicted by the thermodynamics analysis. The molar fractions obtained during the pre-breakthrough were below the thermodynamic limits and the ones measured during the post-breakthrough period were above the thermodynamic limits, for all cycles of the catalysts. In the 1st cycle all catalysts in the pre-breakthrough region had the lowest hydrogen concentrations, although these values increased and the reactional system stabilized from the 2nd cycle on.

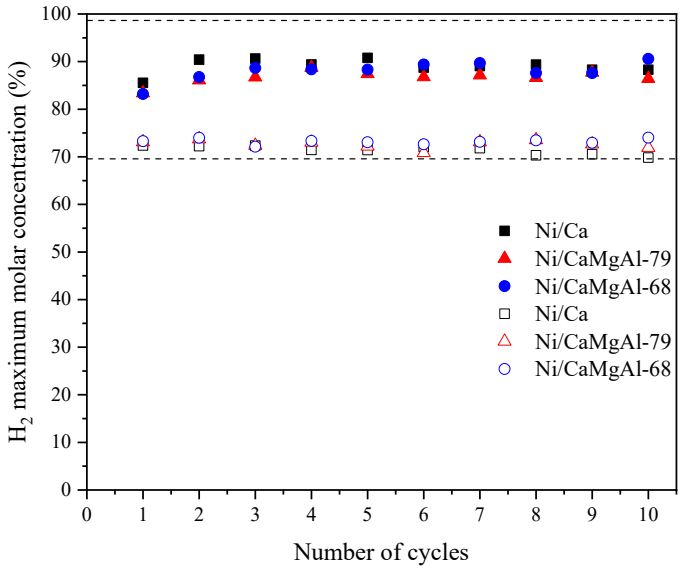

Figure 4.20. Hydrogen maximum molar concentration in the pre-breakthrough and post-breakthrough for each cycle in the SESRE reaction for the studied catalysts. Reactional conditions: $T_{reaction}$ = 600 °C, molar ratio steam/ethanol = 6, W/F = 11.41 $min \cdot mg_{cat} \cdot mL^{-1}$. Pre-breakthrough period (filled points) and post-breakthrough period (unfilled points).

4.10. X-Ray Diffraction (XRD) for the spent catalysts

In order to identify the existing phases in the catalyst after 10 reaction cycles, XRD of the spent catalyst was performed, as shown in Figure 4.21. XRD profiles of the used catalyst are quite similar to the calcined catalysts, although the intensities of the peaks related to NiO and MgO phases are lower than for observed for the calcined samples. Another important fact was the appearance of peaks referring to the Ni^0 phase

in all catalysts at 44.5, 51.8 and 76.4° (PDF 65-2865), showing that the catalysts remained with active sites even after the samples were exposed to air. There is the presence of peaks related to $CaCO_3$ phase, which is the result of CO_2 capture during the reaction. As observed for the calcined samples, the phase $Ca(OH)_2$ was also observed, which can be due to the hydration of CaO with water from the reaction or from exposure to air. As previously observed, we did not detect Al_2O_3 and $NiAl_2O_4$ phases nor the presence of $Ni_xMg_{1-x}O$ phase, although the formation of $NiAl_2O_4$ and $Ni_xMg_{1-x}O$ would be coherent with TPR results.

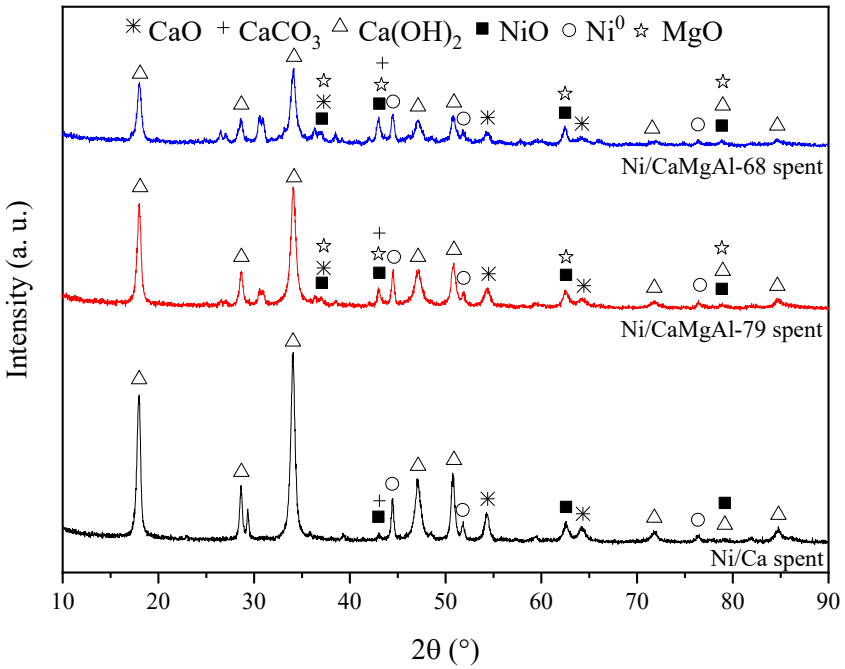

Figure 4.21. XRD patterns for the Ni/Ca, Ni/CaMgAl-79 and Ni/CaMgAl-68 spent catalysts.

4.11. Thermogravimetric analysis after multiple reaction and decarbonation cycles

The spent catalysts were analyzed by thermogravimetric analysis after regeneration process in order to perform the gasification of carbon deposited on the material during reaction. The results can be seen in Figure 4.22. The weight loss for Ni/Ca, Ni/CaMgAl-79 and Ni/CaMgAl-68 catalysts were 25.3, 18.5 and 15.5%, respectively. The first weight loss, around 410 °C, can be correlated to $Ca(OH)_2$ decomposition as shown in Figure 4.3 (Klimesch; Ray, 1999). The samples had a weight increase between 470 and 570 °C. According to the literature, this weight increase could indicate that CO_2 was formed by the oxidation of coke and then captured by the sorbent (Sang et al., 2019). This increase was used as evidence that there was carbon deposition

on the catalysts during ethanol reforming. The carbon deposit average rate, in mg of carbon by hour of reaction by gram of catalyst, was obtained considering 117 minutes each cycle (19.5 hours). Ni/Ca catalyst had the highest carbon deposit rate (11.5 $mgC/g_{cat}/h$) followed by Ni/CaMgAl-79 catalyst with 7.4 $mgC/g_{cat}/h$ and Ni/CaMgAl-68 with 6.2 $mgC/g_{cat}/h$. Besides improving the stability of the material, the addition of MgO and Al_2O_3 caused less carbon deposition when compared to pure CaO. Chen et al. (2018) evaluated carbon deposition in a series of Mg-modified Ni/Attapulgite catalysts (Ni/xMg-ATP) after steam reforming of ethanol reaction. Attapulgite is a hydrated magnesium aluminum silicate (presents Mg^{2+} and Al^{3+} on its composition, similar to the studied catalysts), which can be considered an interesting material to be compared. The authors found higher values for carbon deposition rate, which were 32.2, 29.8 and 12.7 $mgC/g_{cat}/h$ for Ni/ATP, Ni/5Mg-ATP and Ni/20Mg-ATP, respectively, suggesting the addition of MgO decreased the carbon deposition. According to them, filamentous carbon formation starts from the adjacent position of nickel particles and can be effectively extinguished due the strong interaction between support and active metal. Therefore, even after 10 SESRE reaction and decarbonation cycles, the catalysts of this work obtained lower weight loss during coke gasification and consequently achieved lower carbon deposition rate when compared to the steam reforming of ethanol reported by the researchers.

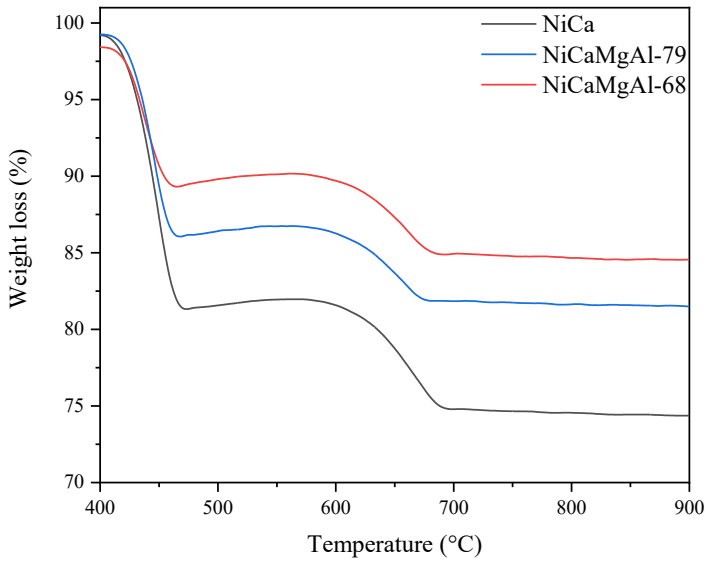

Figure 4.22. Weight loss for Ni/Ca, Ni/CaMgAl-79 and Ni/CaMgAl-68 spent catalysts during carbon gasification in the thermogravimetric analyzer under 15% O_2/He atmosphere.

4.12. N_2 physisorption

After the reaction cycles, N_2 physisorption technique (adsorption and desorption) was carried out for the textural characterization of the catalysts. The specific surface area was determined by N_2 adsorption fitted by the Brunauer-Emmet-Teller (BET) model and pore volume and size were estimated from the desorption isotherm, proposed by Barrett-Joyner-Halenda (BJH) (KIM et al., 2009). The adsorption and desorption isotherms can be seen in Appendix A. Table 4.7 presents the results obtained by N_2 physisorption for the fresh and spent catalysts.

Table 4.7. Textural properties of fresh and spent Ni/Ca, Ni/CaMgAl-79 and Ni/CaMgAl-68 catalysts obtained by N_2 physisorption analysis.

	Ni/Ca		**Ni/CaMgAl-79**		**Ni/CaMgAl-68**	
	fresh	**spent**	**fresh**	**spent**	**fresh**	**spent**
Specific surface area (m^2/g)	56	30	50	13	9	10
Pore volume (cm^3/g)	0.053	0.060	0.029	0.084	0.048	0.074
Pore size (nm)	1.8	1.9	1.9	1.9	1.9	1.9

For Ni/Ca catalyst the surface area decreased due to the sintering process, as expected. The other results are not shown because the analysis is still being performed.

4.13. Scanning Electronic Microscopy (SEM)

The Scanning Electronic Microscopy (SEM) analysis was carried out for the calcined and spent catalysts and the results can be seen in Figure 4.23. After the 10 reaction cycles Ni/Ca catalyst presented greater contact between the CaO particles, showing the sintering process of the material. This caused the increase of the particles and consequently the reduction of the specific surface area, which corroborates with the results found by the N_2 physisorption analysis. The catalysts doped with metal oxides, on the other hand, showed a well-preserved structure after the reaction when compared to the Ni/Ca catalyst. This is an expected behavior, because the inert ones acted as a physical barrier and minimized the sintering of CaO particles during the cycles (Xu et al., 2016). From the images, it was not possible to observe the apparent formation of filamentous carbon on the surface of the spent catalysts, one of the main causes of deactivation of

nickel-based catalysts in the reforming reactions by blocking the active sites. However, by TGA analysis for carbon gasification, the presence of small amounts of carbon on the surface was confirmed. The absence of filamentous carbon in the SEM analysis probably occurred due to the high amount of catalyst mass, since all the ethanol was converted before even reaching the end of the catalytic bed, resulting in the formation of coke in the sample in a non-homogenous way.

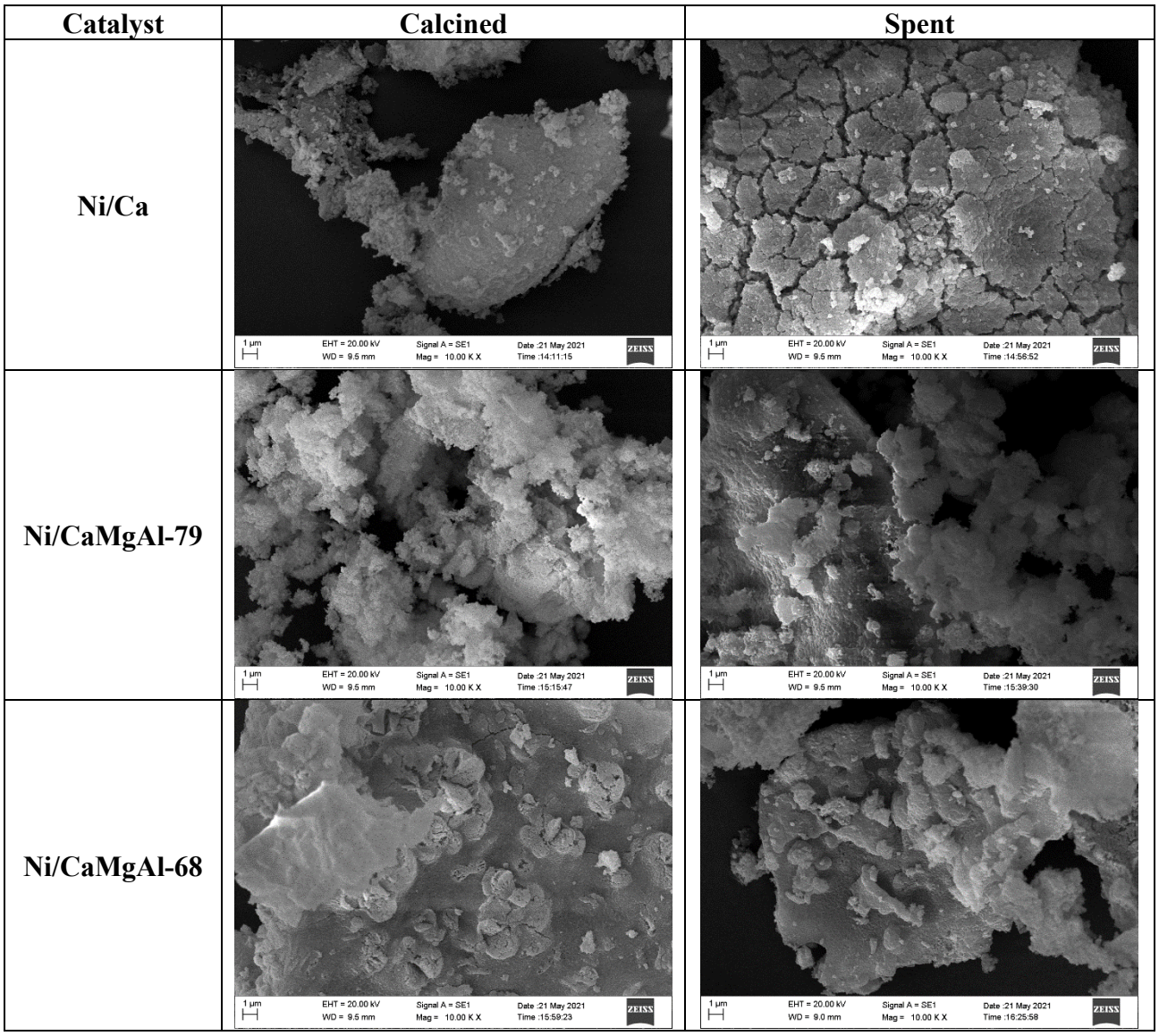

Figure 4.23. Scanning Electronic Microscopy of fresh and used catalysts. Magnification 10000 times.

Besides the SEM, the mapping of the elements present in the catalysts studied in this work was performed. Figure 4.24 and Figure **4.25** show the mapping for the fresh and spent catalyst that proved to be more stable throughout the catalytic tests.

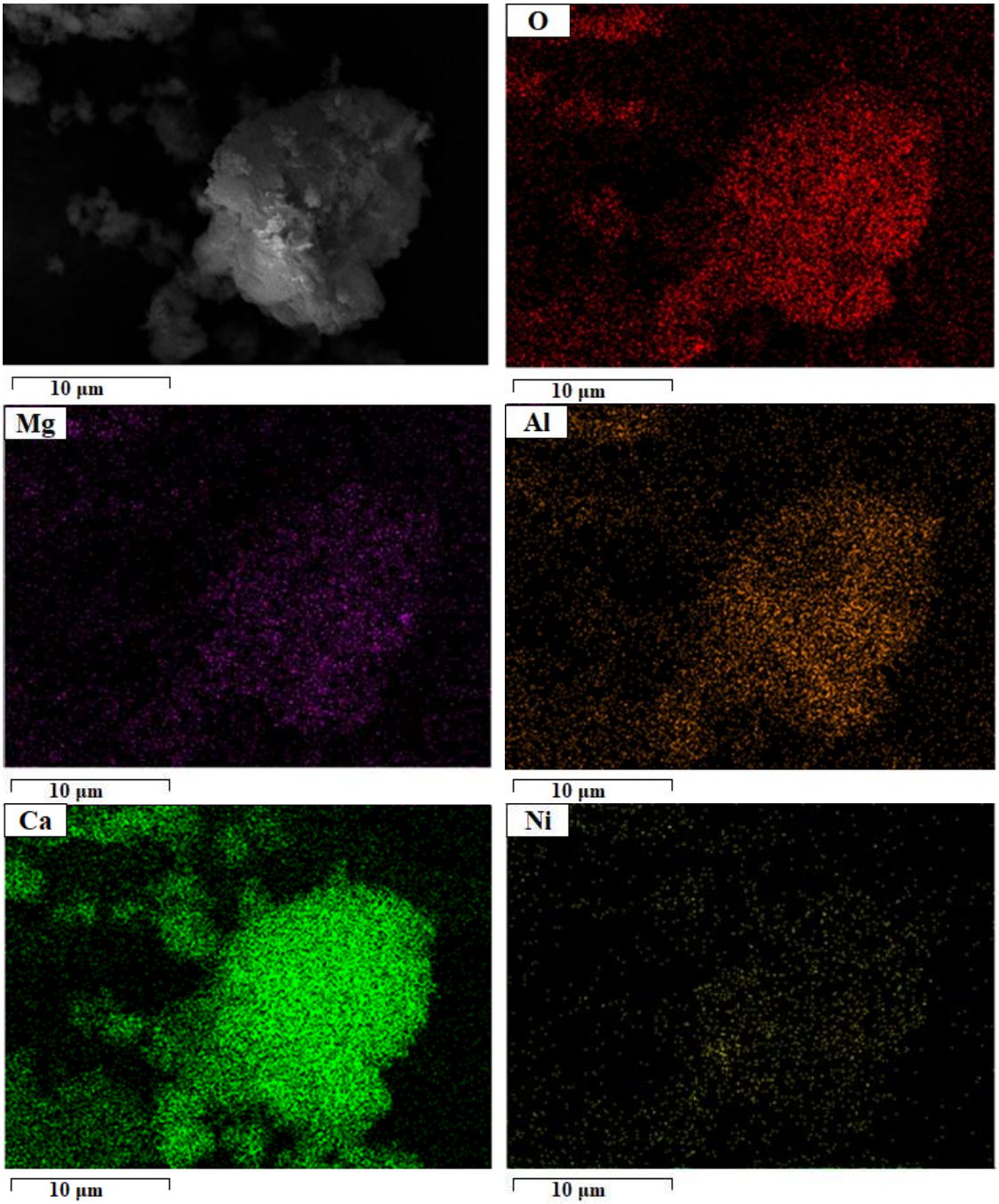

Figure 4.24. EDS mapping for the fresh Ni/CaMgAl-79 catalyst.

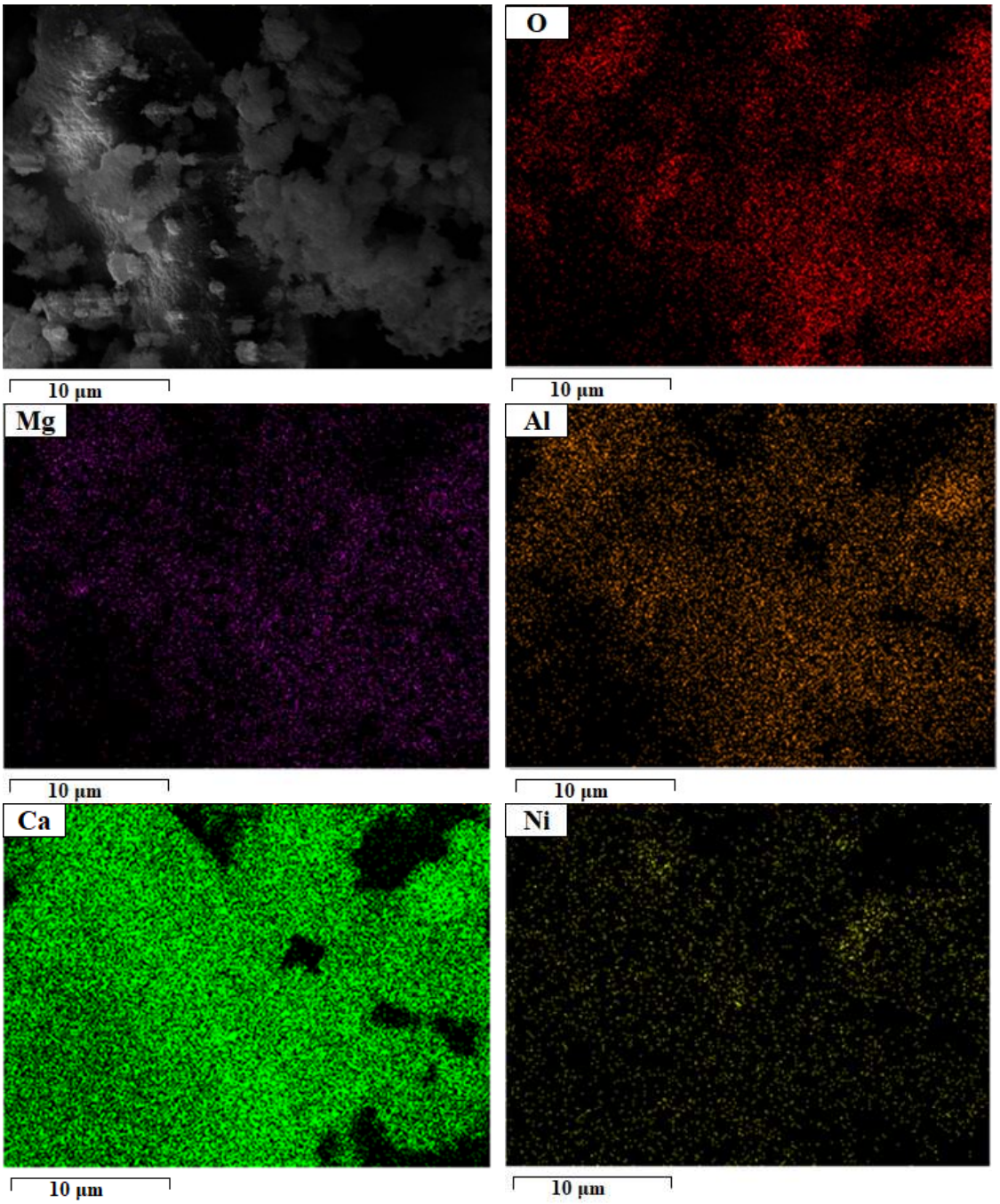

Figure 4.25. EDS mapping for the spent Ni/CaMgAl-79 catalyst.

From the EDS mapping, it was possible to notice that the dopant particles, MgO and Al_2O_3, are uniformly supported on the CaO particles and the nickel element, responsible for the reforming reaction, is well distributed throughout the material. According to Wang et al. (2015), the nickel present in the structure of $NiAl_2O_4$ can lead to high stability and good dispersion for the metal particles, which can be observed by EDS. The EDS mapping of the other fresh and spent catalysts are in Appendix B and show similar behavior.

CHAPTER 5. CONCLUSION AND SUGGESTIONS FOR FUTURE WORK

5.1. Conclusion

This work showed the effect of adding Mg and Al on the performance of Ni/CaO catalyst during SESRE process. XRD results showed the presence of CaO, NiO, $CaCO_3$, $Ca(OH)_2$ and NiO for calcined samples and Ni^0 for reduced ones. TPR profiles showed the occurrence of weak and strong interactions between NiO and CaO. The samples doped with Mg and Al presented a high temperature of reduction, which could indicate $NiAl_2O_4$ formation even though no characteristic peaks of this spinel were shown by XRD. TPR results also showed that the temperature used for catalyst activation was sufficient to ensure a high degree of Ni reduction. The TGA evaluated the effect of the addition of inert materials into CaO during 20 carbonation and decarbonation cycles. Although Ni/CaMgAl-68 showed higher stability, in terms of CO_2 capture capacity, Ni/CaMgAl-79 showed the best result after the cycles, both in terms of gcat and gCaO. The results showed that the addition of these dopants increased cyclic stability and reduced the loss of CO_2 uptake capacity.

In the catalytic tests, all samples achieved an ethanol conversion of 100% for all the 10 cycles, as expected, due to the high amount of catalyst added into the reactor. In the 1st cycle, Ni/Ca catalyst was the one that had the longest pre-breakthrough period (50 min), but by the end of 10 cycles, this time was reduced to less than 30 minutes. The sample Ni/CaMgAl-79 also presented some loss of duration from 45 minutes in the first cycle to 30 minutes in the 10th cycle. Only Ni/CaMgAl-68 catalyst maintained constant the pre-breakthrough period over the 10 cycles of reaction and decarbonation (30 min). However, this catalyst had low capture capacity right in the first cycle, which justifies the small loss in sorption capacity during SESRE, as confirmed by TGA. For all the catalysts, the H_2 mean molar fraction, in dry basis, was almost the same in the 1st cycle during pre-breakthrough stage. Furthermore, Ni/Ca and Ni/CaMgAl-79 catalysts had a slight increase in the H_2 molar fraction during pre-breakthrough of the 10th cycle. TGA of the spent catalysts showed that there was carbon formation on the surface of the material, however no filamentous carbon could be observed by SEM. The textural analysis indicated that there was sintering of the Ni/Ca sample through the decrease of its specific

surface area, which can be confirmed by showing a larger particle in SEM analysis. The results showed that doping Ni/Ca catalyst with Al and Mg may lead to materials with higher stability, which can be advantageous for SESRE processes.

5.2. Suggestions for future work

- Study the addition of metallic oxides (such as MgO, Al_2O_3, CeO_2, La_2O_3, Y_2O_3) as dopants in industrial waste with CO_2 capture capacity.
- Perform catalytic tests using other types of doped sorbents, such as Li_4SiO_4, Li_2ZrO_3 and Na_2ZrO_3.
- Study sorption enhanced steam reforming of other molecules, such as acetic acid, phenol, glycerol.

REFERENCE

ABD EL-HAFIZ, Dalia R.; EBIAD, Mohamed A.; ELSALAMONY, Radwa A.; MOHAMED, Lamia S. Highly stable nano Ce-La catalyst for hydrogen production from bio-ethanol. **RSC Advances**, *[S. l.]*, v. 5, n. 6, p. 4292–4303, 2015. DOI: 10.1039/c4ra12679c.

ACEVES OLIVAS, D. Y.; BARAY GUERRERO, M. R.; ESCOBEDO BRETADO, M. A.; MARQUES DA SILVA PAULA, M.; SALINAS GUTIÉRREZ, J.; GUZMÁN VELDERRAIN, V.; LÓPEZ ORTIZ, A.; COLLINS-MARTÍNEZ, V. Enhanced ethanol steam reforming by CO2 absorption using CaO, CaO∗MgO or Na_2ZrO_3. **International Journal of Hydrogen Energy**, *[S. l.]*, v. 39, n. 29, p. 16595–16607, 2014. DOI: 10.1016/j.ijhydene.2014.04.156.

ASHOK, Jangam; DEWANGAN, Nikita; DAS, Sonali; HONGMANOROM, Plaifa; WAI, Ming Hui; TOMISHIGE, Keiichi; KAWI, Sibudjing. Recent progress in the development of catalysts for steam reforming of biomass tar model reaction. **Fuel Processing Technology**, *[S. l.]*, v. 199, n. May 2019, p. 106252, 2020. DOI: 10.1016/j.fuproc.2019.106252.

BEPARI, Sujoy; BASU, Sanchari; PRADHAN, Narayan C.; DALAI, Ajay K. Steam reforming of ethanol over cerium-promoted Ni-Mg-Al hydrotalcite catalysts. **Catalysis Today**, *[S. l.]*, v. 291, p. 47–57, 2017. DOI: 10.1016/j.cattod.2017.01.027.

BIČÁKOVÁ, Olga; STRAKA, Pavel. **Production of hydrogen from renewable resources and its effectivenessInternational Journal of Hydrogen Energy**Pergamon, , 2012. DOI: 10.1016/j.ijhydene.2012.05.047.

BOLATKHAN, Kenzhegul; KOSSALBAYEV, Bekzhan D.; ZAYADAN, Bolatkhan K.; TOMO, Tatsuya; VEZIROGLU, T. Nejat; ALLAKHVERDIEV, Suleyman I. **Hydrogen production from phototrophic microorganisms: Reality and perspectivesInternational Journal of Hydrogen Energy**Elsevier Ltd, , 2019. DOI: 10.1016/j.ijhydene.2019.01.092.

BRODA, Marcin; KIERZKOWSKA, Agnieszka M.; BAUDOUIN, David; IMTIAZ, Qasim; COPÉRET, Christophe; MÜLLER, Christoph R. Sorbent-enhanced methane reforming over a Ni-Ca-based, bifunctional catalyst sorbent. **ACS Catalysis**, *[S. l.]*, v. 2, n. 8, p. 1635–1646, 2012. DOI: 10.1021/cs300247g.

CAPA, A.; GARCÍA, R.; CHEN, D.; RUBIERA, F.; PEVIDA, C.; GIL, M. V.

On the effect of biogas composition on the H_2 production by sorption enhanced steam reforming (SESR). **Renewable Energy**, *[S. l.]*, v. 160, p. 575–583, 2020. DOI: 10.1016/j.renene.2020.06.122.

CESÁRIO, Moisés R.; BARROS, Braúlio S.; COURSON, Claire; MELO, Dulce M. A.; KIENNEMANN, Alain. Catalytic performances of Ni-CaO-mayenite in CO_2 sorption enhanced steam methane reforming. **Fuel Processing Technology**, *[S. l.]*, v. 131, p. 247–253, 2015. DOI: 10.1016/j.fuproc.2014.11.028.

CHEN, Dong; LIU, Chenlong; MAO, Yangyang; WANG, Wenju; LI, Tianle. Efficient hydrogen production from ethanol steam reforming over layer-controlled graphene-encapsulated Ni catalysts. **Journal of Cleaner Production**, *[S. l.]*, v. 252, 2020. a. DOI: 10.1016/j.jclepro.2019.119907.

CHEN, Fangyuan; TAO, Yongwen; LING, Huajuan; ZHOU, Cuifeng; LIU, Zongwen; HUANG, Jun; YU, Aibing. Ni-Cu bimetallic catalysts on Yttria-stabilized zirconia for hydrogen production from ethanol steam reforming. **Fuel**, *[S. l.]*, v. 280, n. June, p. 118612, 2020. b. DOI: 10.1016/j.fuel.2020.118612.

CHEN, Mingqiang; WANG, Yishuang; YANG, Zhonglian; LIANG, Tian; LIU, Shaomin; ZHOU, Zhongshan; LI, Xiaojing. Effect of Mg-modified mesoporous Ni/Attapulgite catalysts on catalytic performance and resistance to carbon deposition for ethanol steam reforming. **Fuel**, *[S. l.]*, v. 220, n. September 2017, p. 32–46, 2018. DOI: 10.1016/j.fuel.2018.02.013.

CHEN, Sai; PEI, Chunlei; GONG, Jinlong. Insights into interface engineering in steam reforming reactions for hydrogen production. **Energy and Environmental Science**, *[S. l.]*, v. 12, n. 12, p. 3473–3495, 2019. DOI: 10.1039/c9ee02808k.

COLLINS-MARTINEZ, Virginia; ESCOBEDO BRETADO, Miguel; MELÉNDEZ ZARAGOZA, Miguel; SALINAS GUTIÉRREZ, Jesús; ORTIZ, Alejandro Lopez. Absorption enhanced reforming of light alcohols (methanol and ethanol) for the production of hydrogen: Thermodynamic modeling. **International Journal of Hydrogen Energy**, *[S. l.]*, v. 38, n. 28, p. 12539–12553, 2013. DOI: 10.1016/j.ijhydene.2012.11.146.

DANG, Chengxiong; LIU, Liqiang; YANG, Guangxing; CAI, Weiquan; LONG, Juan; YU, Hao. Mg-promoted Ni-CaO microsphere as bi-functional catalyst for hydrogen production from sorption-enhanced steam reforming of glycerol. **Chemical Engineering Journal**, *[S. l.]*, v. 383, p. 123204, 2020. a. DOI: https://doi.org/10.1016/j.cej.2019.123204.

DANG, Chengxiong; WU, Shijie; CAO, Yonghai; WANG, Hongjuan; PENG, Feng; YU, Hao. Co-production of high quality hydrogen and synthesis gas via sorption-enhanced steam reforming of glycerol coupled with methane reforming of carbonates. **Chemical Engineering Journal**, *[S. l.]*, v. 360, p. 47–53, 2019. DOI: 10.1016/j.cej.2018.11.203.

DANG, Chengxiong; WU, Shijie; YANG, Guangxing; CAO, Yonghai; WANG, Hongjuan; PENG, Feng; WANG, Songrui; YU, Hao. Hydrogen Production from Sorption-Enhanced Steam Reforming of Phenol over a Ni-Ca-Al-O Bifunctional Catalyst. **ACS Sustainable Chemistry and Engineering**, *[S. l.]*, v. 8, n. 18, p. 7111–7120, 2020. b. DOI: 10.1021/acssuschemeng.0c01267.

DANG, Chengxiong; YU, Hao; WANG, Hongjuan; PENG, Feng; YANG, Yanhui. A bi-functional Co – CaO – $Ca_{12}Al_{14}O_{33}$ catalyst for sorption-enhanced steam reforming of glycerol to high-purity hydrogen. *[S. l.]*, v. 286, p. 329–338, 2016.

DEWOOLKAR, Karan D.; VAIDYA, Prakash D. Tailored hydrotalcite-based hybrid materials for hydrogen production via sorption-enhanced steam reforming of ethanol. **International Journal of Hydrogen Energy**, *[S. l.]*, v. 41, n. 14, p. 6094–6106, 2016. DOI: 10.1016/j.ijhydene.2015.10.034.

DEWOOLKAR, Karan D.; VAIDYA, Prakash D. New Hybrid Materials for Improved Hydrogen Production by the Sorption-Enhanced Steam Reforming of Butanol. **Energy Technology**, *[S. l.]*, v. 5, n. 8, p. 1300–1310, 2017. DOI: 10.1002/ente.201600645.

DI GIULIANO, A.; GALLUCCI, K.; FOSCOLO, P. U.; COURSON, C. Effect of Ni precursor salts on Ni-mayenite catalysts for steam methane reforming and on Ni-CaO-mayenite materials for sorption enhanced steam methane reforming. **International Journal of Hydrogen Energy**, *[S. l.]*, v. 44, n. 13, p. 6461–6480, 2019. DOI: 10.1016/j.ijhydene.2019.01.131.

DI MICHELE, Alessandro; DELL'ANGELO, Anna; TRIPODI, Antonio; BAHADORI, Elnaz; SÀNCHEZ, Felipe; MOTTA, Davide; DIMITRATOS, Nikolaos; ROSSETTI, Ilenia; RAMIS, Gianguido. Steam reforming of ethanol over Ni/$MgAl_2O_4$ catalysts. **International Journal of Hydrogen Energy**, *[S. l.]*, v. 44, n. 2, p. 952–964, 2019. DOI: 10.1016/j.ijhydene.2018.11.048.

DOU, Binlin; ZHANG, Hua; CUI, Guomin; WANG, Zilong; JIANG, Bo; WANG, Kaiqiang; CHEN, Haisheng; XU, Yujie. Hydrogen production by sorption-enhanced chemical looping steam reforming of ethanol in an alternating fixed-bed

reactor: Sorbent to catalyst ratio dependencies. **Energy Conversion and Management**, *[S. l.]*, v. 155, n. August 2017, p. 243–252, 2018. DOI: 10.1016/j.enconman.2017.10.075.

FERMOSO, Javier; HE, Li; CHEN, De. Production of high purity hydrogen by sorption enhanced steam reforming of crude glycerol. **International Journal of Hydrogen Energy**, *[S. l.]*, v. 37, n. 19, p. 14047–14054, 2012. DOI: 10.1016/j.ijhydene.2012.07.084.

GHUNGRUD, Swapnil A.; VAIDYA, Prakash D. Sorption-enhanced reaction process for glycerol-to-hydrogen conversion over cobalt catalyst supported on promoted hydrotalcites. **International Journal of Hydrogen Energy**, *[S. l.]*, v. 45, n. 16, p. 9440–9450, 2020. DOI: 10.1016/j.ijhydene.2020.01.206.

GORDON, Sanford; MCBRIDE, Bonnie J. Computer Program for Calculation of Complex Chemical Equilibrium. **NASA reference publication**, *[S. l.]*, v. 1311, 1994.

GUNDUZ, Seval; DOGU, Timur. Sorption-enhanced reforming of ethanol over Ni- and Co-incorporated MCM-41 type catalysts. **Industrial and Engineering Chemistry Research**, *[S. l.]*, v. 51, n. 26, p. 8796–8805, 2012. DOI: 10.1021/ie201852f.

GUO, Hongxia; FENG, Jiaqi; ZHAO, Yujun; WANG, Shengping; MA, Xinbin. Effect of micro-structure and oxygen vacancy on the stability of (Zr-Ce)-additive CaO-based sorbent in CO_2 adsorption. **Journal of CO2 Utilization**, *[S. l.]*, v. 19, p. 165–176, 2017. DOI: 10.1016/j.jcou.2017.03.015.

HAN, Seung Ju; SONG, Ji Hwan; YOO, Jaekyeong; PARK, Seungwon; KANG, Ki Hyuk; SONG, In Kyu. Sorption-enhanced hydrogen production by steam reforming of ethanol over mesoporous Co/CaO–Al_2O_3 xerogel catalysts: Effect of Ca/Al molar ratio. **International Journal of Hydrogen Energy**, *[S. l.]*, v. 42, n. 9, p. 5886–5898, 2017. DOI: 10.1016/j.ijhydene.2016.12.075.

HOSSEINI, Seyed Ehsan; ABDUL WAHID, Mazlan; JAMIL, M. M.; AZLI, Anis A. M.; MISBAH, Mohamad F. **A review on biomass-based hydrogen production for renewable energy supplyInternational Journal of Energy Research**John Wiley and Sons Ltd, , 2015. DOI: 10.1002/er.3381.

HU, Rongrong; LI, Danping; XUE, Huiyuan; ZHANG, Ni; LIU, Zhongwen; LIU, Zhaotie. Hydrogen production by sorption-enhanced steam reforming of acetic acid over Ni/$Ce_xZr_{1-x}O_2$-CaO catalysts. **International Journal of Hydrogen Energy**, *[S. l.]*, v. 42, n. 12, p. 7786–7797, 2017. DOI: 10.1016/j.ijhydene.2017.01.167.

KIM, Eun Young; KIM, Dong Suk; AHN, Byung Tae. Synthesis of Mesoporous TiO2 and its application to photocatalytic activation of methylene blue and E. coli.

Bulletin of the Korean Chemical Society, *[S. l.]*, v. 30, n. 1, p. 193–198, 2009. DOI: 10.5012/bkcs.2009.30.1.193.

KLIMESCH, Danielle S.; RAY, Abhi. DTA-TGA evaluations of the CaO-Al_2O_3-SiO_2-H_2O system treated hydrothermally. **Thermochimica Acta**, *[S. l.]*, v. 334, n. 1–2, p. 115–122, 1999. DOI: 10.1016/s0040-6031(99)00140-9.

LAMB, Jacob J.; HILLESTAD, Magne; RYTTER, Erling; BOCK, Robert; NORDGÅRD, Anna S. R.; LIEN, Kristian M.; BURHEIM, Odne S.; POLLET, Bruno G. **Traditional Routes for Hydrogen Production and Carbon Conversion**. [s.l.] : Elsevier Ltd, 2020. DOI: 10.1016/b978-0-08-102629-8.00003-7.

LI, Hongfang et al. Sorption enhanced steam reforming of methanol for high-purity hydrogen production over Cu-MgO/Al_2O_3 bifunctional catalysts. **Applied Catalysis B: Environmental**, *[S. l.]*, v. 276, n. February, p. 119052, 2020. DOI: 10.1016/j.apcatb.2020.119052.

LIU, Liang; HONG, Dikun; WANG, Nana; GUO, Xin. High purity H2 production from sorption enhanced bio-ethanol reforming via sol-gel-derived Ni–CaO–Al_2O_3 bi-functional materials. **International Journal of Hydrogen Energy**, *[S. l.]*, v. 45, n. 59, p. 34449–34460, 2020. DOI: 10.1016/j.ijhydene.2020.02.158.

LOGANATHAN, Sravanthi; TIKMANI, Mayur; MISHRA, Aakanksha; GHOSHAL, Aloke Kumar. Amine tethered pore-expanded MCM-41 for CO_2 capture: Experimental, isotherm and kinetic modeling studies. **Chemical Engineering Journal**, *[S. l.]*, v. 303, n. April 2015, p. 89–99, 2016. DOI: 10.1016/j.cej.2016.05.106.

MARTAVALTZI, Christina S.; PEFKOS, Tilemachos D.; LEMONIDOU, Angeliki A. Operational window of sorption enhanced steam reforming of methane over CaO-$Ca_{12}Al_{14}O_{33}$. *In*: INDUSTRIAL AND ENGINEERING CHEMISTRY RESEARCH 2011, **Anais** [...]. : American Chemical Society, 2011. p. 539–545. DOI: 10.1021/ie1002284.

MOJAVER, Parisa; JAFARMADAR, Samad; KHALILARYA, Shahram; CHITSAZ, Ata. Investigation and optimization of a Co-Generation plant integrated of gasifier, gas turbine and heat pipes using minimization of Gibbs free energy, Lagrange method and response surface methodology. **International Journal of Hydrogen Energy**, *[S. l.]*, v. 45, n. 38, p. 19027–19044, 2020. DOI: 10.1016/j.ijhydene.2020.04.278.

NIMMAS, Talita; JAMRUNROJ, Panupong; WONGSAKULPHASATCH, Suwimol; KIATKITTIPONG, Worapon; LAOSIRIPOJANA, Navadol; GONG, Jinlong;

ASSABUMRUNGRAT, Suttichai. Influence of CaO precursor on CO_2 capture performance and sorption-enhanced steam ethanol reforming. **International Journal of Hydrogen Energy**, *[S. l.]*, v. 44, n. 37, p. 20649–20662, 2019. DOI: https://doi.org/10.1016/j.ijhydene.2018.07.095.

OGO, Shuhei; SEKINE, Yasushi. Recent progress in ethanol steam reforming using non-noble transition metal catalysts: A review. **Fuel Processing Technology**, *[S. l.]*, v. 199, p. 106238, 2020. DOI: https://doi.org/10.1016/j.fuproc.2019.106238.

PHROMPRASIT, Janewit; POWELL, Jon; WONGSAKULPHASATCH, Suwimol; KIATKITTIPONG, Worapon; BUMROONGSAKULSAWAT, Palang; ASSABUMRUNGRAT, Suttichai. H_2 production from sorption enhanced steam reforming of biogas using multifunctional catalysts of Ni over Zr-, Ce- and La-modified CaO sorbents. **Chemical Engineering Journal**, *[S. l.]*, v. 313, p. 1415–1425, 2017. DOI: https://doi.org/10.1016/j.cej.2016.11.051.

PHUNG, Thanh Khoa; PHAM, Thong Le Minh; NGUYEN, Anh Nga T.; VU, Khanh B.; GIANG, Ha Ngoc; NGUYEN, Tuan Anh; HUYNH, Thanh Cong; PHAM, Hong Duc. Effect of Supports and Promoters on the Performance of Ni-Based Catalysts in Ethanol Steam Reforming. **Chemical Engineering and Technology**, *[S. l.]*, v. 43, n. 4, p. 672–688, 2020. DOI: 10.1002/ceat.201900445.

QI, Zhang; DAYING, Han; YANG, Liu; QIAN, Ye; ZIBIN, Zhu. Analysis of CO_2 sorption/desorption kinetic behaviors and reaction mechanisms on Li_4SiO_4. **AIChE Journal**, *[S. l.]*, v. 59, n. 3, p. 901–911, 2013. DOI: 10.1002/aic.13861.

RAHMANZADEH, Lida; TAGHIZADEH, M. Sorption-enhanced ethanol steam reforming on Ce-Ni/MCM-41 with simultaneous CO_2 adsorption over Na- and Zr-promoted CaO based sorbent. **International Journal of Hydrogen Energy**, *[S. l.]*, v. 44, n. 39, p. 21238–21250, 2019. DOI: 10.1016/j.ijhydene.2019.04.289.

REDDY, Sivamohan N.; NANDA, Sonil; DALAI, Ajay K.; KOZINSKI, Janusz A. **Supercritical water gasification of biomass for hydrogen productionInternational Journal of Hydrogen Energy**Elsevier Ltd, , 2014. DOI: 10.1016/j.ijhydene.2014.02.125.

SANG, Sier; ZHAO, Zhi Jian; TIAN, Hao; SUN, Zhao; LI, Hongfang; ASSABUMRUNGRAT, Suttichai; MUHAMMAD, Tahir; ZENG, Liang; GONG, Jinlong. Promotional role of MgO on sorption-enhanced steam reforming of ethanol over Ni/CaO catalysts. **AIChE Journal**, *[S. l.]*, 2019. DOI: 10.1002/aic.16877.

SHARMA, Yogesh Chandra; KUMAR, Ashutosh; PRASAD, Ram;

UPADHYAY, Siddh Nath. Ethanol steam reforming for hydrogen production: Latest and effective catalyst modification strategies to minimize carbonaceous deactivation. **Renewable and Sustainable Energy Reviews**, *[S. l.]*, v. 74, n. April 2016, p. 89–103, 2017. DOI: 10.1016/j.rser.2017.02.049.

SIKARWAR, Vineet Singh; ZHAO, Ming. Biomass Gasification. *In*: **Encyclopedia of Sustainable Technologies**. [s.l.] : Elsevier, 2017. p. 205–216. DOI: 10.1016/B978-0-12-409548-9.10533-0.

SNYDER, C. A. **NASA Chemical Equilibrium with Applications (CEA)**, 2016. Available in: < https://software.nasa.gov/software/LEW-17687-1>.

THOMAS, John Meurig; THOMAS, W. John. **Principles and practice of heterogeneous catalysis**. [s.l.] : John Wiley & Sons, 2014.

TIAN, Sicong; YANG, Xiaoxia; CHEN, Xuejing; LI, Guangshi; AIKELAIMU, Aihemaiti; MENG, Yuan; GAO, Yuchen; LANG, Candace; FAN, Maohong. Catalytic calcium-looping reforming of biogas: A novel strategy to produce syngas with improved H_2/CO molar ratios. **Journal of Cleaner Production**, *[S. l.]*, v. 270, 2020. DOI: 10.1016/j.jclepro.2020.122504.

VANGA, Giuseppina; GATTIA, Daniele Mirabile; STENDARDO, Stefano; SCACCIA, Silvera. Novel synthesis of combined CaO-$Ca_{12}Al_{14}O_{33}$ -Ni sorbent-catalyst material for sorption enhanced steam reforming processes. **Ceramics International**, *[S. l.]*, v. 45, n. 6, p. 7594–7605, 2019. DOI: 10.1016/j.ceramint.2019.01.054.

WANG, Chao; DOU, Binlin; JIANG, Bo; SONG, Yongchen; DU, Baoguo; ZHANG, Chuan; WANG, Kaiqiang; CHEN, Haisheng; XU, Yujie. Sorption-enhanced steam reforming of glycerol on Ni-based multifunctional catalysts. **International Journal of Hydrogen Energy**, *[S. l.]*, v. 40, n. 22, p. 7037–7044, 2015. DOI: 10.1016/j.ijhydene.2015.04.023.

WANG, Denghui; XIAO, Rui; ZHANG, Huiyan; HE, Guangying. Comparison of catalytic pyrolysis of biomass with MCM-41 and CaO catalysts by using TGA-FTIR analysis. **Journal of Analytical and Applied Pyrolysis**, *[S. l.]*, v. 89, n. 2, p. 171–177, 2010. DOI: 10.1016/j.jaap.2010.07.008.

WANG, Mingyong; WANG, Zhi; GONG, Xuzhong; GUO, Zhancheng. **The intensification technologies to water electrolysis for hydrogen production - A reviewRenewable and Sustainable Energy Reviews,** Elsevier Ltd, 2014. DOI: 10.1016/j.rser.2013.08.090.

WANG, Nana; FENG, Yuchuan; GUO, Xin; NI, Shiyi. Continuous high-purity

hydrogen production by sorption enhanced steam reforming of ethanol over modified lithium silicate. **International Journal of Hydrogen Energy**, *[S. l.]*, v. 46, n. 16, p. 10119–10130, 2021. a. DOI: 10.1016/j.ijhydene.2020.04.225.

WANG, Wenju; WANG, Y. Q. Thermodynamic analysis of steam reforming of ethanol for hydrogen generation. **International Journal of Energy Research**, *[S. l.]*, v. 32, n. 15, p. 1432–1443, 2008.

WANG, Xun; HE, Yiping; XU, Tingting; XIAO, Bo; LIU, Shiming; HU, Zhiquan; LI, Jianfen. CO_2 sorption-enhanced steam reforming of phenol using Ni–M/CaO–$Ca_{12}Al_{14}O_{33}$ (M = Cu, Co, and Ce) as catalytic sorbents. **Chemical Engineering Journal**, *[S. l.]*, v. 393, n. March, p. 124769, 2020. DOI: 10.1016/j.cej.2020.124769.

WANG, Yinxiang; MEMON, Muhammad Zaki; SEELRO, Majid Ali; FU, Weng; GAO, Yuan; DONG, Yingchao; JI, Guozhao. A review of CO_2 sorbents for promoting hydrogen production in the sorption-enhanced steam reforming process. **International Journal of Hydrogen Energy**, *[S. l.]*, 2021. b. DOI: 10.1016/j.ijhydene.2021.01.206.

WU, Gaowei; ZHANG, Chengxi; LI, Shuirong; HUANG, Zhiqi; YAN, Suli; WANG, Shengping; MA, Xinbin; GONG, Jinlong. Sorption enhanced steam reforming of ethanol on Ni-CaO-Al_2O_3 multifunctional catalysts derived from hydrotalcite-like compounds. **Energy and Environmental Science**, *[S. l.]*, v. 5, n. 10, p. 8942–8949, 2012. DOI: 10.1039/c2ee21995f.

XU, Pan; ZHOU, Zhiming M.; ZHAO, Changjun; CHENG, Zhenmin. Ni/CaO-Al_2O_3 bifunctional catalysts for sorption-enhanced steam methane reforming. **AIChE Journal**, *[S. l.]*, v. 60, n. 10, p. 3547–3556, 2014. DOI: 10.1002/aic.14543.

XU, Yongqing; LU, Bowen; LUO, Cong; CHEN, Jian; ZHANG, Zewu; ZHANG, Liqi. Sorption enhanced steam reforming of ethanol over Ni-based catalyst coupling with high-performance CaO pellets. **Chemical Engineering Journal**, *[S. l.]*, v. 406, n. August 2020, p. 126903, 2021. DOI: 10.1016/j.cej.2020.126903.

XU, Yongqing; LUO, Cong; ZHENG, Ying; DING, Haoran; WANG, Qiyao; SHEN, Qiuwan; LI, Xiaoshan; ZHANG, Liqi. Characteristics and performance of CaO-based high temperature CO_2 sorbents derived from a sol-gel process with different supports. **RSC Advances**, *[S. l.]*, v. 6, n. 83, p. 79285–79296, 2016. DOI: 10.1039/c6ra15785h.

YOON, Hyung Jin; MUN, Sungyong; LEE, Ki Bong. Facile reactivation of used CaO-based CO_2 sorbent via physical treatment: Critical relationship between particle size and CO_2 sorption performance. **Chemical Engineering Journal**, *[S. l.]*, v. 408, n.

September 2020, p. 127234, 2021. DOI: 10.1016/j.cej.2020.127234.

ZANCHET, Daniela; SANTOS, Joao Batista O.; DAMYANOVA, Sonia; GALLO, Jean Marcel R.; BUENO, José Maria C. Toward understanding metal-catalyzed ethanol reforming. **ACS Catalysis**, *[S. l.]*, v. 5, n. 6, p. 3841–3863, 2015. DOI: 10.1021/cs5020755.

ZHAO, Changjun; ZHOU, Zhiming; CHENG, Zhenmin; FANG, Xiangchen. Sol-gel-derived, $CaZrO_3$-stabilized Ni/CaO-$CaZrO_3$ bifunctional catalyst for sorption-enhanced steam methane reforming. **Applied Catalysis B: Environmental**, *[S. l.]*, v. 196, p. 16–26, 2016. DOI: 10.1016/j.apcatb.2016.05.021.

ZHAO, Ming; SHI, Jeffrey; ZHONG, Xia; TIAN, Sicong; BLAMEY, John; JIANG, Jianguo; FENNELL, Paul S. A novel calcium looping absorbent incorporated with polymorphic spacers for hydrogen production and CO_2 capture. **Energy and Environmental Science**, *[S. l.]*, v. 7, n. 10, p. 3291–3295, 2014. DOI: 10.1039/c4ee01281j.

ZHAO, Xiao-yong; XUE, Ya-ping; YAN, Chang-feng; WANG, Zhi-da; GUO, Chang-qing; HUANG, Shi-lin. Sorbent assisted catalyst of Ni-CaO-La_2O_3 for sorption enhanced steam reforming of bio-oil with acetic acid as the model compound. **Chemical Engineering and Processing: Process Intensification**, *[S. l.]*, v. 119, p. 106–112, 2017. DOI: https://doi.org/10.1016/j.cep.2017.05.012.

ZHOU, Zhiming; QI, Yang; XIE, Miaomiao; CHENG, Zhenmin; YUAN, Weikang. Synthesis of CaO-based sorbents through incorporation of alumina/aluminate and their CO_2 capture performance. **Chemical Engineering Science**, *[S. l.]*, v. 74, p. 172–180, 2012. DOI: 10.1016/j.ces.2012.02.042.

APPENDIX – SUPLEMENTARY INFORMATION

A. Nitrogen Physisorption

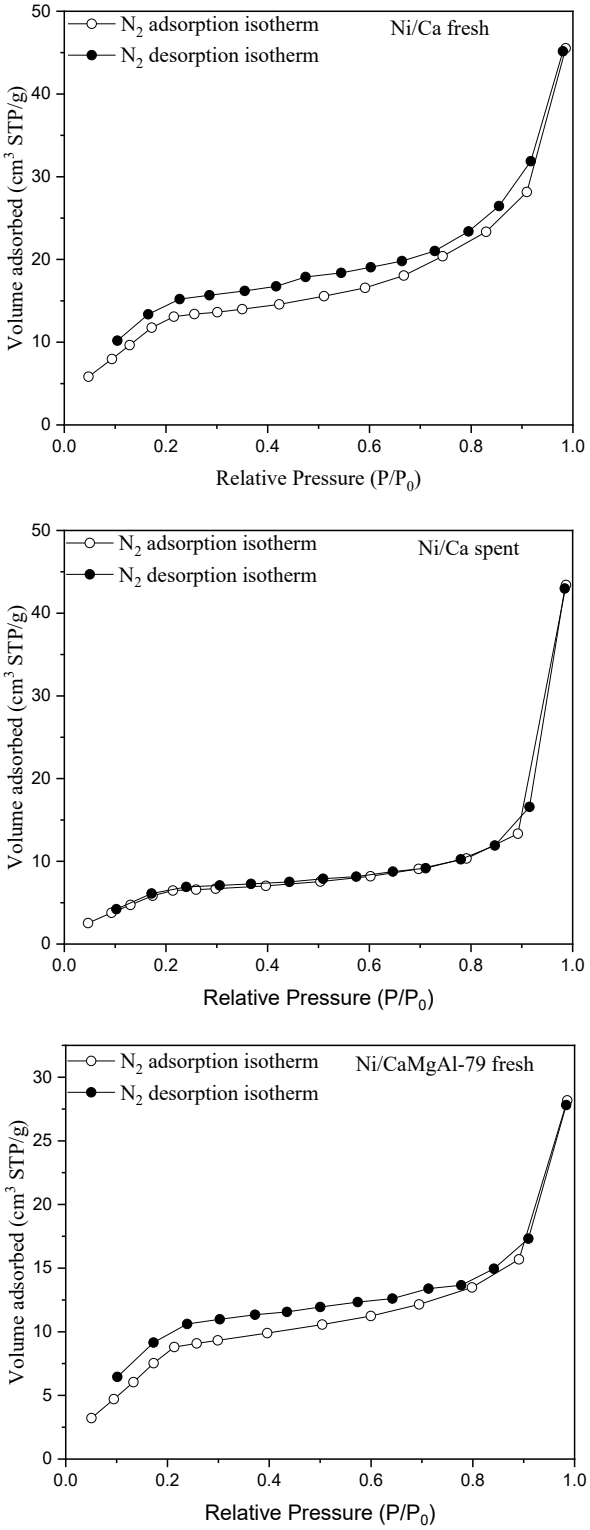

Figure A.1. Nitrogen adsorption (unfilled points) and desorption (filled points) isotherms at 77 K for the studied catalysts.

B. Mapping of the chemical elements

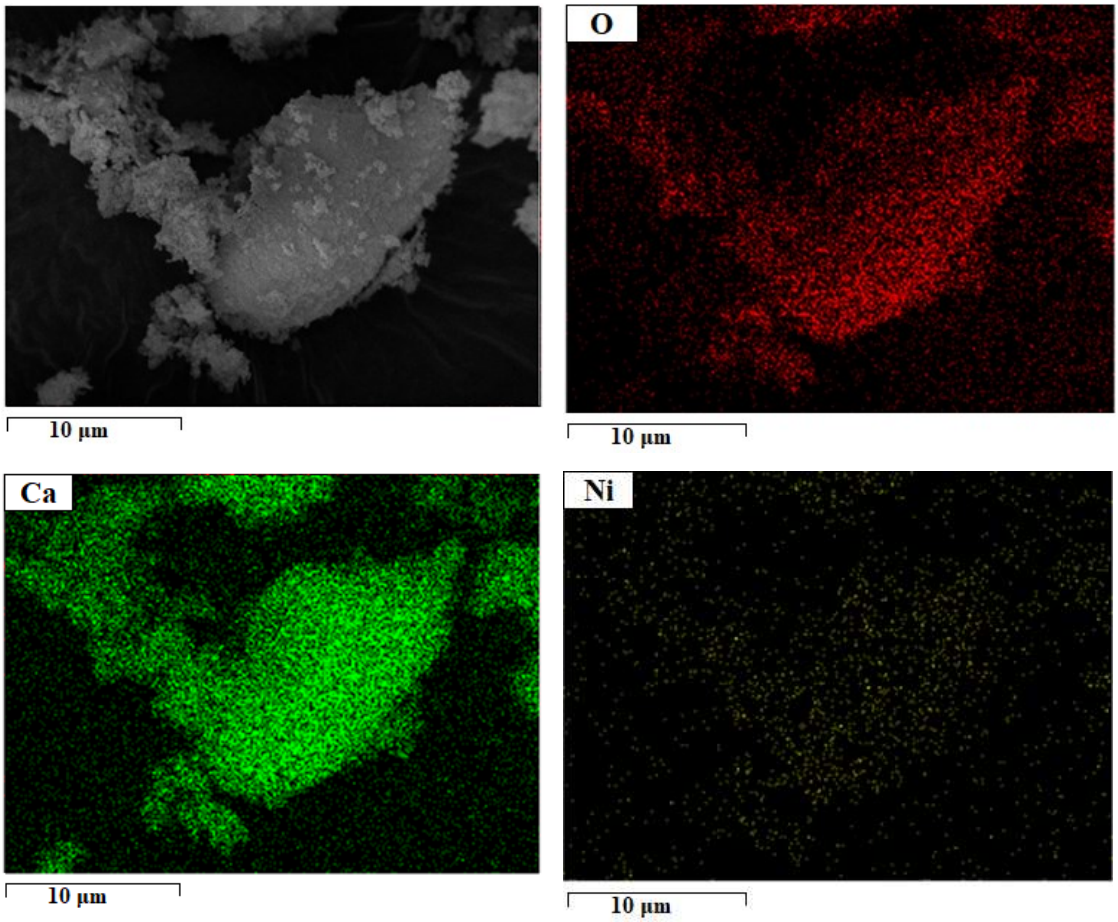

Figure B.1. EDS mapping for the fresh Ni/Ca catalyst.

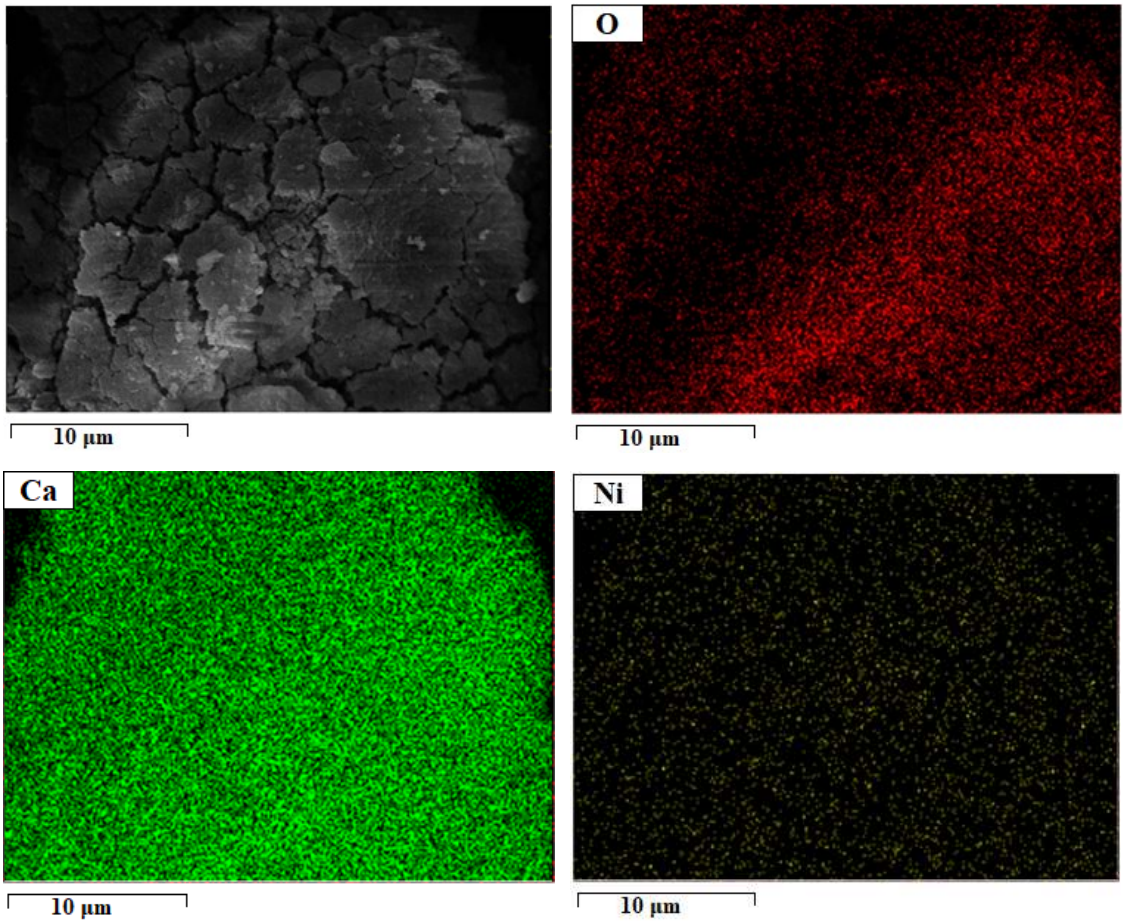

Figure B.2. EDS mapping for the spent Ni/Ca catalyst.

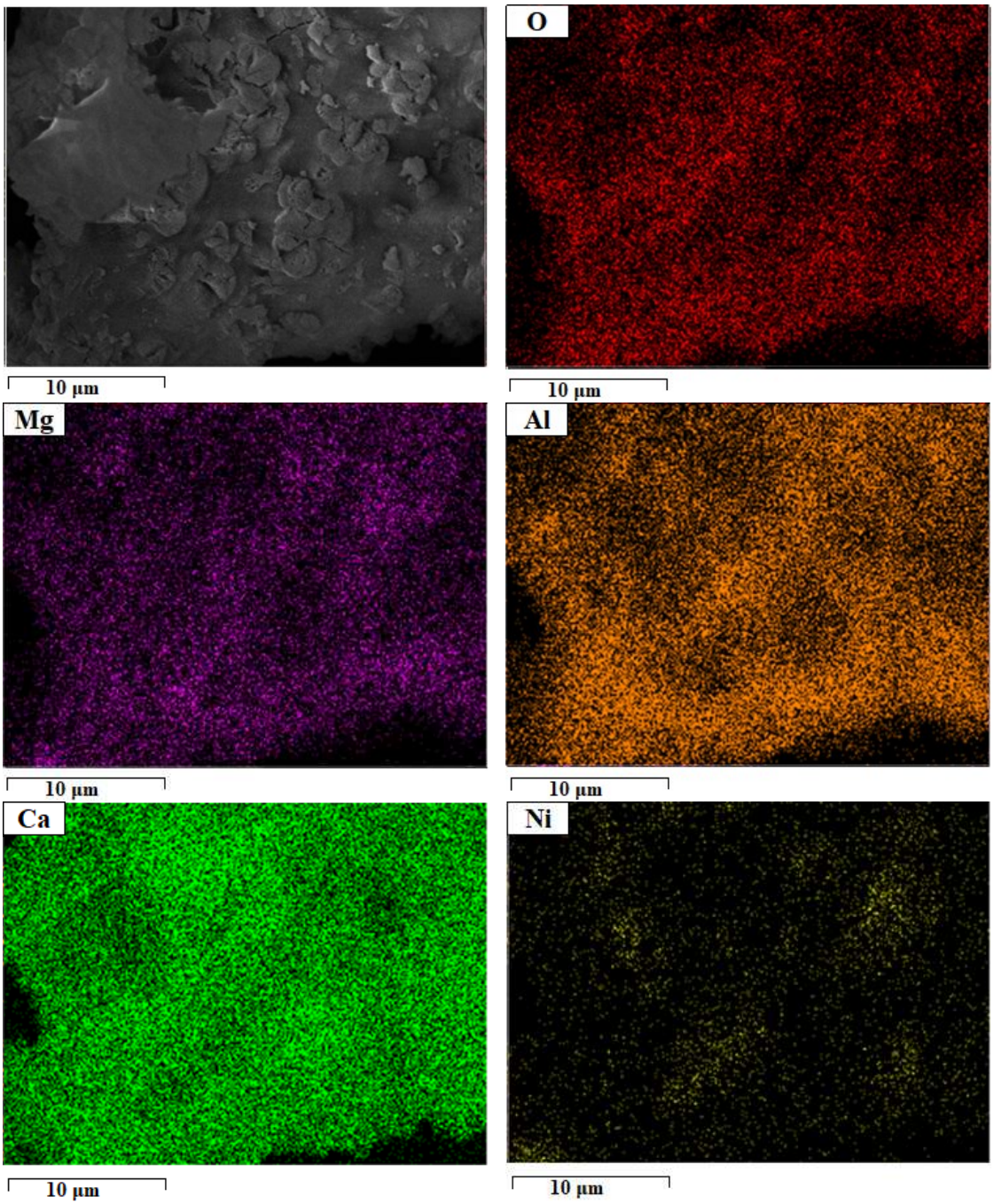

Figure B.3. EDS mapping for the fresh Ni/CaMgAl-68 catalyst.

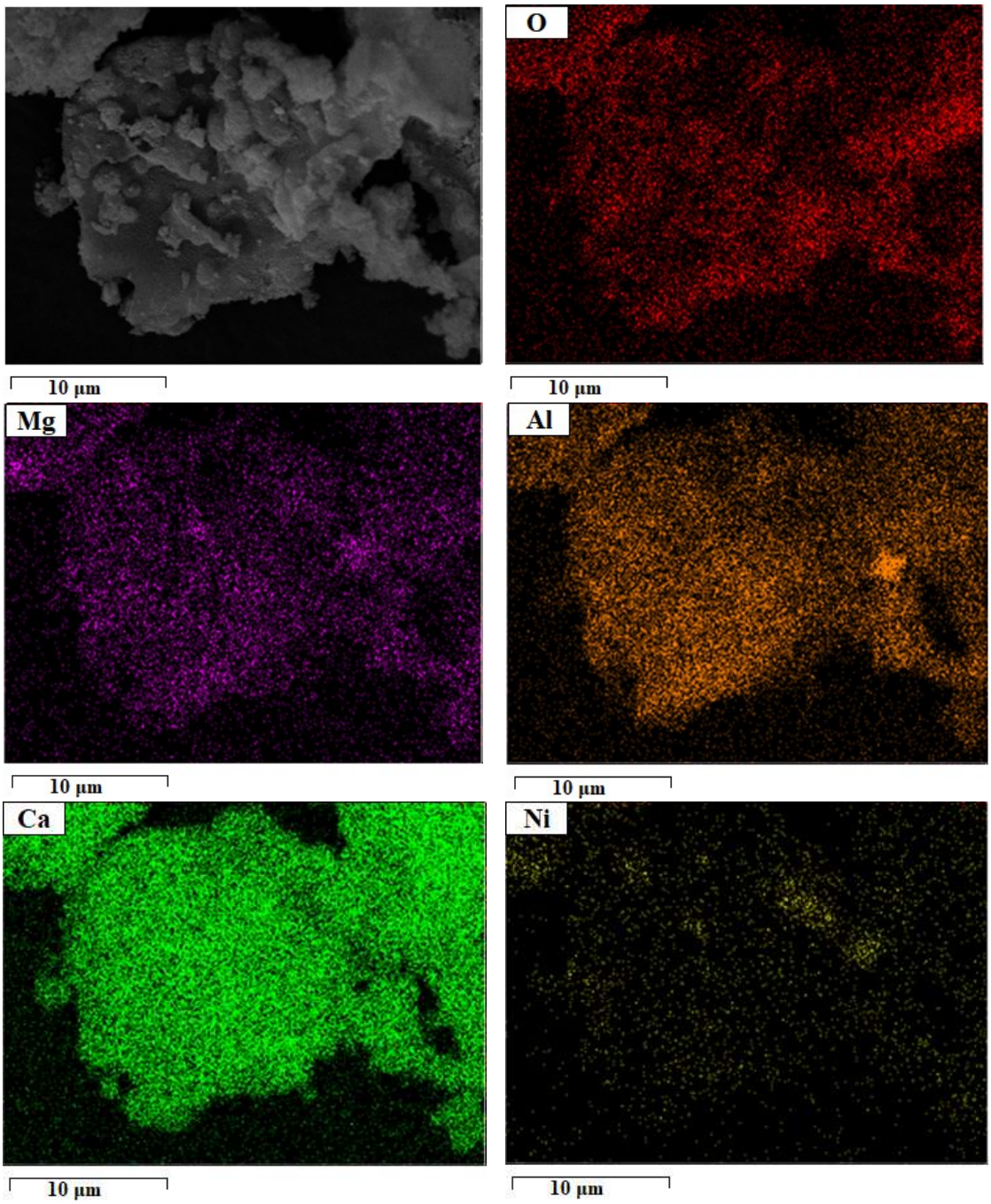

Figure B.4. EDS mapping for the spent Ni/CaMgAl-68 catalyst.